ROYAUME DU MAROC
Université Mohammed V - RABAT -
جامعة محمد الخامس – الرباط –
Faculté des sciences
كلية العلوم
CENTRE D'ETUDES DOCTORALES - SCIENCES ET TECHNOLOGIES

N° d'ordre : 3094

# THESE

*En vue de l'obtention du :* ***DOCTORAT***

*Structure de Recherche : Laboratoire de Matière condensée et Sciences Interdisciplinaires (LaMcSI)*

*Discipline : Physique Informatique*

*Spécialité : Matière condensée et modélisation des Systèmes*

***Présentée et soutenue le :28/04/2018 par :***

***Younes ZIAT***

## *Ab initio studies of the magnetic and electronic properties of $SnO_2$, $ZrO_2$ and $FeS_2$ for spintronic applications*

### *JURY*

| | | |
|---|---|---|
| *Youssef EL AMRAOUI,* | *PES, Faculté des Sciences, Rabat* | *Président* |
| *Abdelilah BENYOUSSEF,* | *PES, Membre résident de l'Académie Hassan II des Sciences et Techniques* | *Co-Directeur de Thèse* |
| *Abdallah EL KENZ,* | *PES, Faculté des Sciences, Rabat* | *Directeur de Thèse* |
| *Ahmed HOURMATALLAH,* | *PES, Ecole Normale Supérieure, Fès* | *Rapporteur* |
| *Hamid EZ-ZAHRAOUY,* | *PES, Faculté des Sciences, Rabat* | *Examinateur* |
| *Mohammed LOULIDI,* | *PES, Faculté des Sciences, Rabat* | *Rapporteur* |

Année Universitaire : 2017/2018

**Dedication**

*To*

*My parents*
*To my sisters, brothers and my family to all my professors and teachers*
*to all my friends*

**Acknowledgements**

This thesis has been carried out at Laboratory of Condensed Matter and Interdisciplinary Sciences (LaMCScI), Faculty of Science, Mohammed V University – Rabat, under the supervision of Prof. Hamid EZ-ZAHRAOUY.

First and foremost, praises and thanks go to Allah, the Almighty, for his unlimited and uncountable blessings in my whole life and throughout my research work especially.

I would like to take this opportunity to express my thanks and gratitude to the many people who have in so many ways helped and supported me throughout my thesis study.

I would like to express my deepest sense of **G**ratitude **(with a capital and bold g)** to my supervisor Prof. Abdallah EL KENZ, who offered his continuous advices and encouragement throughout the course of this thesis. He supervised my work two times, during my bachelor degree and now in my thesis. I thank him for the systematic guidance and great efforts he put into training me in the scientific field.

I am especially thankful to my co-supervisor Prof. Abdelilah BENYOUSSEF for his fruitful discuss, help, encouraging and most of all patience throughout the entire process.
I wish to thank my committee members who were more than generous with their expertise and precious time.

I would like to thank the president of this thesis Prof. Youssef EL AMRAOUI from Faculty of Science Rabat for reviewing this thesis.

Also i would like to extend my thanks to Prof. Ahmed HOURMATALLAH from *Ecole Normale Supérieure, Fès*, for reporting and reviewing this thesis.

I would like to thank Prof. Hamid EZ-ZAHRAOUY from Faculty of Science Rabat, for reviewing this thesis.

I would like to extend my gratitude to Prof. Mohammed LOULIDI from Faculty of Science Rabat, for reporting and reviewing this thesis.

I am thankful to all my colleagues, friends and family members for the help, support and encouragement whenever i was in need.

## Abstract

Within LDA, the ferrimagnetic state is predicted in $Sn_{0.98-x}Mn_{0.02}Cr_xO_2$ (x=0.09). Within GGA, the stability of the ferrimagnetic also is observed (x=0.05). $Sn_{0.98}Mn_{0.02}O_{1.95}F_{0.05}$ system could induce the FM stability instead the DLM and shows the half-metallic characteristic. within GGA, $Zr_{14}OsCoO_{32}$ system provides the half-metallic behavior. With mBJ, the presence of magnetic gap is predicted. For $Zr_{14}MnCoO_{32;}$ the system provides the half metallic behavior. For $FeS_2$ pyrite, the antiferromagnetic (AFM) stability belong to super-exchange coupling is observed in $Fe_{0.98}V_{0.02}S_2$. However, $Fe_{0.95}Cr_{0.05}S_2$ shows FM stability belongs to double-exchange coupling type and having a considered $T_C$ which leads to significant magnetic proprieties. Moreover, 3d-3d hybridization of transition metals show that is believed to result a half-metal propriety. The stabilization of the FM state in N-doped $Fe_{0.98}V_{0.02}S_2$ is observed.



**Key words:** ab intio; Diluted magnetic semiconductors; spintronic; ferromagnetic; ferrimagnetic; DLM; half metallic.

## Résumé

Avec LDA, l'état ferrimagnétique est prédit dans $Sn_{0.98-x}Mn_{0.02}Cr_xO_2$ (x = 0.09). Avec GGA, on observe également la stabilité du ferrimagnétique (x = 0,05). Le système $Sn_{0.98}Mn_{0.02}O_{1.95}F_{0.05}$ pourrait induire la stabilité FM au lieu du DLM et montre la caractéristique semi-métallique. Avec GGA, le système $Zr_{14}OsCoO_{32}$ fournit le comportement semi-métallique. Avec mBJ, la présence du gap magnétique est prédite. Pour $Zr_{14}MnCoO_{32}$; le système fournit le comportement semi-métallique. Pour la pyrite $FeS_2$, la stabilité antiferromagnétique appartenant au couplage de super-échange est observée dans $Fe_{0.98}V_{0.02}S_2$. Cependant, $Fe_{0.95}Cr_{0,05}S_2$ montre que la stabilité de la FM appartient au type de couplage à double échange et qu'elle a un $T_C$ considéré qui conduit à des propriétés magnétiques significatives. De plus, l'hybridation 3d-3d des métaux de transition montre que l'on croit qu'elle résulte d'une propriété semi-métallique. La stabilisation de l'état FM dans $Fe_{0.98}V_{0.02}S_2$ dopé N est observée.



**Mots-clés:** ab initio; Semiconducteurs magnétiques dilués; spintronique; ferromagnétique; ferrimagnétique; DLM; semi-métallique.

# Résumé détaillé

Le but principal de la présente thèse est d'étudier théoriquement les propriétés magnétiques et électroniques de certains semi-conducteurs magnétiques dilués (DMS), ainsi que de prédire leur utilisation potentielle dans les applications de spinotronique. Nous avons restreint l'étude de certains oxydes magnétiques dilués ($SnO_2$ et $ZrO_2$) et de la pyrite $FeS_2$, car ces types de matériaux sont utiles dans d'autres domaines de la science des matériaux.

Pour le rutile $SnO_2$, nous avons incorporé quelques métaux de transition (Manganèse: Mn et Chrome: Cr), en utilisant l'approximation du potentiel cohérent du Korringa, Kohn et Rostoker (KKR-CPA) en relation avec l'approximation de densité locale et l'approximation du gradient généralisé), pour prédire l'effet de Mn et Cr sur la stabilité des systèmes considérés.

Nos résultats indiquent que l'état ferromagnétique (FM) est plus stable que le moment local désordonné (DLM) pour le système dopé ($Sn_{1-x}Cr_xO_2$; x = 0.07, 0.09, 0.12 et 0.15), alors que l'état DLM est plus stable que le FM pour le système dopé ($Sn_{1-x}Mn_xO_2$; x = 0.02 et 0.05). Cependant, les états FM et/ou ferrimagnétiques sont stables pour le système dopé ($Sn_{0,98-x}Mn_{0,02}Cr_xO_2$; x = 0.05, 0.09 et 0.13), ici la concentration Cr détermine l'état le plus stable. De plus, nous avons estimé la température de Curie ($T_C$) pour le $SnO_2$ dopé au Cr.

Pour le $SnO_2$ dopé au Mn, l'état DLM est stable, car le spin minoritaire de la bande Mn[d] est inoccupé et l'impureté Mn a une configuration électronique $d^3$ en raison de la substitution de $Sn^{4+}$ par $Mn^{4+}$. Alors, $e_g^+$ de Mn[d] est inoccupé.

Puisque l'état FM relié au demi-métal a été largement recherché en raison de ses applications potentielles dans le domaine spintronique, nous avons évalué l'effet du système dopé au fluor $Sn_{0.98}Mn_{0.02}O_2$. Donc le système $Sn_{0.98}Mn_{0.02}O_{1.95}F_{0.05}$ pourrait induire la stabilité FM au lieu de la DLM et montrer la caractéristique semi-métallique Puisque l'état $e_g^+$ est situé autour du niveau de Fermi.

Pour le $SnO_2$ dopé au Cr, nous avons observé que le spin majoritaire $t_{2g}^+$du Cr se situe au niveau de Fermi, ce qui explique l'existence de l'état semi-métalliques. Pour $Sn_{0.98-}$

$_x Mn_{0.02}Cr_xO_2$ et avec LDA, l'état ferrimagnétique est prédit lorsque x = 0.09. Avec GGA, la stabilité du ferrimagnétique est également observée lorsque x = 0.05.

Avant d'expliquer le comportement ferrimagnétique, nous avons remarqué que $Sn_{0.98}Mn_{0.02}O_2$ est en relation avec la stabilité antiferromagnétique (DLM) et que les moments magnétiques d'au moins deux sous-réseaux sont antiparallèles. Contrairement à l'antiferromagnétisme, en ferrimagnétique, l'aimantation des différents sous-réseaux n'annule pas complètement les uns les autres; donc, le ferrimagnétisme a une aimantation spontanée; par conséquent, 2% de Mn avec le Cr expliquerait que la transformation magnétique, comme de ferrimagnétique au FM ou l'inverse, se produit lorsque le champ magnétique externe (H) est varié. De tels types de transitions sont induits par le champ magnétique.

Pour étudier la zircone $ZrO_2$, nous avons utilisé la méthode des ondes planes augmentées linéarisées (FP-LAPW) implémentée dans le code Wien2K, incluant les approches GGA et le potentiel modifié de Becke-Jonhson (mBJ). Pour la bande de gap relative au $ZrO_2$ pur, La densité d'états calculée (DOS) est plus proche de l'expérimental avec le mBJ.

Pour $Zr_{14}OsCoO_{32}$, nous avons deux cas: d'une part, avec GGA, le système $Zr_{14}OsCoO_{32}$ fournit le couplage entre Os[5d] et Co[3d], et le comportement semi-métallique est estimé bien qu'il ne soit pas polarisé à 100% de la partie négatif de niveau de Fermi. Avec mBJ, la présence du gap magnétique est prédite, les charges sont ($Os^{3+}$ et $Co^{2+}$, où les configurations Os : $5d^5$ et Co : $3d^7$). Pour Os, on peut estimer que les spins majoritaires de $e^+_g$ et $t^+_{2g}$ sont complètement remplies car une partie de $t^+_{2g}$ est apparue autour de (1.40 à 2.40) eV quand les spins des minorités sont vides. En outre, avec $d^7$ de Co, nous pouvons remarquer que le $t^+_{2g}$ du spin majoritaire est apparu autour de (-2.90 à 0.20) eV, alors les deux spins up/down de $e^+_g$ doivent être complètement remplis pour avoir 3 spins en $t^+_{2g}$ pour cet arrangement d'énergie alors que le spin minoritaire de $t_{2g}$ de Co sont vide.

dans $Zr_{14}MnCoO_{32}$, le système fournit l'hybridation entre Mn[3d] et Co[3d], et le comportement semi-métallique est estimé, de plus , pour Co[3d] nous n'avons pas la polarité à 100% au niveau de Fermi, et pour les charges, on a ($Mn^{2+}$ et $Co^{2+}$). Ici, Mn et Co ont ($3d^5$ et $3d^7$), respectivement, cette information indique que Mn possède 2 spins dans l'état $e^+_g$ et 3 dans l'état $t^+_{2g}$. Où $3d^7$ de Co ayant 4 spins en $e^+_g$ et 3 spins pour $t^+_{2g}$ .

Pour la pyrite $FeS_2$, nous avons utilisé le KKR-CPA, pour étudier le $FeS_2$ dopé au vanadium et au chrome et co-dopé. Nous avons observé la stabilité antiferromagnétique (AFM)

appartenir au type de couplage de super-échange, ce qui explique l'existant de la DLM en $Fe_{0.98}V_{0.02}S_2$, cependant, $Fe_{0.95}Cr_{0.05}S_2$ montre que la stabilité de FM appartient au type de couplage à double échange et ayant un $T_C$ qui conduit à des propriétés magnétiques importantes. De plus, l'hybridation 3d-3d des métaux de transition montre que l'on pense qu'il en résulte des propriétés semi-métalliques pour le système $Fe_{0.93}V_{0.02}Cr_{0.05}S_2$, donc, (V et Cr) pourrait être en interaction avec l'orbitale 3p de S, en conséquence forme l'hybridation orbitale pd et produit un champ de moment magnétique efficace pour aligner le moment magnétique V et Cr et stabiliser le FM semi-métallique.

Après cela, nous avons incorporé l'azote dans les systèmes suivants: $Fe_{0.98}V_{0.02}S_2$ et $Fe_{0.98}Cr_{0.02}S_2$. La stabilisation de l'état FM dans $Fe_{0.98}V_{0.02}S_2$ N-dopé est observée. Le spin-majoritaire lié à est situé autour du niveau de Fermi.

Pour $Fe_{0.98}Cr_{0.02}S_{1.97}N_{0.03}$, l'azote induit une hybridation entre Cr[3d] et N[2p]. Nous avons prédit un agrandissement du pic du Cr [3d]. En outre, le moment total des systèmes étudiés est augmenté ainsi que $T_C$.

# *Summary*

# Part 1: Diluted magnetic semiconductors (DMSs) in spintronic applications

## 1 - 1 - Introduction and motivation

Diluted magnetic semiconductors (DMSs) materials are very attractive for integration of electronic (field effect transistors), optical applications, magnetic (memory) devices, etc [1-3].

In addition, DMSs are expected to play an important role in interdisciplinary materials science and future spintronics to explore novel physics and new devices with low costs and high efficiencies.

On the other hand, oxide semiconductors have wide band gap, transparent for visible light and can be doped heavily with n-type carrier. This Characteristic serves an important role as transparent conductor that is used for various applications [4]. Beside that, the advantages of of oxide semiconductors are the capability to be grown at low temperature even on plastic substrate, ecological safety, durability with low cost, etc [5]. Moreover, the large electronegativity of oxygen is expected to produce strong p-d exchange coupling between band carriers and localized spins [6]. Here is worthy to indicate that the DMS which including ferromagnetic stability connected to the half metal has been extensively searched due to its potential applications in spintronic field. Then, our topics was emphasizing on some useful materials presented in the following oxides $SnO_2$, $ZrO_2$ and $FeS_2$ pyrite. For these reasons, the ab-inition integreted some methods (KKR-CPA and FP-LAPW) implemented in the (MACHIKANEYAMA 2002V09 and Wien2k codes) were used to predict the effect of the impurities on those materials in terms of ferromagnetic stability. Subsequently, within our investigation, we have intended to contribute theoretically in that field of spintronic. And making our results as a steps toward the experimental side for others researches and real applications.

## 1 - 2 - Spintronics and giant magneto-resistance

In the last decades, a new science was born with the idea of using the spin present in the charge carriers in semiconductors. It is spin electronics or (spintronic). Its principle consists on the manipulation of the spin orientation in the magnetic elements. In the presence of a magnetic field, the spins of the (ferromagnetic state, antiferromagnetic state…) are oriented, which made it possible to use additional properties in order to interact the electrical field, the

magnetic field, the electrical current and the polarization which gave another degree of freedom and carry out to many applications for efficient devices.

The principle of spintronics is putting in the path of the electrons a thin layer of magnetized material as an example (iron) to stop or slow the electrons of a certain spin direction (up or down), see figure 1.1. We considered in the middle of a conductive material (copper) a layer of iron as a ferromagnetic material with a spin up orientation, we passed a current of electrons with two spin directions, the principle is that the electrons with a spin parallel to the orientation of iron spins could pass. Other down spin electrons were stopped by the iron layer. This is the fact which enabled the realization of giant magneto-resistance.

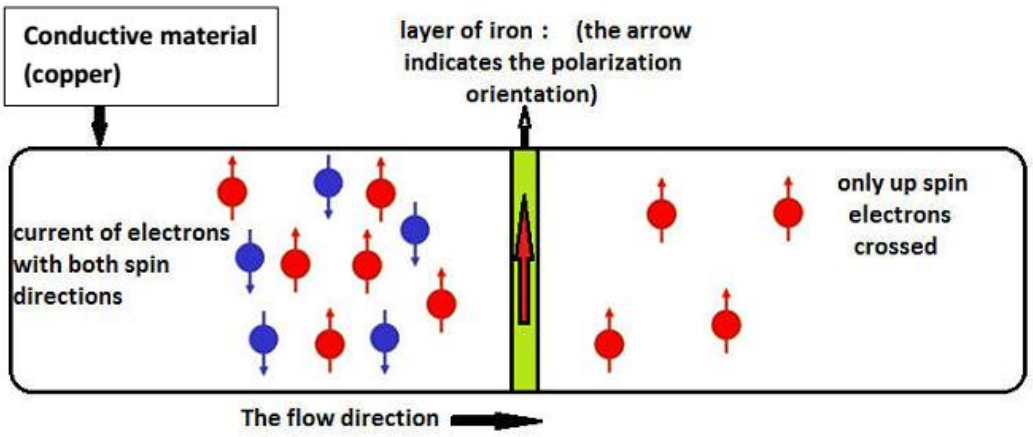


***Figure 1.1:*** *principle of the spintronics operating principle*

The Giant Magneto-resistance Effect (GMR) is a quantum effect observed in thin film structures composed of alternating ferromagnetic and non-magnetic conductive layers. This effect is used in the most important industrially spintronics application. This is what makes possible the current hard drive heads to be as efficient as they are today.

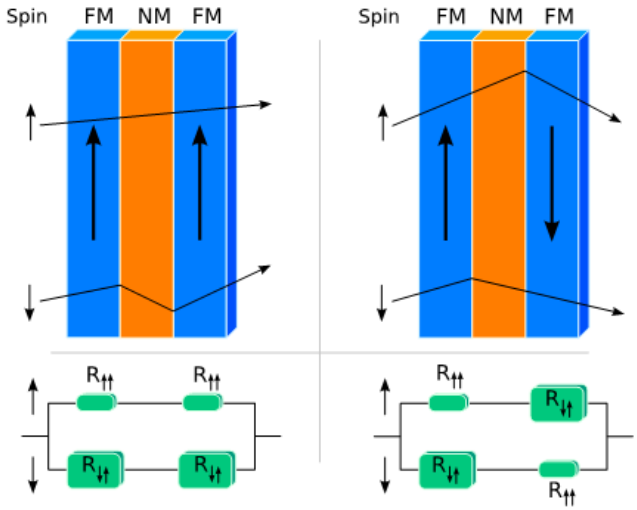


***Figure 1.2:*** *The operating principle of the GMR [7]. Depending on whether the two magnetic layers are polarized in the same direction (left) or in opposite direction (right). The total resistance of the stack of layers is different. This phenomenon is exploited to achieve spin valves used in modern hard drives.*

In 1988, Albert Fert and his colleagues were able to demonstrate the (GMR). Its use has increased the storage capacities of computers hard disks. In 2007, Albert Fert and Peter Grünberg were thus awarded the Nobel Prize in Physics for their discovery.

In figure 1.2, we have two channels (up and down channel). These two channels are equivalent in conventional conductive material. For a ferromagnetic material, that may be the opposite. Depending on the density of states at the Fermi level, there may be a big difference between the two. In the case of the two channels have opposite polarizations, conduction may only be ensured by one of the two channels. Where the other being insulator. This is the so called half metallic.

In addition, Albert Fert and Peter Grünberg saw very large resistance changes in materials comprised of alternating very thin layers of various metallic elements, figure 1.3[8-10].

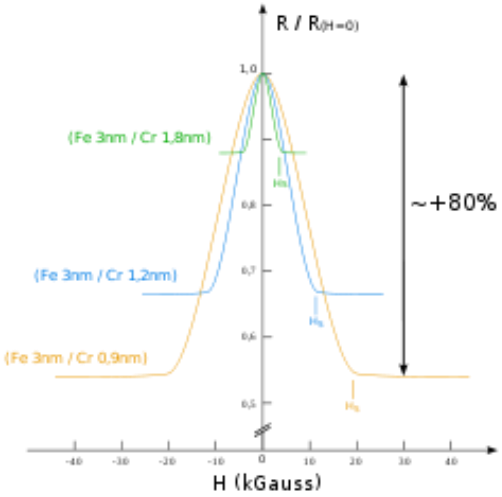


***Figure 1.3:*** *The founding results of Albert Fert and Peter Grünberg, the variation of the resistance of the GMR as a function of chromium [9].*

What is the more, GMR is the change in electrical resistance in response to an applied magnetic field. It was discovered that the application of a magnetic field to (Fe/Cr) multilayer resulted in a significant reduction of the electrical resistance of the multilayer. This effect was found to be much larger than either ordinary or anisotropic magneto-resistance and was, therefore, called GMR. A similar, though diminished, effect was simultaneously discovered in (Fe/Cr/Fe trilayers). High magneto-resistance values can also be obtained in other magnetic multilayers, such as (Co/Cu). The change in the resistance of the multilayer arises when the applied field aligns the magnetic moments of the successive ferromagnetic layers, as is illustrated in figure 1.4[8, 10].

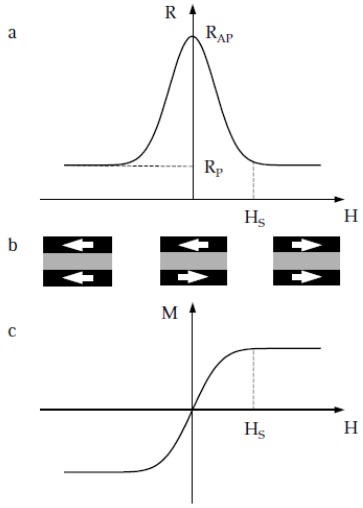


***Figure 1.4:*** *Schematic representation of the GMR effect. (a): Change in the resistance of the magnetic multilayer as a function of applied magnetic field. (b): The magnetization configurations (indicated by the arrows) of the multilayer (trilayer) at various magnetic fields: the magnetizations are aligned antiparallel at zero field; the magnetizations are aligned parallel when the external magnetic field H is larger than the saturation field $H_S$. (c): The magnetization curve for the multilayer [10].*

In the absence of the magnetic field the magnetizations of the ferromagnetic layers are antiparallel. Applying the magnetic field, which aligns the magnetic moments and saturates the magnetization of the multilayer, leads to a drop in the electrical resistance of the multilayer? [10].

## 1 - 3 - The magnetization and applications

### 1 - 3 - 1 The tunneling magneto-resistance TMR.

A magneto-resistance effect similar to the GMR. The tunnel magneto-resistance (TMR) has been observed in tunnel junctions (metal / insulator / metal). In which the two ferromagnetic electrodes: free layer and trapped layer are separated by a thin insulating layer, this layer, called barrier tunnel with a thickness of nanometer [11].

The trapped layer acts as a reference layer and its magnetization being fixed either by coupling with a strongly antiferromagnetic layer, or because of its hard magnetic character.

Where ferromagnetic layer keeps the ability to change its orientation depending on the applied magnetic field.

A similar behavior is observed, then, a large variation in the resistance of the junction when applying a voltage to the terminals of the TMR, the relative direction of magnetization of the free ferromagnetic layer varies, which involves a significant variation in magneto-resistance at room temperature which is three times the giant magneto-resistance. This behavior in a magnetic tunnel junction with a state that allows storing one bit of information, a principle that is used in magnetic random access memory (MRAM). Tedrow et al. talked about spin-dependent tunnelling into ferromagnetic nickel [12].

To explain the TMR. A model based on two hypotheses was created; the first one is that the spin of the electron is preserved during tunnel transportation. Where the second is that the probability of transmission of electrons through the barrier is proportional to the density of states at the Fermi level in the receiver electrode. The number of the electrons candidate to pass is proportional to the density of states at the Fermi level in the emitter electrode. The existing for each spin channel is proportional to the product of the density of states at the Fermi level of the two electrodes.

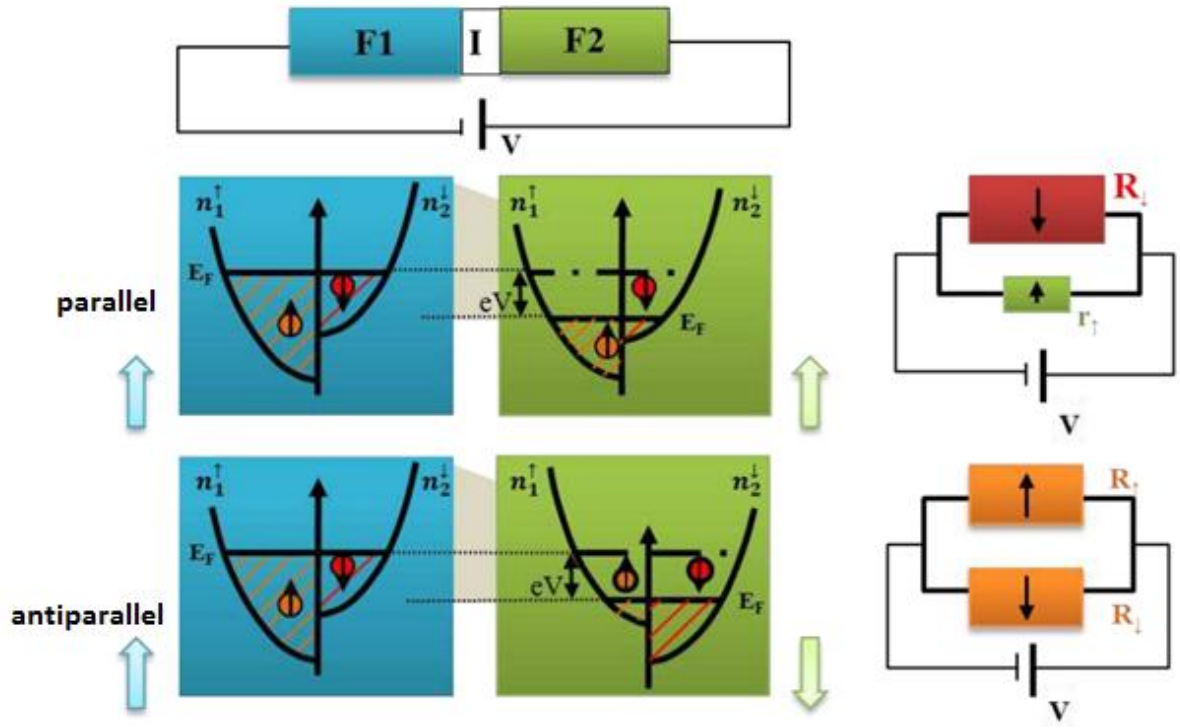


***Figure 1.5:*** *tunneling effect between two ferromagnetic layers F1 and F2 separated by an insulating barrier I of deformed rectangular potential by applying a voltage V.*

Figure 1.5 is a simple representation of this model. The densities of states of majority and minority spin electrons ($n_\uparrow$, $n_\downarrow$) are represented by parabolas shifted into energy. This energy shift induces a polarization P of ferromagnetic materials:

$$P = \frac{n_\uparrow - n_\downarrow}{n_\uparrow + n_\downarrow} \qquad \textbf{(1.1)}$$

For the parallel configuration of the magnetizations of the two ferromagnetic materials, the density of states at the Fermi level of the majority spin electrons is important in the transmitter electrode F1 and in the receiver electrode F2. The corresponding resistance is then low $r_\uparrow$ for this spin channel, while the density of states at the Fermi level of the minority spin electrons is low in both electrodes. The tunnel resistance $R_\downarrow$ in this case is important. Therefore, the current is mainly due to the majority spin channel.

The total resistance of the magnetic tunnel junction in the parallel state is given by:

$$R_{\uparrow\uparrow} = \frac{r_\downarrow . R_\uparrow}{r_\downarrow + R_\uparrow} \qquad \textbf{(1.2)}$$

In the configuration of anti-parallel magnetization, the density of states at the Fermi level of the majority or minority spin electrons is low in either the emitter electrode F1 or F2 the receiver electrode. Both channels lead equivalently and generally lower than in the case of parallel magnetization. For that reason, the tunnel resistances of the majority $R_{\uparrow}$ and the minority $R_{\downarrow}$ electrons spins are averages. The total resistance of the magnetic tunnel junction in the anti-parallel configuration is:

$$R_{\uparrow\downarrow} = \frac{R_{\downarrow}.R_{\uparrow}}{R_{\downarrow} + R_{\uparrow}} \qquad \textbf{(1.3)}$$

The low resistance $r_{\uparrow}$ makes $R_{\uparrow\uparrow}$ weaker than $R_{\uparrow\downarrow}$. A configuration change of the magnetization from a parallel state to an anti-parallel state causes then a change in electrical current through the tunnel barrier.

By 1995, Moodera et al. [13] have observed a consistent TMR at room temperature measured on junction of: CoFe / $Al_2O_3$ / Co or NiFe / $Al_2O_3$ / Co. The TMR has reached 11.8% at 295 K.

The TMR is defined as the relative variation in the resistance of the system between its two extreme values:

$$TMR = \frac{R_{\uparrow\downarrow} - R_{\uparrow\uparrow}}{R_{\uparrow\uparrow}} = \frac{G_P - G_{AP}}{G_{AP}} = \frac{\left(n_1^{\uparrow}n_2^{\uparrow} + n_1^{\downarrow}n_2^{\downarrow}\right) - \left(n_1^{\uparrow}n_2^{\downarrow} + n_1^{\downarrow}n_2^{\uparrow}\right)}{n_1^{\uparrow}n_2^{\downarrow} + n_1^{\downarrow}n_2^{\uparrow}} = \frac{2P_1P_2}{1 - P_1P_2} \qquad \textbf{(1.4)}$$

Where G is the electrical conduction of the junction, and $G_P$ isrelated to parallel magnetization configuration and $G_{AP}$ is connected to anti-parallel magnetization configuration.

For n, the $n_i^{\uparrow}$ and $n_i^{\downarrow}$ (where i = 1 or 2) are the densities of states of majority and minority spin electrons in each electrode, and $P_j$ (where j = 1 or 2) is the polarization of the current in each of the electrodes at the Fermi level. This quantity is dimensionless and we frequently use percentage.

### 1 - 3 - 2 The magnetic random access memories MRAM

Via GMR, also the possibility of controlling the state of resistance of a spin valve by an electrical field has permitted the realization of non volatile memories having several advantages by combining non volatility of the magnetic storage to electrical writing information and consumes little energy, beside non destructive magnetic read thanks to GMR. It is possible to make submicron size junctions matrices to encode information by a series of (0 and 1), figure 1.6. For low resistance, the (0) state is the parallel configuration. For high

resistance, the (1) refers to the anti-parallel configuration. In practice, the difference between two resistance levels and the fastest the reading of the state is, the non volatility of such magnetic systems and the sub-nanosecond write demonstration enable the consideration of their use as a memory for storing a high reliability and a support for the processing of logical data. Such systems are called MRAM.

The principle of reading a digit bit is passing a current between a word line and a bit line, figure 1.6. The resistance measurement obtained is either the low resistance state or the high one. By applying a voltage between two lines, a set of possible paths for current going through one or more magnetic tunnel junctions are superposed. To avoid this reading problem, a series transistor was added to each cell to be able to address each individually during the reading.

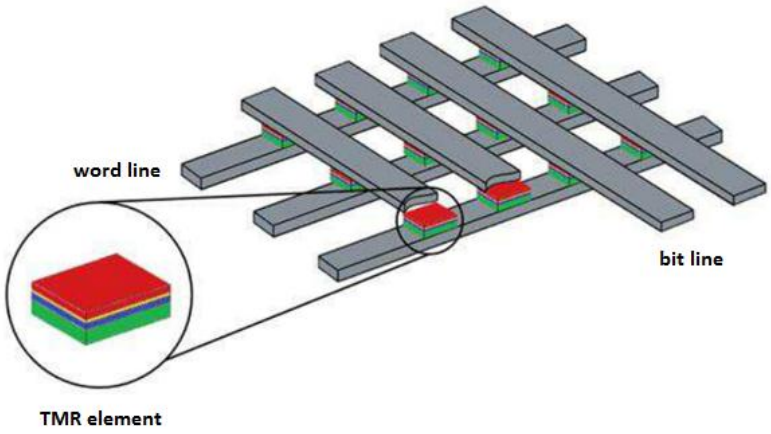


***Figure 1.6:*** *MRAM architecture formed by a matrix of magnetic tunnel junctions [14]*

The MRAM architecture presents a magnetic tunnel junction connected in series with a transistor selector, figure 1.6, a bit line and a word line. Writing is performed by closing the transistor and passing a current through the bit line and the word line that cross at the addressed memory location. This fact creates two orthogonal magnetic fields at the junction. These two fields are able to change the direction of the free layer. Each magnetic field taken independently, does not allow the reversal of the magnetization of the free layer because the magnetic field created at the intersection of the two currents must be greater than the coercively of the free layer.

### 1 - 3 - 3 Spin field effect transistor (SpinFET).

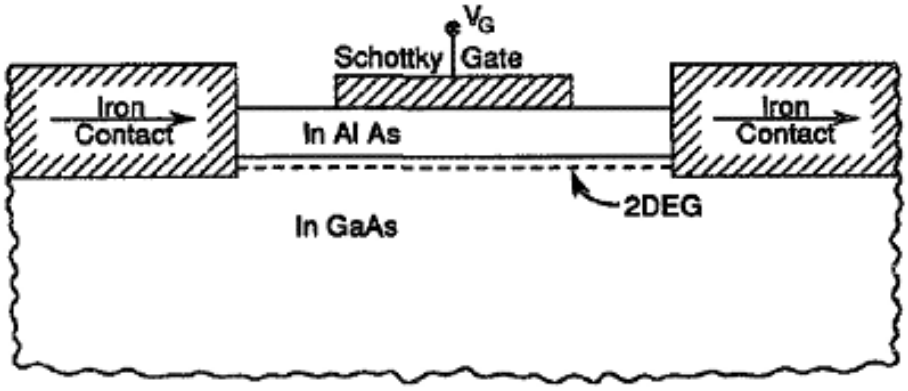


***Figure 1.7:****Schematic illustration of the spin field-effect transistor Datta and Das [15]*

The figure 1.7 is presented the illustration of the spin field-effect transistor (SpinFET). The current in the channel is spin polarized, and it processes under the action of electric field created by the gate by Rashba-Bychkov coupling. Thus, the amount of current flowing through the transistor varies depending on the gate voltage.

The SpinFET is a future semiconductor spintronics device promising to deliver a performance superior to that achieved with present transistor technology. SpinFETs are composed of two ferromagnetic contacts presented in source and drain, which sandwich the semiconductor region is sandwiched. Ferromagnetic contacts contain mostly spin-polarized electrons and play the role of polarizer and analyzer as described by Datta and Das [15]. The ferromagnetic source contact injects spin-polarized electrons into the semiconductor region. Because of the non-zero spin-orbit interaction the electron spin processes during the propagation through the channel [16-17].

At the drain contact only the electrons with spin aligned to the drain magnetization can easily leave the channel and contribute most to the current. Thus, the total current through the device depends on the relative angle between the magnetization direction of the drain contact and the electron spin polarization at the end of the semiconductor channel. Current modulation is achieved by tuning the strength of the spin-orbit interaction in the semiconductor region and thus the degree of the spin precession. Importantly, the strength of the spin-orbit interaction in

the channel depends on the effective electric field and can be controlled by the voltage applied to the gate [18-23].

## 1 - 4 - Diluted magnetic semiconductors (DMS)

Related to the transition metal (TM), many studies have been spread on dilute magnetic semiconductors (DMS). Mainly Mn doped (II-VI, IV-VI and II-V) compound semiconductors. Classical examples are II-VI (Cd,Co)Se; (Zn,Mn)Se; (Hg,Fe)Te…And IV-VI: (Pb,Mn)Te ; (Sn,Mn)Te ; (Pb,Eu)Te…

Thanks to much lower solubility of magnetic ions in (III-V compared to II-VI) semiconductors, along with its poor stability, not much studies are done on ( III-V diluted semiconductors) [24]. A step was made by using molecular beam epitaxy. By technical methods and procedures, where III-V material InMnAs, and ferromagnetism was observed in p-type InMnAs [25].

In fact, the first Mn doped dilute magnetic semiconductor (Ga,Mn)As was made by Ohno [26], where the system was grown as a $Ga_{1-x}Mn_xAs$ (x = 0.015 - 0.017) thin film on a semi insulated GaAs (001) substrate. So, the (Mn-doped III–V) $In_{1-x}Mn_xAs$ and $Ga_{1-x}Mn_xAs$[27]showed ferromagnetism at higher temperature.

This effect has motivated a continuous search for mediated ferromagnetism with higher temperatureand led to the conjecture that oxide based DMS would be key materials in the development of spintronic devices.

It was pointed out that the capability of high electron doping and the rather heavy effective electron mass of oxide semiconductors could be quite efficient to realize high Curie temperatures [28].

On the other hand, many oxide based DMSs are wide (band gap semiconductors >3eV), which can add an optoelectronic dimension to the new generation of spintronic, the revolutionary was the discovery of room temperature (RT) ferromagnetism in Co doped $TiO_2$ [29-30]. subsequently, a considerable number of investigations in other oxide based DMS ($SnO_2$[31];$In_{1.8}Sn_{0.2}O_3$[32]; Cu2O[33]; and ZnO[34] etc.) occurred and reported a high $T_C$.

Related to $ZrO_2$, the 25% of Mn incorporated in this later indicated, 570 K as a $T_C$,[35]. Theoretically , $ZrO_2$ was investigated by Boujnah [36], where (V, Mn and Fe) doped $ZrO_2$ are stabilized in the FM state with high stability. Mn-doped $ZrO_2$ has higher FM stability than any

of the other doped systems. Then Mn-doped $ZrO_2$ in cubic structure was found to be a potential high-Curie temperature.

For $FeS_2$ (pyrite), many studies devoted in connection to magnetic properties of ($CoS_2$, $FeS_2$, $NiS_2$ and $Fe_xCo_{1-x-y}Ni_yS_2$)[37] ferromagnetic (F), antiferromagnetic (AF ) and paramagnetic (P) phases were found. Also, an experimental and computational investigation of magnetism in pyrite $Co_{1-x}Fe_xS_2$ in viewpoint of chemical bonding and half metallicity [38].

## 1 - 5 - Interest of oxides and pyrite.

The challenge was to find DMS which operates at RT such as dilute magnetic oxides (DMO) which are obtained by substituting atoms of no doped semiconductor with impurities of one or more magnetic elements such as the ions of the series of TMs at very low concentrations. See table 1.1.

| Materials | $E_g$ (eV) | Dopant (x%) | Moment ($\mu_B$/3d ion) | $T_C$ (k) |
|---|---|---|---|---|
| $SnO_2$ | 3.5 | Co5% | 0.3 | 650 [33] |
| | | Fe 5% | 1.8 | 610 [39] |
| $ZrO_2$ | 6.1 | Mn 25% | 3.45 | 570 [35] |
| $TiO_2$ | 3.2 | Co 1-2% | 1.4 | >650[40]. |
| | | Co 7% | 0.3 | >300[29] |
| | | V 5% | 4.2 | >400[41] |
| | | Fe 2% | 2.4 | 300 [42] |
| $Cu_2O$ | | Co 5% - Al 0.5% | 0.2 | >300 [33] |
| $In_2O_3$ | 2.9 | Cr 2% | 1.5 | 900 [43] |
| | | Fe 5% | 1.4 | >600 [44] |

***Table 1.1:*** *Data of some oxides with high $T_C$*

## 1 - 6 - Reasons and motivations to consider $SnO_2$ (rutile), $ZrO_2$ (zirconia) and $FeS_2$ (pyrite) as a matter of our research.

According many studies, investigations and elaborations, dilute magnetic oxides (DMO) and their applications are incorporated in many fields and specializations. These kinds of materials, combine can combine optical transparency with a high $T_C$ and semi conducting behavior beside high temperature ferromagnetism.[45]. Where, $SnO_2$ has diverse optical and electrical properties [46].

These properties are suitable in many fields as in thin solid films and photovoltaic devices.It should be noted that $SnO_2$ is n-type semiconductor [47], Including a direct wide band gap with $E_g$= 3.6 eV[48]. For this reason many efforts have been devoted to study the magnetic properties of $SnO_2$ doped and co-doped with various transition metals (Co, Cr, Fe, W, F, etc. ), [48-57].

For zirconium dioxide ($ZrO_2$), it is a ceramic material of importance technological potentials due to its outstanding electrical properties with high dielectric constant and wide band gap. The applications of such a material appear in many fields like gas sensors, solid fuel cells, high durability coating, and catalytic agents [58-59]. This material with 25% of Mn, has a $T_C$ of 570 K [35].

Furthermore, it is proposed to replace $SiO_2$ in advanced metal oxide semiconductor devices in gate stack, dynamic access memory devices, and optical applications [58, 60-63]. Besides that, this material involves a large band-offset in direct contact with Si and good thermal stability.

The sulfides ($MnS_2$ hauerite , $FeS_2$ pyrite, $NiS_2$ vaesite…etc) have many proprieties, electrical and magnetic and connected to many areas of potential technological exploitation in photovoltaics and in solar energy conversion devices, magnetic recording devices, etc... [64].

The $FeS_2$ pyrite is a good candidate for optoelectronics or photovoltaic cells that require a material with excellent environment compatibility, low production cost for photocurrent generation and high quantum efficiency [65-70].

## 1 - 7 - Exchange interaction mechanisms

### 1 - 7 - 1 Direct exchange

Direct exchange occurs when there is direct overlap of the wave functions of electron associated with nearest neighbor magnetic atoms. In addition, the direct exchange can also be understood in terms of the Pauli principle and the Coulomb repulsion. Where the Coulomb energy is lowered if the spins of the electrons are parallel, because for parallel spin alignment the electrons avoid each other better than antiparallel alignment. This interaction is called d-d coupling exchange. For DMS, This is a direct interaction that occurs between the magnetic elements impurities in without any intermediary.

For all the (i, j) pairs of atoms of the many-electron system, the generalization of the Heisenberg Hamiltonian in which the sum is taken over the exchange Hamiltonians is

$$H = -\sum_{i,j} J < \overrightarrow{S_i}.\overrightarrow{S_J} > \qquad \textbf{(1.5)}$$

**J** (**$R_i$-$R_j$**) represents a coupling between **$S_i$** et **$S_j$** spins located at **$R_i$** et **$R_j$** sites.

### 1 - 7 - 2 Inderect exchange or Ruderman, Kittel, Kasuya and Yoshida (RKKY) interaction

The dominant exchange interaction in metals is indirect exchange couples moments over relatively large distances, there is little or no direct overlap between neighboring electrons. That consequently acts throughout an intermediary, which in metals are the conduction electrons. This kind of exchange is better known as the RKKY interaction.

The RKKY interaction applied to DMS to calculate the indirect exchange interaction between localized magnetic moments, carried by electrons and holes from impurities [71].

The RKKY is a very strong indirect exchange interaction between the localized moments carried by the 4f orbital of rare earth realized within conduction electrons.

The RKKY exchange coefficient ($J^{RKKY}$) depends on the distance between two magnetic ions, alternatively ferromagnetic and antiferromagnetic. This mechanism has been applied to explain the ferromagnetic or antiferromagnetic coupling between two thin layers of a ferromagnetic metal separated by a thin layer of a nonmagnetic metal. The RKKY interaction coupling represented in the following expression:

$$J^{RKKY}(r) = J_0 e^{\frac{-r}{l}} r^{-4}\left[\sin(2K_F r) - 2K_F r\cos(2K_F r)\right] \text{[72]} \quad \textbf{(1.6)}$$

$$\text{Where } J_0 = \frac{(N_0\beta)^2 m^*}{4\eta^2(2\pi)^3} \quad \textbf{(1.7)}$$

$$N_0\beta = \frac{\Delta E_v}{x_{TM} < S >} \quad \textbf{(1.8)}$$

Where $K_F = (3/2\pi^2 n_c)^{1/3}$ is the Fermi wave number. And $n_c$ is the hole density. $J_0 > 0$ is related to the local Zener coupling $J_{pd}$ between the *TM* (transition metal) local moments and the hole spins.

$\Delta E_v$ is the band edge spin splitting of the VB, which was calculated by band structure calculation. And $< S >$ is the average *TM* spin and $m^*$ is the hole effective mass.

The RKKY exchange coefficient $J_0$ oscillates from positive to negative as the separation of the ions changes and has the damped oscillatory, figure 1.8. Hence, depending upon the separation between a pair of ions their magnetic coupling can be ferromagnetic or antiferromagnetic.

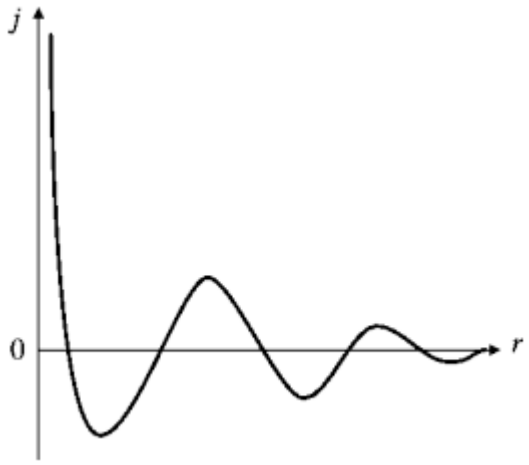


***Figure 1.8:*** *Variation of indirect exchange coupling constant J of a free gas electron in the vicinity of a magnetic moment point from the origin r = 0.*

### 1 - 7 - 3 Zener's exchange

With the impurity concentration, Zener's p-d exchange exhibits an energy gain with increased linearly. Because the effects of different impurities on the shift of the valence band superimpose each other, the energy shifts due to hybridization and can be treated in first order perturbation theory [73].

From figure 1.9, the d states hybridize with the valence band p, push the majority valence band to higher energies while the minority valence states are pushed to lower energies by the minority d states of the impurity.

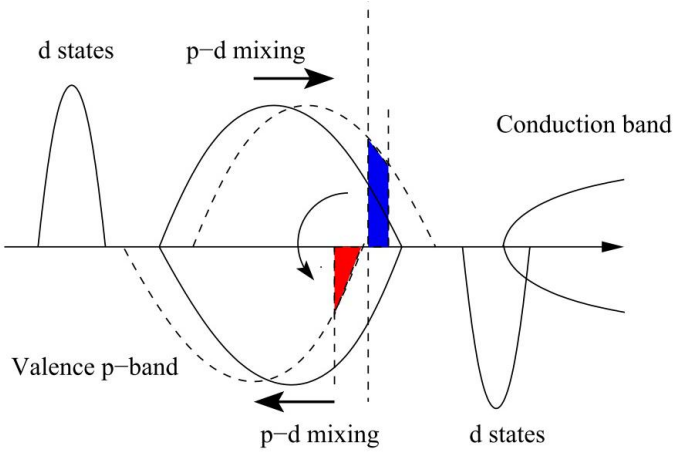


***Figure 1.9:*** *Schematic diagram of p-d exchange related to the spin polarized DOS. The majority d-level lies below the valence p-band and the minority level above.*

### 1 - 7 - 4 The double-exchange mechanism

The double-exchange mechanism is a type of a magnetic exchange that may arise between ions in different oxidation states.

This interaction occurs through the exchange of an electron from the 3d shell between the cation of the same kind but of different valences, where an intermediary of a non-magnetic element (oxygen ions) to transport electrons between the cations which are separated by a large distance, where the direct-exchange (cation-cation) is zero.

Related to Mn-O-Mn interaction, figure 1.10[74], we consider the 180°, in which the $e_g$ of Mn are directly interacting with the 2p of O, and one of the Mn ions has more electrons than the other. In the ground state, electrons on each Mn ion are aligned according to the Hund's rule.

In Mn-O-Mn interaction, O provides its spin-up electron to $Mn^{4+}$, after that, its orbital can be filled by another electron existed in $Mn^{3+}$.

This process is supposedly similar to super-exchange. Though, in superexchange, a ferromagnetic or antiferromagnetic alignment occurs between two atoms with the same number of electrons. Where in double-exchange, the interaction occurs only when one atom has an extra electron compared to the other [75].

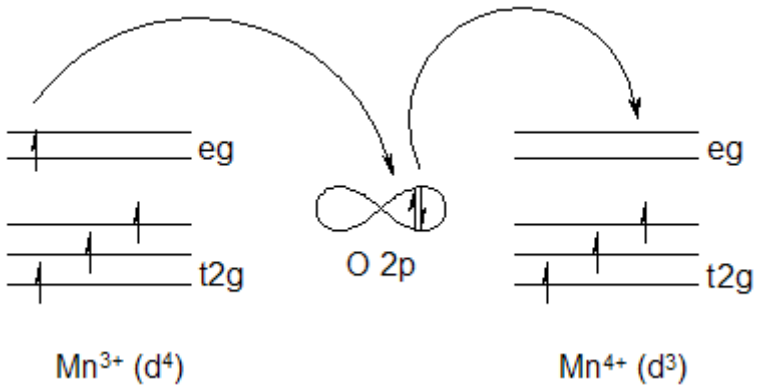


***Figure 1.10:*** *an electron from the Mn4 $^{+}$ ion jumps to O, the O gives an electron to the other Mn ion. This is possible only if the two Mn ions have their spins Parallel*

### 1 - 7 - 5 Super-exchange mechanism

The antiferromagnetism by super-exchange interaction has been shown for crystals of LaMnO [76]. The transition magnetic moments located on adjacent cationic sites interact via a nonmagnetic atom which provides exchange carrier [77].

In addition, the super-exchange interaction has been formalized by Goodenough et al. [78], which resulted in the Goodenough-Kanamori rules. The ion of the transition series metals in a tetragonal crystal field undergoes lifting degeneration (3d electronic) levels into 2 groups separated by the energy of the crystal field. That crystal field included doubly lowest energy ($e_g$) and higher triply energy denoted ($t_{2g}$).

For an octahedral symmetry, the triplet lowest energy and doublet higher energy are ($t_{2g}$) and ($e_g$), respectively.

Basically, the Pauli Exclusion Principle believes that between two magnetic ions with half occupied orbitals, which couple through an intermediary non magnetic ion such as oxygen, the super exchange will be strongly antiferromagnetic while the coupling between an ion with a filled orbital and one with a half filled orbital will be ferromagnetic. The coupling between an ion with either a half filled or filled orbital and one with an empty orbital can be either antiferromagnetic or ferromagnetic [79].

For the $e_g$ connected to (cation-anion-cation at 180°), the 2 cations have orbital $e_g$ half occupied pointing in the direction of the anion, the coupling is direct by the rules of Hund and gives strong antiferromagnetism. If the two of $e_g$ orbitals are empty, that gives antiferromagnetism but weak.
For a weak ferromagnetic, a cation has an orbital $e_g$ half occupied and the other empty. In this case, the electron in question can virtually switch from a cation to another provided that both cations have their parallel spins.

## 1 - 8 - View and origins of magnetism

By 1819, Oerstead accidentally made the connection between magnetism and electricity discovering that a current carrying wire deflected a compass needle [80].

Later, in 1906, Weiss proposed the ferromagnetic theory [81]. During 1920's, the physics of magnetism was developed with theories involving electron spins and exchange interactions.

The electricity is the movement of electrons, whether in an atom or in wire. Then, each atom represents a tiny permanent magnet in its own background. The circulating electron produces its own orbital magnetic moment, measured in Bohr magnetons ($\mu_B$), and there is also a spin magnetic moment associated with it due to the electron itself spinning, like the earth, on its own axis, figure 1.11.

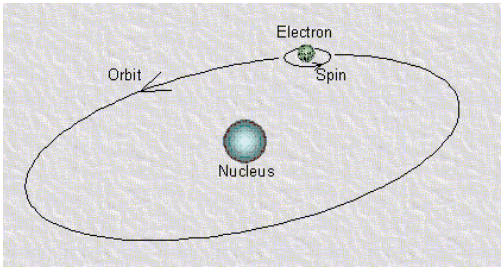


***Figure 1.11:****The orbit of a spinning electron about the nucleus of an atom*

In most materials, there are resultant magnetic moments, due to the electrons being grouped in pairs causing the magnetic moment to be cancelled by its neighbor.

Regard to magnetism fact, this later token place on the sub-atomic level from localized polarization of the electron clouds of certain atoms arising from unpaired electrons. That causes the charge on the atom to have a net angular momentum. Any flow of charge causes additional physical effects on the surroundingsas a magnetic effect. The magnitude of that

magnetic or spin moment is dependent on the species of atom [82]. When atoms are brought in proximity to each other there is a probability of an electron jumping from one atom to another, recognized as the Heisenberg exchange [83].

This interaction probability can indirectly couple the spin moments of the atoms, causing the spin moments to align parallel or anti-parallel.

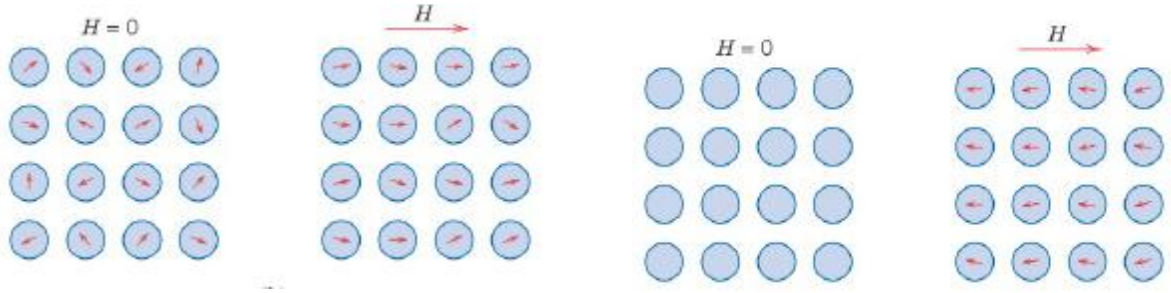


a b

***Figure 1.12:*** *(a) Atomic dipole configuration with and without an external magnetic field for a paramagnetic material.*

*(b) a diamagnetic material without a magnetic field. In the presence of a field, dipoles are induced that are aligned opposite to the field direction.*

In most materials, the spin moments are small and aligned randomly, leading to paramagnetism as shown in figure 1.12 (a). For diamagnetism, it is a very weak form of magnetism that is nonpermanent and persists only while an external field is being applied, and it is induced by a change in the orbital motion of electrons due to an applied magnetic field. The magnitude of the induced magnetic moment is extremely small, and in a direction opposite to that of the applied field as shown in figure 1.12 (b).

In the absence of an external field, metallic materials possess a permanent magnetic moment and manifest very large and permanent magnetizations. In terms of ferromagnetism they are displayed by the transition metals iron as Ni, Co and some of the rare earth material such as Gd. In fact, the spin moments are large, and align in parallel. This is schematically illustrated in figure 1.13 (a).

The magnetic moment coupling between adjacent atoms or ions occurs in materials other than those that are ferromagnetic. In one such group, this coupling result in an antiparallel

alignment; the alignment of the spin moments of neighboring atoms or ions in exactly opposite directions is termed antiferromagnetism. Manganese oxide (MnO) is one material that displays this behavior as presented in figure 1.13 (b). Then, the magnetic structure is composed of two magnetic sublattices (called A and B) separated by oxygens. The exchange interactions are mediated by the oxygen anions. When this happens, the interactions are called indirect or superexchange interactions. The strongest superexchange interactions result in an antiparallel alignment of spins between the A and B sublattice

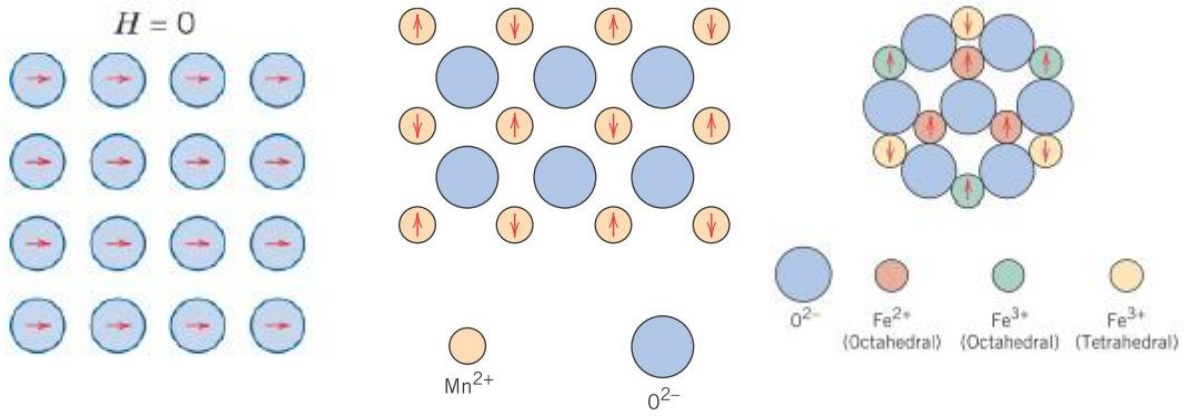


***Figure 1.13:****(a) Schematic illustration of the alignment of atomic dipoles for a ferromagnetic material, even in the absence of an external magnetic field. (b) Representation of antiparallel alignment of spin magnetic moments for antiferromagnetic manganese oxide (MnO).(c) A diagram showing the spin magnetic moment configuration for* $Fe^{2+}$ *and* $Fe^{3+}$ *ions in* $Fe_3O_4$

In ferrimagnets, figure 1.13 (c), the magnetic moments of the sublattices of those (A and B) are not equal and result in a net magnetic moment. So, ferrimagnetism is therefore similar to ferromagnetism, it exhibits the characteristic of the behavior spontaneous of ferromagnetic magnetization, hysteresis, remanence and Curie temperatures. In fact, all materials can be classified in terms of its magnetic behavior. Ferromagnets and ferrimagnets have very different magnetic ordering. The common types of magnetism are diamagnetism and paramagnetism, which account for the magnetic properties of most of the periodic table of elements at room temperature. Usually, these elements are referred to as non magnetic. At room temperature, the only other type of magnetism observed in pure elements is antiferromagnetism. Magnetic materials can also be classified as ferrogmatic, but this behavior is not observed in pure element. Nevertheless can also be found in compounds (the mixed oxides, known as ferrite) from which ferrimagnetism derives its name.

The various types of behaviors are illustrated in table 1.2. And the value of magnetic susceptibility falls into a particular range for each type of material and this is shown in table 1.3 with some examples.

| Type | Atomic / Magnetic Behaviour | |
|---|---|---|
| Dia-magnetism |  Atoms have no magnetic moment | 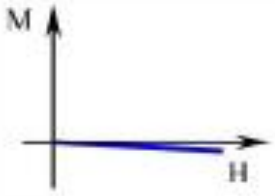  |
| Para-magnetism | 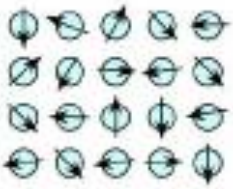 Atoms have randomly oriented magnetic moments | 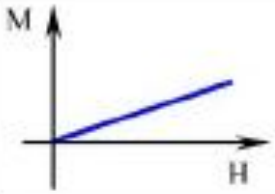  |
| Ferro-magnetism | 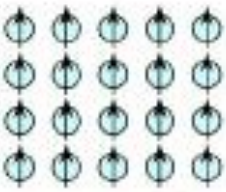 Atoms have parallel aligned magnetic moments | 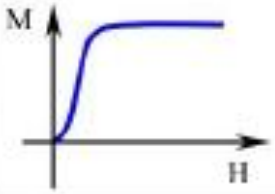  |
| Antiferro-magnetism | 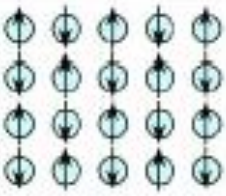 Atoms have anti-parallel aligned magnetic moments | 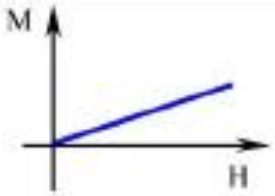  |
| Ferri-magnetism | 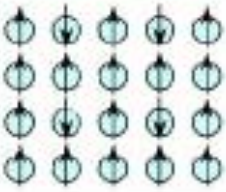 Atoms have mixed parallel and anti-parallel aligned magnetic moments | 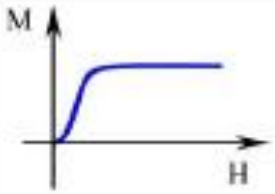  |

***Table 1.2:*** *A summary of the different type of magnetic behavior*

| Type of magnetism | Susceptibility | Example | |
|---|---|---|---|
| Diamagnetism | Small and negative | Au | $-2.74 \times 10^{-6}$ |
| | | Cu | $-0.77 \times 10^{-6}$ |
| Paramagnetism | Small and positive | $\beta$-Sn | $00.19 \times 10^{-6}$ |
| | Small and positive | Pt | $21.04 \times 10^{-6}$ |
| | Small and positive | Mn | $66.10 \times 10^{-6}$ |
| Ferromagnetism | Large and positive function of applied field, microstructure dependent | Fe | Up to ~ 100,000 |
| Antiferromagnetism | Small and positive | Cr | -- |
| Ferrimagnetism | Large and positive function of applied field, microstructure dependent | Ferrite | Up to ~3 |

***Table 1.3:*** *Susceptibility at room temperature for each type of magnetic material.*

# Part 2: Theoretical framework insights ab-intio method.

In the present work, we restricted our study to the bulk materials, where the possible surface effects are excluded. We are considering the bulk to be an infinite crystal material for all numerical simulations.

## 2 - 1 - Schrödinger equation for many-body problem

Numerical simulations based on so-called ab initio calculation have gained a well-known place in modern and condensed matter physics. They can be used to guide or to plan future experiments by means of a rational process.

In order to investigate the properties of molecules, atoms and solids, the so-called Schrödinger equations is the basic tool that the solid state theorist works with. The time-independent Schrödinger equation has the form:

$$\hat{H}\Psi = E\,\Psi \qquad \textbf{(2.1)}$$

where $\Psi$ is the many-body wave-function, Eis the total energy and $\hat{H}$is the Hamiltonian of system.

The Hamiltonian can be written as a sum of five terms as follows:

$$\hat{H} = T_{core} + V_{core-core} + T_e + V_{e-e} + V_{core-e} \qquad \textbf{(2.2)}$$

Given that

$T_{core} = -\sum_{k=1}^{N_0} \frac{1}{2M_k} \Delta_{R_k}$ is the kinetic energy of the nuclei

$V_{core-core} = +\sum_{k<k'} \frac{Z_k Z_{k'}}{R_{kk'}}$ is the interaction energy between the nuclei

$T_e = -\sum_{i=1}^{N} \frac{1}{2} \Delta_{r_i}$ is the kinetic energy of the electrons

$V_{e-e} = +\sum_{i<j'} \frac{1}{r_{ij}}$ is the interaction energy between electrons

$V_{core-e} = -\sum_{k,i} \frac{z_k}{r_{ik}}$ is the interaction energy between electrons and nuclei

In the above terms, the distance between *i*-th and *j*-th electron is: $r_{ij} = |r_i - r_j|$ , the distance between *i*-th elextron and *k*-th nucleus is: $r_{ik} = |r_i - R_k|$ and the distance between the *k*-th nucleus and *k'*-th nucleus is :$R_{kk'} = |R_k - R_{k'}|$. In atomic units, the energy in Hartee and the length in Bohr.

With:

- $N_0$ is the total number of nuclei in the system and $N$ is the total number of electrons in the system.

- The indexes $k$ and $k'$ refer to the nuclei.

- The indexes $i$ and $j$ refer to the electrons.

- $r_i$ is the position of the electron $i$.

- $R_k$ is the position of the nucleus $k$.

- $Z_k$ is the charge of the nucleus $k$.

In fact, it is not possible to solve this equation and there are many difficulties underlying the application of this technique to different classes of system, so, the use of approximations and methods are required. For example, the solid system is described by many electron wave functions $\Psi(x_1, x_2, \ldots\ldots x_{N-1}, x_N)$ which become very complicated where each $x_i$ determinates the position and spin of each particle, given that, the Schrödinger equation should to solve $10^{23}$ simultaneous different equations.

## 2 - 2 - The Born-Oppenheimer approximation

The Born-Oppenheimer approximation [84] has an essential role in electronic structure calculations. The underling rationalization of this approximation is that the mass of nuclei is already 1835 times the mass of an electron (case of the hydrogen atom). According to that, they assumed that the nuclei move much more slowly than electrons, subsequently, we can considered the electrons are moving in a field produced by the fixed nuclei. Base on Born-Oppenheimer approximation, the $T_{core}$ and $V_{core-core}$ operators are neglected in equation **(2.2)**, where the repulsion between nuclei, can be considered as a constant for a fixed configuration of the nuclei, subsequently, the remaining part of the equation **(2.2)** is called the electronic Hamiltonian, noticed $\hat{H}_{elec}$.

$$\hat{H}_{elec} = T_e + V_{e-e} + V_{core-e} \qquad \textbf{(2.3)}$$

At this stage the expression of the electronic wave function is:

$$\Psi_{elec} = \Psi_{elec}(r_i, R_k) \qquad \textbf{(2.4)}$$

Even Born-Oppenheimer approximation permits to separate the Schrödinger equation into independent electronic and nucleonic parts, the solving of this for electronic part is still theoretically a very complicated. Subsequently the uses of approximations besides methods are required.

## 2 - 3 - Hartree-Fock approximation

The Hartee-Fock (HF) approximation has a remarkable position, since it is facilitating the way to more accurate calculations, thus, it is useful to solve the electronic wave function related to equation **(2.4)**. The HF approximation is used to investigate various the problems connected to materials science, as defects in solids [85] and electronic structure of insulators [86].

Even the HF approximation provides an exact description of electron exchange and includes the electron spins, it is ignored the electrons correlation property. Then, the energy associated with this approach must be different from the exact energy by an energy difference, which is called the correlation energy. Known that the movement of a given electron affects and is affected by the movement of the other particles. Then, this is the major limitation of the HF approximation, for atoms and small molecules. While this approximation is still going on in terms of the total energy error, the limitation could be around 0.5% in a carbon atom, where the total energy is around 1000 eV, which already reaches the order of magnitude of chemical single bond energy. That is to say, to obtain a reliable description of chemical reactions, more approximations are required. This can be achieved within the wave-function based approximations and by making more elaborate methods for the many-body wave function, such as the configuration Interaction (CI) method [87], also the Møller-Plesset (MP) perturbation theory[88], and the Coupled-Cluster (CC) method [89] have achieved the greater success in the last years.

## 2 - 4 - Density functional theory

Density functional theory (DFT) is a popular and successful computational quantum mechanical modeling method used in physics, materials science and chemistry. It is to study the electronic structure of many-body systems, such as molecules and atoms. The basic concept of DFT is to deal with a formulation of this many-electron problem that involves the total density of electrons instead of using the many-electron wave function in that formulation

without any loss of information. In fact, Thomas [90] and Fermi[91] proposed the earliest form of DFT. Additionally, in 1964 Hohenberg and Kohn [92] demonstrated the fundamental importance of the electronic density in their theorems. After that, in 1965, Kohn and Sham [93], further developed the theory into a framework for real calculations. In many cases the results of DFT calculations for solid state studies agree quite acceptably with experimental data.

### 2 - 4 - 1 Thomas-Fermi-Dirac theory

The earliest model of density functional theory proposed in 1927 by Thomas and Fermi. This model is Thomas-Fermi (TF), which used the electron density $\rho(r)$ as the basic variable instead of the wave function.

The total energy is represented, by terms defining the kinetic energy, the Coulomb interactions of electron-electron (internal potential), nucleus-electron (external potential ), as an explicit functional of the total density of electrons. In an external potential $V_{ext}(r)$, the total energy of the system is given as a functional of the electron density ρ(r), its expression is:

$$E_{TF}[\rho] = C_F \int \rho^{\frac{5}{3}}(r)dr + \int \rho(r)V_{ext}(r)dr + \frac{1}{2}\iint \frac{\rho(r_1) - \rho(r_2)}{|r_1 - r_2|} dr_1 dr_2 \qquad \textbf{(2.5)}$$

Where the first, second and third terms are: the kinetic energy of the non-interacting electrons in the homogeneous electron gas model (HEG). The classical electrostatic energy of the nucleus-electron Coulomb interaction and the classical electrostatic Hartree energy approximated by the classical Coulomb repulsion between electrons.

With $C_F = \frac{3}{10}(3\pi^2)^{\frac{5}{3}} = 2.871$

And the electron density $\rho(r) = N \int \dots \int |\Psi(x_1, x_2, \dots, x_N)|^2 dx_1 dx_2 \dots dx_N$ **(2.6)**

When $\rho(r)$ verifies the probability of finding any of the $N$ electrons within the volume $r$, however, with arbitrary spin with N-1 electrons have arbitrary positions and spin in state represented by wave function. Given that $x_i$ represents both spatial and spin coordinates.

Dirac [94] extended the equation **(2.5)** by adding a local exchange term $C_D \int \rho^{\frac{4}{3}}(r)dr$, subsequently, the Thomas-Fermi-Dirac equation is:

$$E_{TFD}[\rho] = C_F \int \rho^{\frac{5}{3}}(r)dr + \int \rho(r)V_{ext}(r)dr + \frac{1}{2}\iint \frac{\rho(r_1) - \rho(r_2)}{|r_1 - r_2|} dr_1 dr_2 + C_D \int \rho^{\frac{4}{3}}(r)dr$$

**(2.7)**

With $C_D = -\frac{3}{4}(\frac{3}{\pi^2})^{\frac{1}{3}}$.

### 2 - 4 - 2 Hohenberg-Kohn theorems

Hohenberg-Kohn (HK) demonstrated that the Thomas-Fermi model is in fact an approximation for an exact theory called DFT. They based on the two fundamental theorems, noticed HK-theorems [92-93] which are mentioned below:

Theorem 1. For any system of interacting particles in an external potential $V_{ext}(r)$, the potential $V_{ext}(r)$ is determined uniquely, except for a constant, by the ground state density $\rho_o(r)$.

Theorem 2. There exists a universal functional $F[\rho(r)]$ of the density, independent of $V_{ext}(r)$, such as the global minimum value of the energy functional, where, the exact ground state energy of the system is

$$E[\rho(r)] = \int \rho(r)V_{ext}(r)dr + F[\rho(r)] \qquad \textbf{(2.8)}$$

The proof of the first theorem is remarkably simple and proceeds by *reductio ad absurdum*. With two different external potentials, $V_{ext}(r)$ and $V'_{ext}(r)$, that give rise to the same density $n_o(r)$. The associated Hamiltonians ($\hat{H}$and $\hat{H}$'), will therefore have different ground state wave functions ( $\Psi$ and$\Psi'$), that each yield $\rho_o(r)$.

With $E_0$ and $E_0$**'**, the ground state related to $\hat{H}$and $\hat{H}$' respectively,

$$E_0 < \langle\Psi'|\hat{H}|\Psi'\rangle = \langle\Psi'|\hat{H}'|\Psi'\rangle + \langle\Psi'|\hat{H} - \hat{H}'|\Psi'\rangle$$

$$= E_0' + \int \rho_0(r)[V_{ext}(r) - V'_{ext}(r)]dr \textbf{(2.9)}$$

Hohenberg-Kohn theorems apply rigorously only to the ground state .Given that:

$$E_0 + E_0' < E_0' + E_0 \qquad \textbf{(2.10)}$$

The ground state density uniquely determines the external potential within an additive constant.

To the proof the second theorem,

The universal functional $F[\rho(r)]$ can be written as the follow:

$$F[\rho(r)] = T[\rho(r)] + E_{int}\,[\rho(r)] \qquad \textbf{(2.11)}$$

The kinetic energy and the interaction energy of the particles are $F[\rho(r)]$ and $E_{int}[\rho(r)]$ respectively, at this point, for the variation principle, the energy functional is:

$$\mathrm{E}[\Psi] = \langle \Psi' | \hat{\mathrm{T}} + \hat{V}_{\cdot int} + \hat{V}_{\cdot ext} | \Psi' \rangle \qquad \textbf{(2.12)}$$

Thus the energy functional **(2.8)** evaluated for the correct ground state density $\rho_0(r)$ is indeed lower than the value of this functional for any other $\rho(r)$. Then by minimizing the total energy functional of the system with respect to variations in $\rho(r)$ , one would find the exact ground state density and energy.

The HK theories are generalized in the theory of spin density functional, with spin degrees of freedom, integrated the particle density and the spin density related to $\rho(r) = \rho\uparrow(r) + \rho\downarrow(r)$ and $S(r) = \rho\uparrow(r) + \rho\downarrow(r)$ , respectively, with ↑and ↓are the different varieties of spin, thus, the energy functional is we generalize into *E[ρ(r),S(r)]*

## 2 - 5 - Kohn-Sham theorem

The HK theorems clarify that the electron density can be uniquely used rather than the wave function to determine the fundamental quantity of the many-body problems. nevertheless, these theorems are still only pure ideas, since the calculating of the kinetic energy of interacting system does not give enough precision.
In 1964, Kohn and Sham (KS) [95] proposed a formalism to calculate *E[ρ]* based on the wave functions, subsequently they decided to describe the idea of one electron orbitals and approximate the kinetic energy of the system by the kinetic energy of non-interacting electrons. In fact, the KS formalism reduces the problem with many electrons to a problem only mono-electronic. Hence, The Kohn-Sham lead to the one electron Schrödinger-like equation called the Kohn-Sham equation which is expressed as:

$$\varepsilon\phi_i = (-\frac{1}{2}\nabla^2 + V_{eff})\phi_i \qquad \textbf{(2.13)}$$

where $V_{eff} = V_{ext} + V_H + V_{xc} = V_{ext}(r) + \int \frac{\rho(r)}{|r_1 - r_2|} dr_2 + \frac{\delta E_{xc}[\rho]}{\delta \rho(r)}$ **(2.14)**

The $\varepsilon$ are the energy of the KS-orbital where $\phi$ are the Kohn-Sham orbitals. Where $-\frac{1}{2}\nabla^2$ and $V_{eff}$ are the kinetic energy of non-interaction reference system and the effective potential. The $V_{eff}$ included the sum of the external potential, the Hartree potential and $E_{xc}$ nge-correlation potential, respectively.

The electron density is $\rho = 2\sum_{i=1}^{\frac{1}{2}N} |\phi_i|^2$ **(2.15)**

Here, the non-interacting kinetic energy is given by:

$$T_S[\rho] = -\sum_{i=1}^{\frac{1}{2}N} \int \phi_i^*(r)\nabla^2\phi_i(r)dr \quad \textbf{(2.16)}$$

For $\varepsilon_i$ energies, the factor 2 is for spin degeneracy, we assume the orbitals are singly occupied. Subsequently, the energy of the non-interacting system, the sum of one-electron eigenvalues is

$$2\sum_{i=1}^{\frac{1}{2}N} \varepsilon_i = T_S[\rho] + \int \rho(r) V_{eff}(r)dr \quad \textbf{(2.17)}$$

For that, the total energy can be obtained from the resulting density throughout:

$$E = 2\sum_{i=1}^{\frac{1}{2}N} \varepsilon_i - \frac{1}{2}\iint \frac{\rho(r_1) - \rho(r_2)}{|r_1 - r_2|} dr_1 dr_2 - \int \rho(r) V_{xc}(r)dr + E_{xc}[\rho] \quad \textbf{(2.18)}$$

The KS equations should be solved self consistently. Within DFT calculations, only the total energy, the Fermi energy and the electron density have a physical meaning. The states and energies of KS are only intermediated calculations.

## 2 - 6 - Exchange-Correlation functional

Many possibilities and approximations are used to solve the Schrödinger equation. For that reason, the solving of the KS equation consists of the basic principle of the DFT tools. Nevertheless, the exact form of the exchange-correlation energy: $E_x$ term is still unknown , which represents the major problem. At this stage, finding an approximate form related to $E_{xc}$functional with a sufficient accuracy is a huge challenge of the modern DFT to achieve outcomes in a good agreement with the experimental data.

To elucidate this issue, the density will be precisely known and the energy will be near to the right one. Hence, it is necessary to get an expression for the $E_{xc}$ functional which approximates to the correct expression. The KS equations must be solved by an iterative method that aims to diagonalize the Hamiltonian system that can be summarized as the following, figure 2.1:

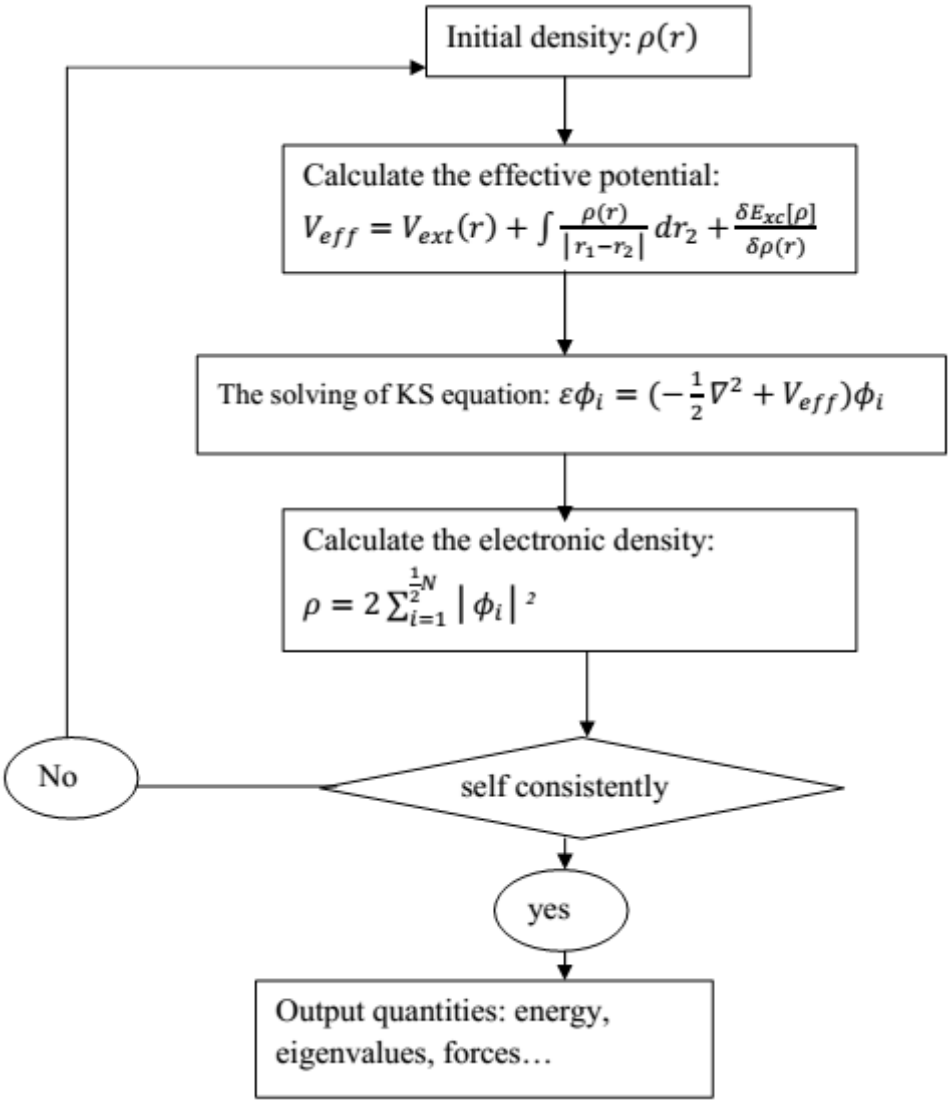


***Figure 2.1:*** *Schematic representation of the self-consistent loop for solution of Kohn-Sham*

Besides that, many codes and packages involved for calculations. See table 2.1.

| Method | Code Name | URL and distribution |
|---|---|---|
| **PSEUDOPOTENTIALS**<br>plane waves | **ABINIT** | www.abinit.org<br>Public License GNU |
| | **CASTEP**<br>Cambridge Serial<br>Total Energy Package | www.castep.org<br>Commercial License |
| | **CPMD**<br>Car-Parrinello<br>Molecular Dynamics | www.cpmd.org<br>Free license after registration |
| | **PARATEC**<br>PARAllel Total<br>Energy Code | www.nersc.gov/projects/paratec<br>through collaborations<br>or by contacting<br>DBRaczkowski@lbl.gov |
| | **PWscf**<br>Plane-Wave<br>Self-consistent field | www.pwscf.org/home.htm<br>GNU public license |
| | **VASP**<br>Vienna Ab-initio<br>Package Simulation | cms.mpi.univie.ac.at/vasp<br>commerciale licence |
| **FP-LAPW**<br>Augmented plane wave | **Win2k** | www.wien2k.at<br>commerciale licence |
| | **SIESTA** | www.uam.es/departamentos/ciencias/ |

| | | |
|---|---|---|
| **LCAO**<br><br>localized orbitals<br><br>Gaussian<br><br>Slater-like | Spanish Initiative for Electronic Simulation of Thousands of Atoms | fismateriac/siesta<br><br>Free license after registration |
| | **CRYSTAL** | www.crystal.unito.it<br><br>commerciale licence |
| | **ADF-BAND**<br><br>Amsterdam Density<br><br>Fuctional package | www.scm.com<br><br>commerciale licence |
| **KKR**<br><br>multiple scattering | **MACHEKANYAMA 2002,**<br><br>**Very useful to study disordered systems**<br><br>By Akai Hisazumi | kkr.phys.sci.osaka-u.ac.jp<br><br>public licence |

***Table 2.1:*** *Codes and methods of calculating the electronic structure.*

It is important to have an accurate [$\rho(r)$] functional or $E_{xc}(r)$ potential to give a satisfactory description of a realistic condensed system. Moreover, many methods considered to study the potential in a self-consistent manner because the density, solution of these equations, should be equal to that initially introduced to solve these self-coherent equations.

Within the following paragraphs, we will present briefly the different $E_{xc}[\rho]$ approach.

### 2 - 6 - 1 Local density approximation

Local density approximation (LDA) is the most widely used in applied DFT. This approximation is based on the HEG that has the same electron density at the point. It varies slowly as a function of $r$ coordinate and multiple values for the energy-exchange can consequently be used; where, the energy of exchange formulated by Dirac is:

$$E_x^{LDA}[\rho] = -C_x \int \rho^{\frac{3}{4}}(r)dr, \text{ given that } C_x = -\frac{3}{2}\left(\frac{3}{8\pi}\right)^{\frac{1}{3}} \qquad \textbf{(2.19)}$$

LDA is more accurate for systems having slowly varying densities [93], as the assumed density is locally a constant. Although, it is a simple approximation, the results of this approximation are surprisingly good.

### 2 - 6 - 2 Generalized gradient approximation and modified Becke-Johnson potential

This approximation comprises in introducing the gradient of density in the description of exchange and correlation effects. For the exchange-correlation energy functional, GGA improves generally the local density description of solids, atoms and molecules. While the LDA is local by consideration of a density equivalent to that of a HEG, is incorporated here to non-local elements. Indeed, the density gradient can take into account the variation of the density in the neighbors of each point. For its formula we can write:

$$E_{xc}^{GGA}[\rho,\nabla\rho]=\int f(\rho,\nabla\rho)\,)dr \qquad \textbf{(2.20)}$$

GGA seems to provide reliable results for all main types of chemical bonds binding energies than LDA. At this point, several studies have been performed to evaluate the advantages or disadvantages of GGA compared to LDA approximations [96-98].

In addition, there are various forms of functional that are used in many different calculations, given that it is feasible to use parameters that are fitted to experimental data as the Becke exchange [99], other form has been employed in a part of our study, which is the modified Becke Johnson potential (mBJ) which proposed by Tran and Blaha [100].

The mBJ exchange potential was developed from a semi-local exchange potential [101]

As propped by Tran and Blaha[100], The modified Becke Johnson potential is:

$$v_X^{mBJ}(r) = cv_X^{BR}(r) + (3c-2)\frac{1}{\pi}\sqrt{\frac{5}{12}}\sqrt{\frac{2t(r)}{\rho(r)}} \qquad \textbf{(2.21)}$$

Given that *c* was chosen to depends linearly on the square root of the average of $|\nabla\rho|/\rho$,

where $c = \alpha + \beta(\frac{1}{V_{cell}}\int_{cell}\frac{|\nabla\rho(r\prime)|}{\rho(r\prime)}d^3r')^{\frac{1}{2}}$ **(2.22)**

with ($\alpha$ = -0.012, $\beta$ = 1.023 bohr$^{1/2}$ and $V_{cell}$ presents the unit cell volume).

For the kinetic energy density, the formula is:

$$t = \frac{1}{2}\sum_{i=1}^{N}\nabla\psi_i^*\nabla\psi_i \qquad \textbf{(2.23)}$$

And $\rho$ is the electronic density:$\rho = \sum_{i=1}^{N} |\psi_i|^2$. The Becke and Roussel (BR) potential [102] is:

$$v_X^{BR}(r) = -\frac{1}{b(r)}(1 - e^{-x(r)} - \frac{1}{2}X(r)e^{-X(r)}) \qquad \textbf{(2.24)}$$

This latter is proposed to model the Coulomb potential created by the exchange hole, where *b* is obtained by:

$$b = (X^3 e^{-X}/(8\pi\rho))^{1/3} \qquad \textbf{(2.25)}$$

when *X* is determined from a formula involving $\nabla^2\rho$, $\nabla\rho$, $\rho$ and *t*.

## 2 - 7 - Korringa, Kohn , Rostoker method

In Korringa-Kohn-Rostocker (KKR) method, we use multiple scattering formalism for the calculation of the electronic structure of the materials. It was introduced in 1947 by Korringa [103] and in 1954 by Kohn and Rostoker [104]. This method is based on the use of multiple scattering theories reformulated by the procedure of Green's functions for solving the Schrödinger equation and the determination of the electronic band structure. Then, the diffusion properties of each atom are described by matrix diffusion. Where the multiple scattering by all the atoms in the system will determined by requesting that the incident wave at each center is the total of the outgoing waves from all other centers.

### 2 - 7 - 1 Green's function method

For the atomic units, we are going to use (ħ =1 and $m_e$ = 1), where the solution of KS equation related to energy E, with a source at the position *r'*, is:

$$(\nabla^2 + V(r) - E)G(r, r'; E) = -\delta(r - r') \qquad \textbf{(2.26)}$$

The spectral representation associated to Green function is given by:

$$G(r, r'; E + i\varepsilon) = \sum_{\sigma} \frac{\psi_\sigma(r)\psi_\sigma^*(r')}{E + i\varepsilon - E_\alpha} \qquad \textbf{(2.27)}$$

Also, the charge density can be expressed as the following:

$$\rho(r) = 2\sum_{\alpha, E_\alpha < E} |\psi_\alpha(r)|^2 = -\frac{\pi}{2}\int^{E_f} dE ImG(r, r'; E) \qquad \textbf{(2.28)}$$

At *r* position, the equation **(2.28)** can be treated as local density of states, subsequently, within the imaginary part of the Green function; this local density of states on particular atom is obtained. Here, the index *i* is substituted by $\alpha$ to avoid the confusion in terms of the imaginary numbers. The local density of states on particular atom within volume $\upsilon$ is obtained by integrating the imaginary part of the Greens function over $\upsilon$.

$$\rho_{\upsilon}(r) = -\frac{\pi}{2}\int_{\upsilon} drImG(r,r';E) \qquad \textbf{(2.29)}$$

Within the analytical properties of the Green function: G(z), where z = E + iε is a complex variable of energy, the energy integral can be transformed into contour integral in the complex energy plane

$$\rho(r) = -\frac{\pi}{2} Im \int_{E_B}^{E_f} dzG(r,r';z) \qquad \textbf{(2.30)}$$

In **(2.30)**, the energy bounds of the contour are from the Fermi energy $E_F$ to that of the bottom of the valence band $E_B$.

Then, we can write the Green function connected to the Hamiltonian. Where, H is the Hamiltonian of the non-interacting system

$$G(E) = \frac{1}{E + i\varepsilon - H_0 - V} \qquad \textbf{(2.31)}$$

And $$H = E_0 - V \qquad \textbf{(2.32)}$$

For non-interacting system, The Green function is:

$$G_0 = \frac{1}{E + i\varepsilon - H_0} \qquad \textbf{(2.33)}$$

For an impurity in a crystal one starts with the bulk Green function G, such that V represents the change of impurity potential with respect to the bulk potential together with the potentials of the neighboring host atoms as perturbations.

Given that the Green's function method for the electronic structure calculations is due to KKR [103-104].

For the impurities, the Schrödinger equation is solved by the multiple scattering theories, which describes the propagation of wave in the solid as a repetition of single scattering events from different atoms.

Here, the Green function $G(r+R^n, r'+R^{n'}; E)$ can be expanded in each cell as a function of r and r' in terms of spherical harmonics, where

$$G(r+R^n, r'+R^{n'}; E)= \sum_{LL'} R_L^n(r;E)G_{LL'}^{nn'}(r;E)R_{L'}^{n'}(r;E)=\delta_{nn'}\sqrt{E}\sum_L H_L^n(r_>;E)R_L^n(r_<;E) \quad \textbf{(2.34)}$$

The whole space is divided into non overlapping and space filling spheres with center at position $R^n$. In each cell, the electrons are scattered by potentials $V^n$. For simplicity, we assume the potentials $V^n$ to be spherically symmetrical and centered at $R^n$. Given that $R_L^n(r;E)$ and $H_L^n(r;E)$ are the products of spherical harmonics and the radial eigenfunctions of the central potential $V^n(r)$. And (r and r') are restricted to the cells (n and n') and ($r_>$ and $r_<$) indicate the two vectors r and r' with smaller and larger absolute value

$$R_L^n(r;E) = R_l^n(r;E)Y_L(r) \text{ and } H_L^n(r;E) = H_l^n(r;E)Y_L(r) \quad \textbf{(2.35)}$$

Here, $H_L^n$ denoted the corresponding irregular solution varying $\frac{1}{r^{l+1}}$ at the origin which is identical with the spherical Hankel function $h_l(\sqrt{E}\,r)$ outside the range of the potential. And $R_L^n(r;E)$ represents the solution which varies at the origin $r^l$ which represents the solution for an incoming spherical Bessel function $j_j(\sqrt{E_r})Y_L(r)$. Here, the radial functions are connected by the Wronskian expression, which guarantees that the first term in expression **(2.34)** denotes the exact Green function for the signal potential $V_n(r)$ in free space, since, this term contain the source condition $-\delta(r-r')$ **(2.26)**. Where the second term is source free and thus have the regular solutions ($R_L^n$ and $R_{L'}^{n'}$) with double angular momentum expansion. The Green's function is described by the equation **(2.34)**, which satisfies that of the Schrödinger's equation in each cell n.

The $G_{LL'}^{nn'}(E)$ is the structural Green's function, which describes the connection of the solutions between different cells. Thus, the structural Green's function contains all the information about the multiple scattering problems. So, is worthy to mention that the main advantage of the KKR approach is in separating between the single site properties, which are described by that $R_L^n(r;E)$ and $H_L^n(r;E)$ , which are the radial solutions and the multiple scattering properties $G_{LL'}^{nn'}(E)$.

The structural Green function matrix can be extracted by matching the solutions of the neighboring cells at the cell boundary. In the multiple-scattering theory it is calculated from the Green's function of the inner region of the cell.

### 2 - 7 - 2 Coherent potential approximation (KKR-CPA)

The coherent potential approximation (CPA) is an extension to random materials of the muffin-tin approximation and used to calculate electronic band structure in solids. A variation implementation of the muffin-tin method to crystalline solids using Green's functions was suggested by Korringa and by Kohn and Rostocker, notice as the KKR method [105-106].

Within random materials, the theory is also applied by the introduction of an ordered lattice of effective potentials to replace the varying potentials in the randodm material. This approach is called the KKR coherent potential approximation (KKR-CPA) [107-108].

## 2 - 8 - Full-potential linearized augmented plan wave and augmented plane wave + local orbitals basis functions.

The solution of many electron problems has been changed to an eigenvalue problem of single particle KS equation **(2.13)**. Besides that, a lot of methods have been proposed to solve the following equation **(2.36)** for different applications, geometries, symmetries, chemical elements and materials requiring different approximations [109]

$$(-\frac{1}{2}\nabla^2 + V_{ext}(r) + \int \frac{\rho(r)}{|r_1 - r_2|} dr_2 + V_{xc}(r))\phi_i = \varepsilon\phi_i \qquad \textbf{(2.36)}$$

Within the equation **(2.36)**, the eigenvalue problem is directly related to choosing basis function sets $\phi_G(k,r)$ for all reciprocal lattice vectors up G to the largest value of $K_{max}$.

With the following equation **(2.37)**, the partial differential of that **(2.36)** can be solved to recognaize the value of that $C_{k,v}^G$.

$$\varphi_{k,v}(r) = \sum_{|k+G| \le K_{max}} C_{k,v}^G \, \phi_G(k,r) \qquad \textbf{(2.37)}$$

Where $C_{k,v}^G$ are the variational coefficients with the reciprocal lattice vector k for the υth sphere [109].

In fact, A lot of methods have been presented to solve the equation **(2.36)** for different applications, chemical elements, symmetries, geometries and materials requiring different approximations [109].

The Bloch theorem gives the most straightforward suggestion for three dimensional periodic solids, which would be to expand the wave function

to plane wave or Fourier series.

$$\phi_G(k,r) = e^{i(k+G)r} \qquad \textbf{(2.38)}$$

The augmented plane wave (APW) method was developed by Slater, in which the space is partitioned into spheres centered at each atom site, which is varying but nearly spherical. The so called muffin tin (MT) sphere and into the remaining interstitial region is illustrated in figure 2.2.

Slater [110], Andersen [111] and Koelling [112] presented a linearization method in the radial functions inside the MT sphere, the basis functions inside the spheres are linear combinations of that $u_l(r)Y_{l,m}(\theta,\phi)$ and its radial derivative $u'_l(r)Y_{l,m}(\theta,\phi)$.

with $\phi_G(k,r) = \frac{1}{\Omega} e^{i(k+G)r}$ r ϵ Interstitial

$$\phi_G(k,r) = \sum_{l,m}\{A^v_{l,m}u_l(r) + B^v_{l,m}u'_l(r)\}Y_{l,m}(\theta,\phi) \text{ r } \epsilon \text{ MT} \qquad \textbf{(2.39)}$$

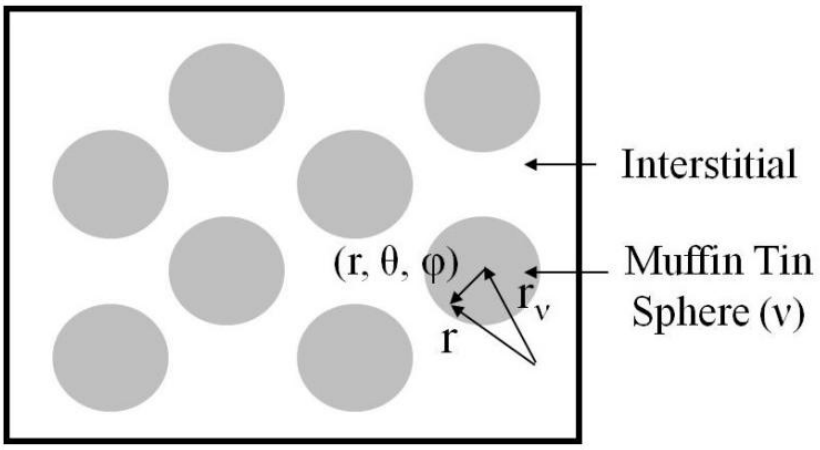


***Figure 2.2**: Space division both in the APW and LAPW methods.*

Sjösted, Nordström and Singh [113] proposed an alternative way to linearize the APW method in which the continuous derivative condition is released. Within that method, the eigenvalue problem of the original APW method is linearized by choosing fixed linearization energies for the augmented plane wave basis functions in equation **(2.13)**. Subsequently, the flexibility of the basis set with respect to the reference energy is obtained by adding a set of local orbitals noticed ($l_O$).

Given that, $\phi^{lo}_{APW}(r) = 0$ r ϵ Interstital

$$\phi^{lo}_{APW}(r) = \sum_{l,m}\{A_{l,m}u_l(r^\alpha,\epsilon_l) + B_{l,m}u'_l(r^\alpha,\epsilon_l)\}Y_{l,m}(r^\alpha) \text{ r } \epsilon \text{ MT} \qquad \textbf{(2.40)}$$

The coefficients are obtained by requiring the function to be zero at the sphere boundary and normalized where we using the same linearization energies.
The APW basis functions keep the convergence behavior of the original APW, while the local orbitals ($l_O$) make it flexible with respect to choice of the reference energy.

## 2 - 9 - Wien2K package

A part of our calculations were carried out using the density functional theory within the help of the full potential linearized augmented plan wave (FP-LAPW) method implemented in Wien2K code [114].

This method has emerged as a widely used very robust and precise state of ab initio electronic structure technique with reasonable computational efficiency to simulate the electronic properties of materials on the basis of DFT [109].

# Part 3: Ab intio studies of magnetic and electronic properties of $SnO_2$, $ZrO_2$ and $FeS_2$ used in spintronic applications

## 3 - 1 - Magnetic and electronic properties of Cr and Mn doped $SnO_2$: ab-initio calculations

### 3 - 1 - 1 Introduction

Diluted magnetic semiconductors (DMS) are compounds based on typical semiconductors (ZnO, $TiO_2$, $SnO_2$...). Recently, Tin dioxide ($SnO_2$) attracted much attention, and this is due to its potential application in spintronic devices [115].

In fact, $SnO_2$ has diverse optical and electrical properties [46], these properties are suitable in many fields as in thin solid films and photovoltaic devices. It should be noted that $SnO_2$ is n-type semiconductor [47], Including a direct wide band gap with $E_g$=3.6 eV[48]. For this reason many efforts have been devoted to study the magnetic properties of $SnO_2$ doped and co-doped with various transition metals (Co, Cr, Fe, W, F, Rh…), experimentally [48-51] and theoretically [52-57]

Punnoose et al. [116], show that chemically synthesized $Sn_{1-x}Co_xO_2$ nanoscale powders with $x \leq 0.01$ are ferromagnetic at room temperature when prepared by precipitation and annealing in the narrow temperature window of 350 – 600 °C. Relating to thin films and Fe-doped $SnO_2$ films, Torres et al. [117] noticed that transparent pure and Fe-doped $SnO_2$ thin films were grown by pulsed laser deposition technique (PLD) on $LaAlO_3$ substrates; X-ray diffraction shows that the films are polycrystalline and have the rutile structure. Surprisingly, the pure film presents magnetic-like behavior at room temperature with a saturated magnetization of almost one-third of the doped film (~3.6 and 11.3 emu per g, respectively) and its magnetization could not be attributed to any impurity phase. Beside this fact, Fitzgerald et al. [118], indicates that the room temperature ferromagnetism is observed in $Sn_{1-x}M_xO_2$ with (M = Mn, Fe) polycrystalline samples with magnetic moments of 0.11 and $0.95\mu_B$ per Mn and Fe ion, respectively; Curie temperature is 360 K for 5% Fe doped $SnO_2$ sample, the ferromagnetism cannot be associated to the minor impurity phase. Hong [119],studied TM-doped $SnO_2$ films, he observed that magnetic moments could be very large, with the maximum saturation of $6\mu_B$ per impurity atom for Cr-doped $SnO_2$ thin films, but it could be influenced very much by the nature of substrate type. On the other hand, results on TM-doped ZnO films interestingly have revealed that in these systems, the magnetism more likely resulted from defects and/or oxygen vacancies.

Concerning the numerical simulations, Bouamra et al. [54], show, using the DFT within the (CRYSTAL03 code), that in Rh-doped $SnO_2$(110); $Sn_{48-2x}Rh_{2x}O_{96}$ (x = 2, 3, 4, 5) with (4×2×1) supercells, system, the Rh impurities substituted with Sn ions acquire magnetization with important value of magnetic moment due to the Rh[4d] states hybridized with O[2p] states in the vicinity of the Fermi level. For Co-doped (110) $SnO_2$ thin film [55], the full-potential linearized augmented plane-wave (FLAPW) method implemented in the (WIEN2k) simulation package, when WIEN2K is the name of a numerical simulation code in which the full-potential linearized augmented plane-wave (FLAPW) method is implemented, indicate that a clustering of Co atoms around O takes place at higher Co concentrations, and the magnetic coupling between Co ions is FM. The strong hybridization between Co [3d] and O[2p] is found to be responsible for the FM coupling. In addition, different geometries with FM, antiferromagnetic and nonmagnetic configurations are also found in Co-doped $SnO_2$ surface layers of the thin film. Also, the DFT was implemented in Wang et al. [120] to study (V, Mn, Fe, and Co)-doped $SnO_2$ in the well-tested SIESTA code; so they,show that ferromagnetism is obtained by doping $SnO_2$ with Feand Co ions and paramagnetism is the ground state in V- and Mn-doped $SnO_2$; oxygen vacancy has a strong influence on the magnetic properties of these TM ion-doped compounds.

In this work, we used the calculations based on (KKR-CPA) method employing the (GGA and LDA) approximations [121] implemented in the Akai-KKR code [122] to study the effect of Mn-, Cr- and co- doped $SnO_2$, on the electronic and magnetic structure. Firstly, we discuss the stability of magnetic states in ($Sn_{1-x}TM_xO_2$;x=0.07, 0.09, 0.12 and 0.15 with TM=Mn or Cr) and ($Sn_{0.98-x}Mn_{0.02}Cr_xO_2$ withx=0.05, 0.09 and 0.13) doped and co-doped system within GGA and LDA approximations. The purpose of this study is the stability of ferromagnetic, ferrimagnetic or disorder local moment states, for $SnO_2$ doped and co-doped with two transition metals (TM), the Chromium and Manganese. The new finding is the stabilization of the ferrimagnetic phase in the co-doped $SnO_2$ depending on the Cr concentration.

Some values of Curie temperature ($T_c$) are estimated from the total energy difference between the DLM and FM states according to the Heisenberg model. Secondly, we calculate transition temperatures of doped and co-doped SnO2 systems.

This paper is organized as follow: Crystal structure and calculation method will briefly be described in the next section (II), the results and discussion are presented in section (III), followed by a conclusion in section (IV).

### 3 - 1 - 2 Crystal structure and calculation method

The present calculations based on the density functional theory (DFT), using the Korringa Kohn Rostoker (KKR) method [123-124], which enable us to take into consideration the randomness of the impurity elements during the calculation. Here, we are going to use the AKAI KKR (MACHIKANEYAMA 2002V08) developed by H. Akai [122], which uses the (DFT) combined with the coherent potential approximation (CPA), including the (KKR-CPA-GGA) and (KKR-CPA-LDA). On the one hand, several different parameters of the General Gradient Approximation (GGA) have been proposed and examined on a variety of materials. The GGA significantly improve the properties of the ground state of atoms, molecules and solids lightweight, and generally tend to produce larger network balance parameters regarding the (LDA); the GGA we used is Perdew–Wang functional, noticed (GGA91) [125], which is one of the most widely used functional in calculations involving solids; important publications in diluted magnetic semiconductors using the same approach have been added; namely [57, 120] using GGA of (Perdew–Burke–Eruzerhof (PBE)), [126] using LDA-VWN method and [122, 125] using GGA (Perdew–Wang functional).

On the other hand, Local Density Approximation (LDA) is based on the parameterization given by Moruzzi, Janak and Williams (MJW) [127]. Here, we should to say that The most widely used approximation, in density functional theory, is the local density approximation (LDA), where the functional depends only on the density at the coordinate where the functional is evaluated. While, Generalized Gradient Approximations (GGA) are still local but also take into account the gradient of the density at the same coordinate. Very good results have been obtained for molecular geometries and ground-state energies, using the GGA. The advantage of GGA with respect to LDA for $SnO_2$ has been added. We restricted the comparison between these approximations to phase stability, in order to show the advantage of GGA with respect to LDA for doped and co-doped $SnO_2$.

In this work, the rutile structure of $SnO_2$ has been considered. This latter crystalline structure has a tetragonal unit cell with two lattice parameters. The first is (a=4.7373 Å) and the second one is (c=3.1864 Å) with (u=0.307 Å) according to [128]. To improve the quality of our calculations, initially empty-spheres (ES) with (Z=0) as an inter-sites, are added. For each atom, the sphere radius is taken such that the volume of the unit cell is the sum of the volumes of all atomic spheres. The method used in this work is KKR combined with Coherent

potential approximation (CPA), in this case different doping concentration may be obtained within one unit cell.

Our $SnO_2$ system is $P4_2/mnm$ as a space group, with six atoms; two tin (Sn) atoms occupying the 2a Wyckoff positions (0,0,0); (½, ½,½) and four oxygen (O) occupying the 4f positions (u,u,0); (-u,-u,0); (½+u,½-u,½); (½-u,½+u,½), with eight (ES) sites localized at the followings positions (½,0,-0.1682); (0,½,-0.1682); (0,½,0.1682); (½,0,0.1682); (-0.3125,0.3125,0); (-0.1875,-0.1875,0.3363); (0.1875,0.1875,0.3363); (0.3125,-0.3125,0) as indicated in the figure 3.1. The valence states considered are: Sn($4d^{10}5s^25p^2$), O($1s^22s^22p^4$), Mn($3d^54s^2$) and Cr($3d^54s^1$).

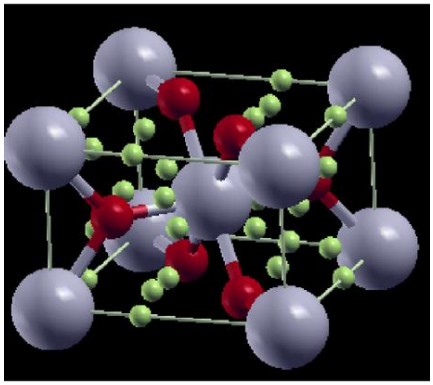

***Figure 3.1****: The unit cell of rutile SnO2; the big gray balls correspond to tin atoms, the small red balls to the oxygen atoms and the green balls to empty spheres.*

### 3 - 1 - 3 Results and discussion

Based on the previously indicated methods, the electron structure of rutile $SnO_2$ has been determined. The total energy obtained within GGA is lower than that within LDA; -25314.1919072 versus -25284.7996419 Ry, respectively. Secondly, the total density of States (DOS) and the partials O(2p) and Sn(4d), obtained within GGA and LDA, related to the pure $SnO_2$ as presented in figure 3.2 (a, b), reveal that the valence band (VB) included two parts; the first one is noted a high (VB), which has an energy range from (-0.54 to -0.17) Ry, the second one, which is called short (VB), is from (-0.7 to -0.54) Ry.

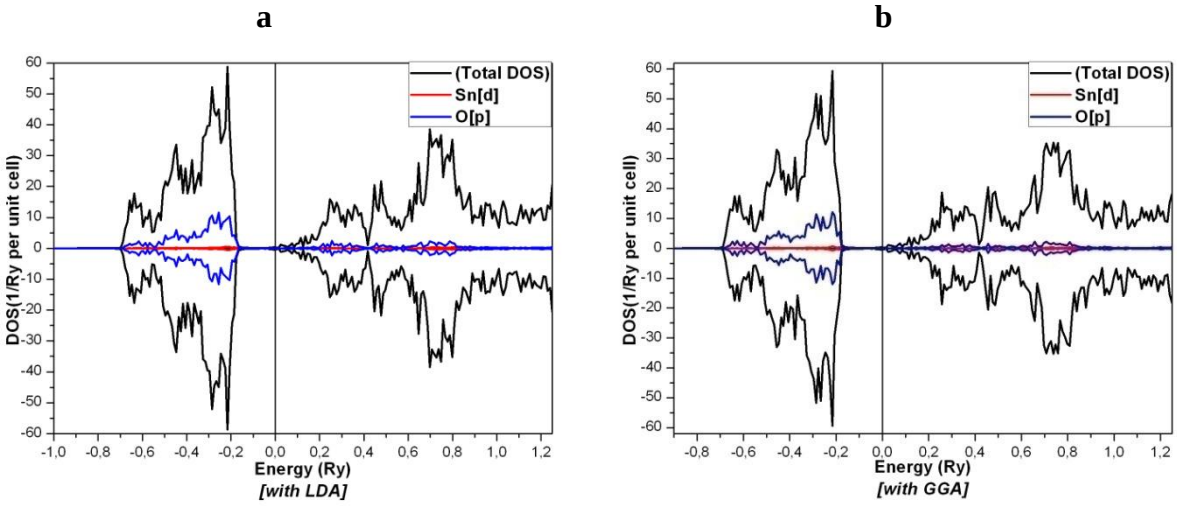


***Figure 3.2 (a, b):*** *Total and Partial DOS (TDOS and PDOS) of the pure $SnO_2$ related to the Fermi energy; the black, Red and blue, respectively are the TDOS, Sn[d] and O[p] shells*

For the $SnO_2$ without doped elements, the DOS of minorities and majorities spin are symmetrical because the $SnO_2$ is not magnetic and the sum of moment spin is null. On the other hand, the experimentally value of band gap is 3.6 eV [48], while in our calculation it is 2.0481 eV with the GGA and LDA, figure 3.2 (a, b). The application of LDA and GGA approximations to solids can lead, for example for semiconductors and insulators, to band gap which are not in full agreement with experimental results, this is due to the use of a potential which is the same for all orbitals. The band gap calculated from the eigenvalue spectrum differs from the true band gap by the derivative discontinuity of the exchange-correlation potential [129-130].

### *3 - 1 - 3 - 1 magnetic properties in Mn- and Cr- doped $SnO_2$*

In this part, the magnetic properties have been estimated for the doped and co-doped $SnO_2$ system with the transition elements (Mn and Cr) which are examined and compared for both approximations, GGA and LDA, and for different concentrations. The electronic structures, total energies, and magnetic moments of various $SnO_2$-based DMS with or without (TM elements) are calculated.

Concerning the Mn- doped $SnO_2$, the stabilization of the magnetic states is evaluated through the estimation of the total energy difference $\Delta E$, between the disordered local moment state and ferromagnetic state:

$$\Delta E = E_{DLM} - E_{ferro}\ [126] \qquad \textbf{(3.1)}$$

where $E_{DLM}$ and $E_{ferro}$ stand for the total energies of the DLM state and the ferromagnetic state, respectively. The DLM states are simulated by states in which half of the impurity ion spins point to the up direction and the rest points to the opposite direction; for example, ($Sn_{1-x}Mn^{\uparrow}_{0.5x}Mn^{\downarrow}_{0.5x}O_2$) stands for the DLM state, and ($Sn_{1-x}Mn^{\uparrow}_{x}O_2$) for the ferromagnetic state in which all spins have the same direction. Throughout the calculations: the potential form is restricted to the muffin-tin type. The wave functions in each muffin-tin sphere are expanded with real harmonic up to (l=2), where (l) is the angular momentum at each site [126]; the relativistic effect is also taken into account by using scalar relativistic approximation. The results of calculations show that the difference of energy **(3.1)**)for the ($Sn_{1-x}Mn_xO_2$ with x=0.02 and 0.05 as an example) system indicates the stability of DLM state with the ($E_{DLM}$-$E_{ferro}$) < 0, see table 3.1 and table 3.2. For Mn-doped $SnO_2$ the DLM state is stable, because the minority-spin of Mn[d] band is unoccupied, figure 3.3 (a, b), thus the Mn impurity has $d^3$ electron configuration due to the substitution of $Sn^{4+}$ by $Mn^{4+}$, so there is no carrier to mediate the ferromagnetic state. Then, the calculated magnetic for $Sn_{1-x}Mn^{\uparrow}_{0.5x}Mn^{\downarrow}_{0.5x}O_2$ stands for the DLM state.

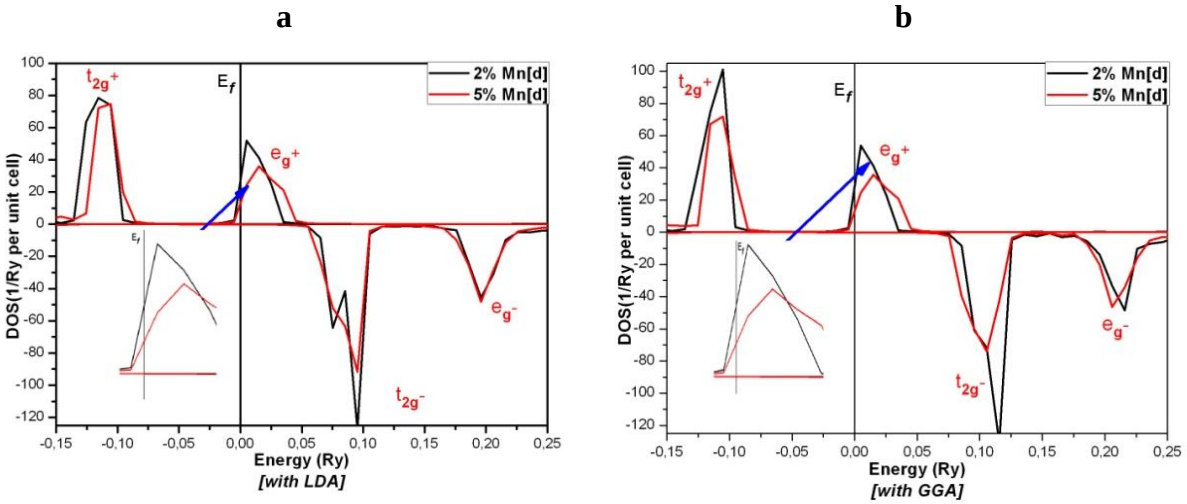


***Figure 3.3 (a, b):*** *PDOS of the Mn[d] shell in ($Sn_{1-x}Mn_xO_2$) related to the Fermi energy; (a) and (b), respectively with LDA and GGA*

| Mn | $E_{ferro}$(Ry) | $E_{DLM}$(Ry) | $E_{DLM}$-$E_{ferro}$ (Ry) | $M^T(\mu_B)$ | $M^{Sn}(\mu_B)$ | $M^{Mn}(\mu_B)$ | $M^O(\mu_B)$ |
|---|---|---|---|---|---|---|---|
| 2% | -24883.553638 | -24883.5536535 | -0.0000155 | 0.13499 | 0.00056 | 3.18302 | 0.00085 |
| 5% | -24281.6857814 | -24281.6859648 | -0.0001834 | 0.31940 | 0.00120 | 3.09093 | 0.00362 |

***Table 3.1:*** *Energy and moment facts in $Sn_{1-x}Mn_xO_2$ with LDA*

| Mn | $E_{ferro}$(Ry) | $E_{DLM}$(Ry) | $E_{DLM}$-$E_{ferro}$ (Ry) | $M^T$($\mu_B$) | $M^{Sn}$($\mu_B$) | $M^{Mn}$($\mu_B$) | $M^O$($\mu_B$) |
|---|---|---|---|---|---|---|---|
| 2% | -24912.6360851 | -24912.6360979 | -0.0000128 | 0.13637 | 0.00051 | 3.2502 | 0.00116 |
| 5% | -24310.3023355 | -24310.302516 | -0.0001806 | 0.32074 | 0.00111 | 3.14936 | 0.00461 |

***Table 3.2:*** *Energy and moment facts in $Sn_{1-x}Mn_xO_2$ with GGA*

The Mn magnetic moments are 3.18302 $\mu_B$ and 3.2502 $\mu_B$ related to LDA and GGA,respectively, for Mn concentration =2%, table 3.1 and table 3.2. Moreover, our calculation shows that the total magnetic moment increase, in both approximations, with increasing concentration, from 0.13637 to 0.32074 $\mu_B$ for the concentration from x=0.02 to x=0.05, respectively. According to the GGA, the major contribution to the moment come from Mn; ($||M^{Mn}||>>||M^{Sn}||+||M^O||$), table 3.1 and table 3.2, with $M^{Mn}$=3.2502 and 3.14936 $\mu_B$ for x=0.02 and x=0.05, respectively. The gap also decreases from the pure $SnO_2$ to $Sn_{0.85}Mn_{0.15}O_2$,which translates the VB to the Fermi level. Knowing that Mn ($3d^5 4s^2$) has seven electrons in $SnO_2$ which is doped in octahedral site of tin, it becomes $Mn^{4+}$ ($3d^3$). Also, the (d) orbital is divided into two states $t_{2g}$ ($d_{xy}$, $d_{yz}$, $d_{xz}$) and $e_g$ ($d_{x^2-y^2}$,$d_{z^2}$), respectively, low and high energy due to electronic field created by six ligand: octahedral crystal field. In this case: $Mn^{4+}$ ($3d^3$), will have three manganese electrons that will fill the $t^+_{2g}$ orbital, which is why the latter is to the left of the Fermi level in the VB, while the remaining three orbital ($e^+_g$, $t^-_{2g}$ and $e^-_g$) will be empty in the conduction band to the right of the Fermi level as noticed within Jahn teller effect in figure 3.8 (b).

For the magnetism in Cr- doped $SnO_2$, table 3.3 and table 3.4 indicated that the Cr magnetic moments are (1.9938 and 2.02115$\mu_B$)within LDA and GGA, respectively, when x=0.15. However, our results indicate that the state of Cr- doped SnO2is different from that of Mn-doped SnO2. In the case of ($Sn_{1-x}Cr_xO_2$), ($\Delta E= E_{DLM}- E_{ferro}$) is positive for chromium concentrations, as example, within LDA, we got ($\Delta E=6.545*10^{-4}$ and $9.282*10^{-4}$ Ry, when x=0.12 and 0.15, respectively); beside that, within GGA, ($\Delta E=6.635*10^{-4}$ and $9.452*10^{-4}$ Ry, when x=0.12 and 0.15, respectively). This indicates the stability of ferromagnetic state. The same mechanism has been observed in V-doped SiO2 in [126]. Moreover, the present calculation proves that the majority-spin related to ($t^+_{2g}$) of chromium impurity is located on the Fermi level, see figure 3.4 (a, b), which indicates the existing of the half-metallic state, hence, the Jahn teller effect shown in figure 3.8 (a) can be related to figure 3.4 (a), which confirm also the stability of ferromagnetic states. This fact pushes us to calculate the mean field Curie temperature ($T_c$) by using the mean field method (MFA), the Curie temperature

can be estimated from the total energy difference between the DLM and the ferromagnetic state. This can be obtained by the help of following equation:

$$T_C = \frac{2}{3K_\beta} * \frac{\Delta E}{C} \qquad (3.2)$$

With (C: doping concentration and k: Boltzmann constant), as a result, the $T_c$ is proportional to 1/C, here, within LDA, ($T_C$ =574.35 and 651.62 K, when x=0.12 and 0.15, respectively), and within GGA ($T_C$=582.24 and 663.55 K, when x=0.12 and 0.15, respectively).

| Cr | $E_{ferro}$(Ry) | $M^T(\mu_B)$ | $M^{Sn}(\mu_B)$ | $M^{Cr}(\mu_B)$ | $M^O(\mu_B)$ |
|---|---|---|---|---|---|
| 7% | -23850.3071205 | 0.3055 | 0.00183 | 2.04561 | 0.00446 |
| 9% | -23440.4534981 | 0.3858 | 0.00232 | 2.02315 | 0.00621 |
| 12% | -22825.6736268 | 0.5058 | 0.00307 | 2.00405 | 0.00899 |
| 15% | -22210.8944039 | 0.6255 | 0.00381 | 1.99380 | 0.01195 |

***Table 3.3:*** *Energy and moment facts in ($Sn_{1-x}Cr_xO_2$) with LDA*

| Cr | $E_{ferro}$(Ry) | $M^T(\mu_B)$ | $M^{Sn}(\mu_B)$ | $M^{Cr}(\mu_B)$ | $M^O(\mu_B)$ |
|---|---|---|---|---|---|
| 7% | -23878.5761762 | 0.3060 | 0.00172 | 2.07275 | 0.00538 |
| 9% | -23468.4008366 | 0.3864 | 0.00218 | 2.05059 | 0.00737 |
| 12% | -22853.1384126 | 0.5064 | 0.00288 | 2.03156 | 0.01050 |
| 15% | -22237.8766731 | 0.6262 | 0.00359 | 2.02115 | 0.01380 |

***Table 3.4:*** *Energy and moment facts in ($Sn_{1-x}Cr_xO_2$) with GGA*

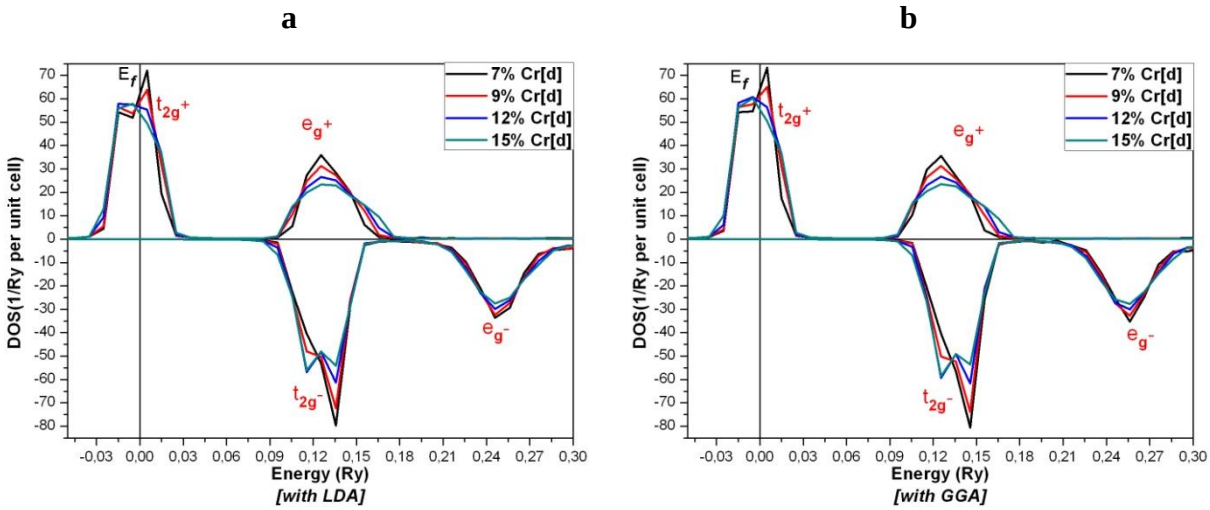


***Figure 3.4 (a, b):*** *PDOS of the Cr[d] shell in ($Sn_{1-x}Cr_xO_2$) related to the Fermi energy; (a) and (b), respectively with LDA and GGA*

***-Magnetic properties in Cr- doped $Sn_{0.98}Mn_{0.02}O_2$***

The aim of the present work is to study oxide-based semiconductor with double transition metal impurities (3d-3d) for ($Sn_{0.98-x}Mn_{0.02}Cr_xO_2$) system rather than the ordinary single impurity. In this study we restrict our study to LDA and GGA, the effective on-site Coulomb (U) and exchange (J) between electrons with the same orbital angular momentum have not been introduced.

In fact, the double impurities in the current host system can optimize the hybridization instead of the single one, so it is possible to obtain the ($sp^3d$) hybridization as noticed in the case of $Ti_{1-2x}Cr_xMn_xO_2$ with x = 0.0416 [131]; Thus, in this kind of ($sp^3d$), we have one (s), three (p) and one (d) orbitals of almost equal energy intermix to give five identical and degenerate hybrid orbitals.

The FM and DLM states were obtained for the Cr- and Mn- doped $SnO_2$, respectively, with both GGA and LDA when (x=0.12 and 0.15, respectively). Beside this fact, the double impurities by using the (LDA or GGA) and also the concentration has a direct influence on the $Sn_{0.98-x}Mn_{0.02}Cr_xO_2$**,(**x=0.05, 0.09 and 0.13) states from Ferromagnetic ($Sn_{0.98-x}Mn^{\uparrow}_{0.02}Cr^{\uparrow}_xO_2$ ) to Ferrimagnetic ($Sn_{0.98-x}Mn^{\downarrow}_{0.02}Cr^{\uparrow}_xO_2$) or to the opposite; to distinguish the impact of the concentration and the approximation (LDA or/and GGA), we are going to compare the influence of concentration within, firstly the LDA, secondly the GGA, and thirdly between LDA and GGA for the same concentration.

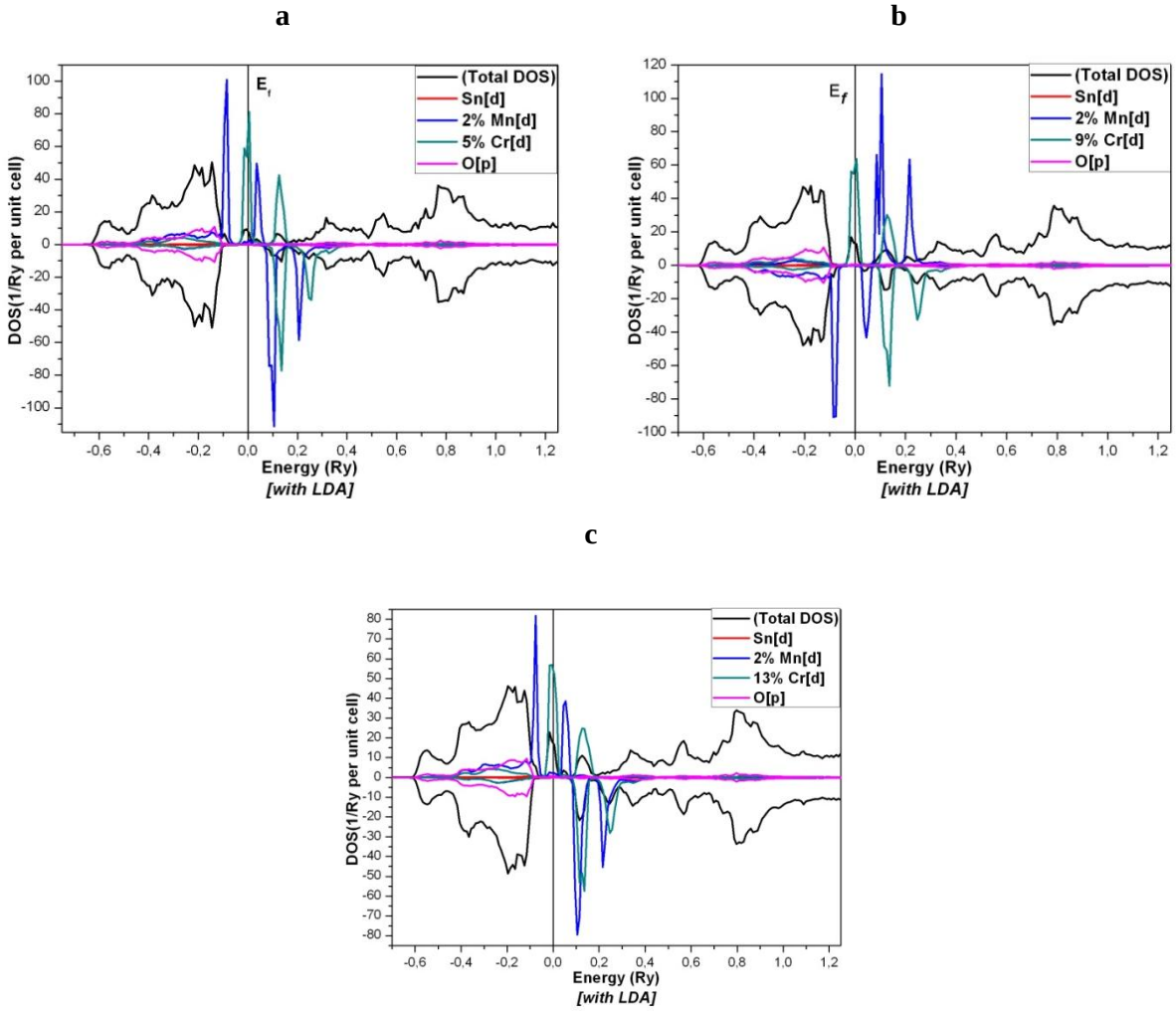


***Figure 3.5 (a, b, c):*** *TDOS and PDOS of the ($Sn_{0.98-x}Mn_{0.02}Cr_xO_2$)related to the Fermi energy; the black, Red, blue, green and pink respectively are the TDOS, Sn[d], (2% of Mn[d]), Cr[d] and O[p] shells with LDA*

Within LDA, the calculation shows the stability of ferromagnetic state for (x=0.05 and 0.13); we calculated the total and partial DOS: figure 3.5 (a, c), it is clear from the PDOS of (2% of Mn beside Cr-) co-doped $SnO_2$ rutile (figure 3.7 (c, e) related to figure 3.5 (a, c)), that the valence and conduction bands are predominantly contributed of O[2p] and Sn[3d], thus spin polarization around the Fermi level is mainly composed by Cr[3d] states and the nearest neighboring O[2p] states. From the calculated total DOS of ($Sn_{0.98-x}Mn_{0.02}Cr_xO_2$), a decrease of energy gap for the co-doped related to the pure $SnO_2$ is observed. This is because Cr ($3d^5 4s^1$) has six valence electrons and $Cr^{4+}$ ($3d^2$) in ($Sn_{0.98-x}Mn_{0.02}Cr_xO_2$), has two net electrons, so the variation in the gap is due to the Coulomb correlation interaction between ($Cr^{4+}$ and $O^{2-}$) cation and anion, respectively. Concerning the Jahn-Teller effect, a splitting

between $t_{2g}$ and $e_g$ is observed, thus the repulsion between the cation $Cr^{4+}$ ($t^2_{2g}$ $e^0_g$) and the anion $O^{2-}$ is weak, and then, the metal oxide distance is lower than in the case of spherical electronic density and the c parameter decreases. From the calculated total and partial DOS of $Sn_{0.98-x}Mn_{0.02}Cr_xO_2$, (see figure 3.7 (e) related to figure 3.9 (a)), the majority-spin DOS is metallic, while the minority-spin components display a conduction band. On the other hand, in the present calculations, the total magnetic moment of unit cell is of 0.3445 and 0.6653 $\mu_B$, respectively for x=0.05 and 0.13, see table 3.5, and the partial moments with x=0.05 are 3.00151;2.07483; 0.00494 $\mu_B$ for Mn, Cr and O, respectively. And are 3.00526; 1.99771; 0.01235 $\mu_B$, for x=0.13. These values show that the p-d exchange coupling between the moment of Cr (3d): 2.07483 with O (2p): 0.00494 $\mu_B$, for x=0.05, and Cr (3d): 1.9977 with O (2p): 0.01235$\mu_B$, for x=0.13}, is ferromagnetic. Therefore the DOS of ($Sn_{0.98-x}Mn_{0.02}Cr_xO_2$) shows that the host system, rutile $SnO_2$ , is a half-metal, (figure 3.5 (c) and figure 3.9 (a)) that is to say, the conduction electrons around the Fermi level are hundred percent spin polarized. The total moment calculations is also a typical character of half-metallic ferromagnetic due to hybridization between the Cr (3d) state and the nearest-neighboring O (2p) state. On the other hand, for the same concentration (x=5 and 13%), the 2% of Mn impurity band is located at the top of the valence band (TVB) and conduction band (TCB), respectively, for the $t^+_{2g}$ and $e^+_g$ and the bottom of conduction band (BCB) for $t^-_{2g}$ and $e^-_g$, as noticed in figure 3.5 (c) referredto figure 3.9 (a) of Jahn teller effect which confirm also the stability of ferromagnetic states.

| Cr | $E_{ferro}$(Ry) | $M^T(\mu_B)$ | $M^{Sn}(\mu_B)$ | $M^{Mn}(\mu_B)$ | $M^{Cr}(\mu_B)$ | $M^O(\mu_B)$ |
|---|---|---|---|---|---|---|
| 5% | -23858.9164693 | 0.3445 | 0.00174 | 3.00151 | 2.07483 | 0.00494 |
| 9% | -23039.2092089 | 0.2658 | 0.00192 | 2.95547 | 2.02079 | 0.00420 |
| 13% | -22219.5033215 | 0.6653 | 0.00371 | 3.00526 | 1.99771 | 0.01235 |

***Table 3.5:*** *Energy and moment facts in ($Sn_{0.98-x}Mn_{0.02}Cr_xO_2$) with LDA*

Though, when x=0.09, the stability of ($Sn_{0.89}Mn_{0.02}Cr_{0.09}O_2$) system has been changed, and this fact confirms the direct impact of changing the chromium percentage beside 2% of Mn, from figure 3.5 (b), the 2% of Mn impurity band is different than figure 3.5 (a, c), the majority-spin states Mn (3d) occurs to the bottom of valence band (BVB) and the top of conduction band, respectively for the $t^-_{2g}$ and $t^+_{2g}$, see figure 3.7 (c), the minority ones located at BCB and TCB related to $e^-_g$ and $e^+_g$, respectively, as well as on comparing the figure 3.9 (b) and figure 3.5 (b) besides figure 9 (a), we can say that the 9% of chromium stabilized the

ferrimagnetic state. To predict theCurie temperature $T_c$, here, we considered the previous steps as noticed before, to find out the ΔE through computing the energies of ($Sn_{0.89}Mn^{\uparrow}_{0.01}Mn^{\downarrow}_{0.01}$ $Cr^{\uparrow}_{0.045}Cr^{\downarrow}_{0.045}O_2$) versus ($Sn_{0.89}Mn^{\uparrow}_{0.02}Cr^{\uparrow}_{0.09}O_2$); as results, also the $T_C$ augmented by adding the (Cr) concentration beside (2% of Mn); as example: we obtained ($T_C$ =561.06 K in case of ferromagnetic) and ($T_C$ =429.93 K in case of ferrimagnetic) when (x=0.13 and 0.09), respectively. Hence the (Cr) concentration is a main factor to stabilize the (ferromagnetic or ferrimagnetic) state within LDA. At this stage, in an antiferromagnetic (DLM of 2%Mn) material, the magnetic moment directions of different sublattices are different, and the magnetization of the medium is zero in the absence of magnetic field, though, on ferrimagnetism, the medium has at least two magnetic sublattices when $Sn_{0.98-x}Mn_{0.02}Cr_xO_2$. The magnetic moments of at least two sublattices are anti-parallel. In contrast to antiferromagnetism, the magnetization of different sublattices don't completely cancel each other, hence, the ferrimagnetism has a spontaneous magnetization; consequently, (2% of Mn beside Cr) would explain that the magnetic transformation, such as from ferrimagnetic to ferromagnetic or the opposite token place when external magnetic field (H) is changed; such kind of transition induced by magneticfield.

Also, varying the chromium concentration in the host system of $Sn_{0.98-x}Mn_{0.02}Cr_xO_2$ has changed the states within the GGA from the ferromagnetic (figure 3.6 (b) related to figure 3.9 (a)), to ferrimagnetic (figure 3.6 (a) related to figure 3.9 (b)), when (x=0.13 and 0.05), respectively, the PDOS of the manganese impurity (figure 3.7 (d) related to figure 3.6 (a, b)), shows the majority-spin states of Mn (3d) occurs to the (BVB and TCB), respectively for the $t^{-}_{2g}$ and $t^{+}_{2g}$, see figure 3.7 (d), as well as (BCB and TCB) included the minority of ($e^{-}_{g}$ and $e^{+}_{g}$), concerning the chromium impurity, the conduction electrons around the Fermi level are hundred percent spin polarized as well as the total moment calculations is a typical character of half-metallic compounds (figure 3.7 (f)) due to hybridization between the Cr (3d) state and the nearest-neighboring O (2p) state. On the one hand, table 3.6 shows the augmenting of moment total from (0.1042 to 0.6661 $\mu_B$) when (x=0.05 and 0.13) respectively, hence the (Cr beside 2% of Mn) are the most important factor to lead the magnetism. On the other hand the (2% of Mn) reduce the ($T_c$), if we considered (x=0.15, case of Cr- doped) we get ($T_C$ =663.55 K), while (x=0.13 beside 2% of Mn, case of co- doped) we have only ($T_C$ =565.62 K), here, at least, the (2% of Mn) has two impact: the first, is to reduce the $T_c$ and/or change the states.

| Cr | $E_{ferro}$(Ry) | $M^T(\mu_B)$ | $M^{Sn}(\mu_B)$ | $M^{Mn}(\mu_B)$ | $M^{Cr}(\mu_B)$ | $M^O(\mu_B)$ |
|---|---|---|---|---|---|---|
| 5% | -23887.1962661 | 0.1042 | 0.00088 | 3.03520 | 2.10626 | 0.00101 |
| 13% | -22246.4962284 | 0.6661 | 0.00348 | 3.06845 | 2.02443 | 0.01437 |

***Table 3.6:*** *Energy and moment facts in ($Sn_{0.98-x}Mn_{0.02}Cr_xO_2$) with GGA*

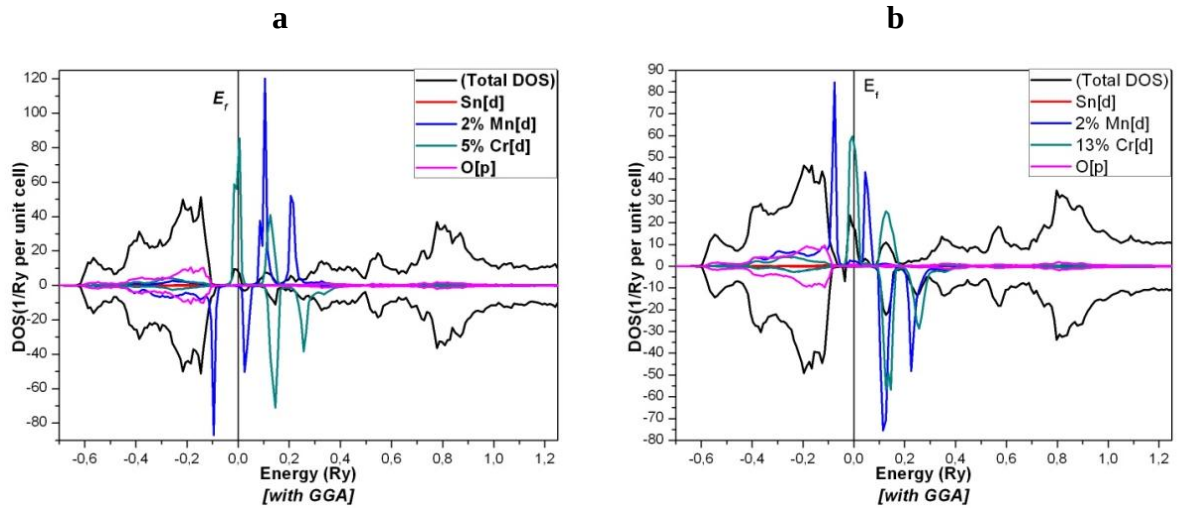


***Figure 3.6 (a, b):*** *TDOS and PDOS of the ($Sn_{0.98-x}Mn_{0.02}Cr_xO_2$)related to the Fermi energy; the black, Red, blue, green and pink respectively are the TDOS, Sn[d], (2% of Mn[d]), Cr[d] and O[p] shells with GGA*

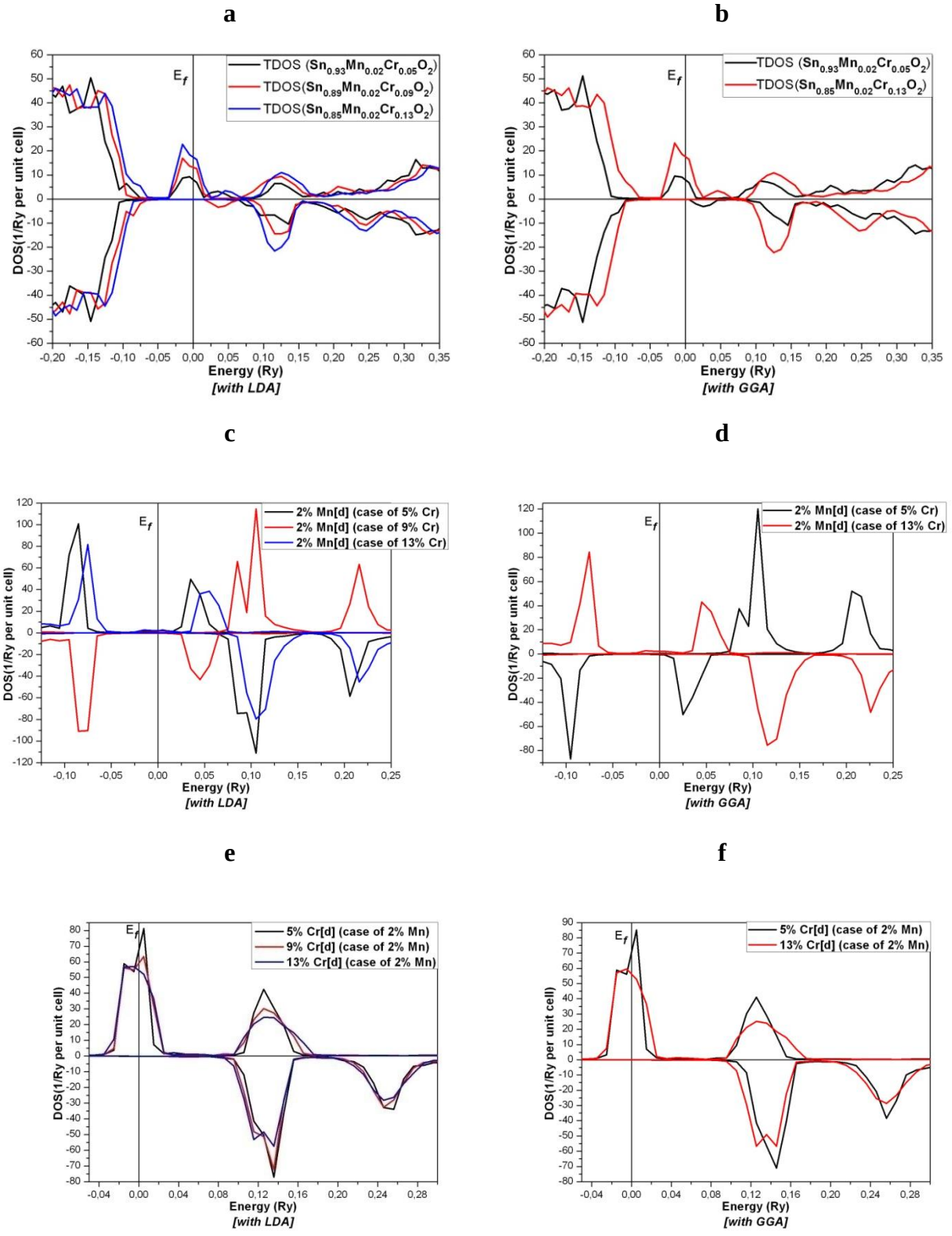


***Figure 3.7 (a, b, c, d, e, f):*** *Comparison included the different chromium concentration within the (LDA and GGA) in the ($Sn_{0.98-x}Mn_{0.02}Cr_xO_2$)related to the Fermi energy.*

On the other part, as a kind of comparison, we investigated that (2% of Mn) beside the used approximation makes sense in the present host system, as shown in figure 3.5 (a) versus figure 3.6 (a) when x=0.05, the first one has as total moment (0.3445 $\mu_B$) besides (0.1042 $\mu_B$) for the second (table 3.5 and table 3.6), which indicated the state is changing from the ferromagnetic to ferrimagnetic. However the figure 3.5 (c) besides figure 3.6 (b) within both approximations kept the ferromagnetic states when x=0.13, even if the GGA favorites a little bit the value of $T_c$ for the considered calculation, with GGA and LDA when x=0.13, we got (565.62 and 561.06 K), respectively. Experimental results [132] have shown that the Cr-doped $SnO_2$ is stable in the ferromagnetic State. The GGA is more in agreement with these results than LDA approximation, because ferromagnetic state is more stable within LDA approximation. Our results have been compared with existing experimental results. Indeed, Hong et al. [132] found that the transition temperature of $Sn_{0.95}Cr_{0.05}O_2$ is higher than 400K, in agreement with our results for Cr doped $SnO_2$.

### 3 - 1 - 4 Conclusion

To sum up this work, with the present concentration and approximations, the Mn- doped $SnO_2$ recognizes the DLM state, in contrast of Cr- doped which stabilized the ferromagnetic, it's worthy to say that Tc is proportional to the ratio ((energy difference)/C), the increase of chromium concentration stabilize the ferromagnetic phase, and then the energy difference between the ferromagnetic phase and the disorder local moment state increases more than the C increases. So, $T_c$ increases, knowing that the $T_c$ of GGA always higher than the LDA.

However with double impurity, when we use 2% of Mn, the stabilization states of the host system have been changed according to the used approximation and/or Cr concentration, the issue of ferromagnetic or ferrimagnetic could be changed within the same approximation when changing the Cr concentration, moreover, here, the GGA always makes the $T_c$ higher than LDA

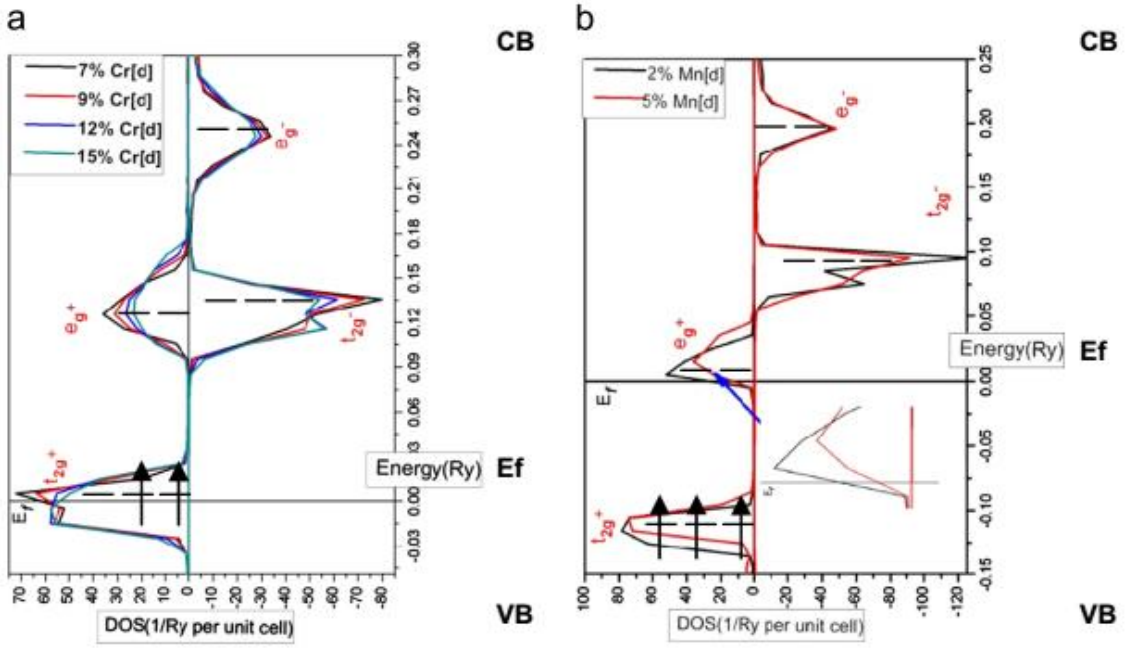


***Figure 3.8 (a,b ):*** *Jahn teller effect in Cr- and Mn- doped $SnO_2$.* ***(within LDA)***

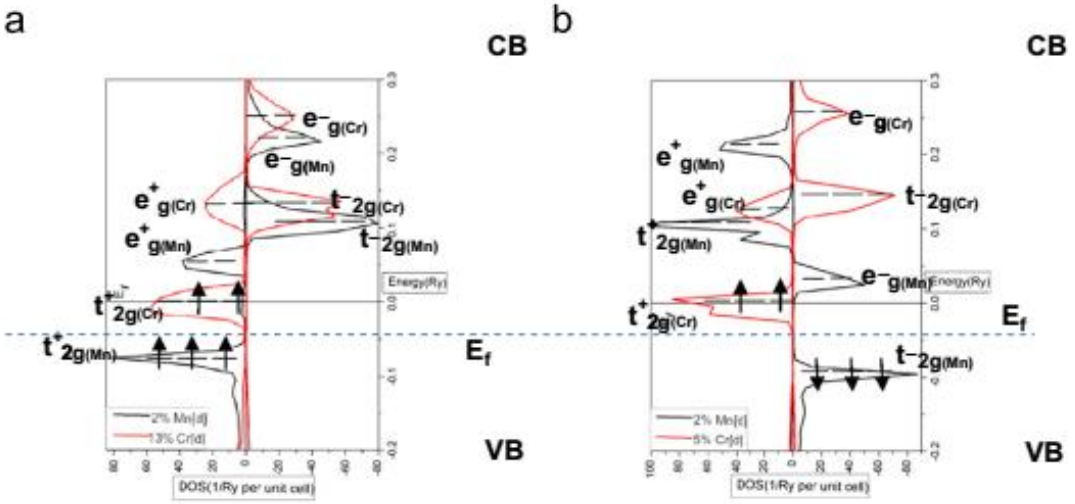


***Figure 3.9 (a, b):*** *Jahn teller effect in $Sn_{0.98-x}Mn_{0.02}Cr_xO_2$.* ***(a within LDA and b within GGA)***.

## 3 - 2 - First-principles study of magnetic and electronic properties of fluorine doped $Sn_{0.98}Mn_{0.02}O_2$ system.

### 3 - 2 - 1 Introduction

The Fluorine-doped $SnO_2$ is an excellent transparent conductive oxide (TCO), which is widely used in optoelectronic devices [133]. In addition, $SnO_2$ is well-known for its gas sensing properties and attracts much interest from many searchers for photovoltaic applications due to its transparency in the visible domain and good conductivity [134]. Moreover, $SnO_2$ films doped with F or Sb seem to be the most appropriate for use in solar cells due to its low electrical resistivity and high optical transmittance [135]. What is the more, the fluoride ion is preferred because the doped films exhibit high transparency and good electrical conductivity [136].

Xu et al. have been investigated the electronic structure of F-doped $SnO_2$ within $Sn_8O_{15}F$ system, the results show that the charge density distribution displays no significant change while the energy of the valence electrons is reduced after introducing the F impurity [50].
In terms of magnetic and electronic properties of $SnO_2$ defects, Rahman et al. have shown that the tin vacancy ($V_{Sn}$) induced a magnetic moment around 4.00 $\mu_B$. The major contribution to the moment comes from O atoms surrounding by $V_{Sn}$ and Sn atoms, which coupled antiferromagnetically with the O atoms in the presence of $V_{Sn}$ [137]. Moreover, the physical properties of oxides depend strongly on the stoichiometric composition, nature and the concentrations of the incorporated atoms in the crystal lattice. The tin oxide is n-type semiconductor, either oxygen vacancy ($V_O$) or Sn interstitial ($Sn_i$) are expected to be donors in pure $SnO_2$ [138].

At this point, Wang et al.[139] noticed that the neutral $Sn_i$ , $V_O$ and ($Sn_i$ and $V_O$) pair defect does not induce magnetic moment in $SnO_2$ bulk. Where the $V_O$ has been suggested to be the key factor in turning the ferromagnetism in undoped $SnO_2$. The only single positively charged O vacancies, noticed as $V_O^{1+}$, can induce local magnetic moments in $SnO_2$ bulk. In addition, $SnO_2$ has a direct wide band gap with $E_g$ = 3.6 eV. For this reason many efforts have been devoted to study experimentally and theoretically the magnetic properties of $SnO_2$ doped and co-doped with various transition metals (TM = V, Fe, Co, Cu, Cr, Zn...),[52, 54, 117, 140, 141-142]. For the Manganese (Mn) impurity, many studies and investigations have been done [51, 143-146]

Where, Mn doped $SnO_2$ recognized the stability of disordered local moment (DLM) [147].

The purpose of this work is investigating the possibility to have the stability of ferromagnetic (FM) for F-doped $Sn_{0.98}Mn_{0.02}O_2$ system. Since the FM state connected to the half metal has been extensively searched due to its potential applications in spintronic field.

### 3 - 2 - 2 Crystal structure and calculation method

The calculations are based on the density functional theory (DFT) within the Korringa–Kohn–Rostoker approximation [123-124] combined with the coherent potential approximation (CPA) and local density approximation (LDA) [92-93]. The LDA is based on the parameterization given by Moruzzi, Janak and Williams (MJW) [127]. We used the AKAI-KKR (MACHIKANEYAMA 2002V09) electronic structure calculations code developed by Akai [148].

In fact, the LDA is the simplest physical path to treat the exchange-correlation energy. It is the most widely used in applied DFT and based on the homogeneous electron gas model (HEG) that has the same electron density at the point. In our calculations, the scalar relativistic approximation was considered and the potential form is restricted to the muffin tin spheres are expanded with real harmonic up to l = 2, while l is the angular momentum at different sites.

For the current calculations, the obtained value of band gap is of 2.05 eV (figure 3.10), while the experimental value is of 3.6 eV [149]. The application of LDA to solids can lead, for example for semiconductors and insulators, to band gap which are not in full agreement with experimental results. This is due to the use of a potential which is the same for all orbitals. The band gap calculated from the eigenvalue spectrum differs from the true band gap by the derivative discontinuity of the exchange-correlation potential [130].

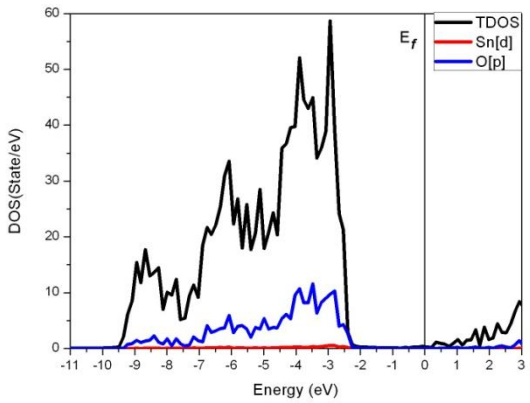

***Figure 3.10:*** *Total and Partial DOS (TDOS and PDOS) of the pure $SnO_2$ related to the Fermi energy; the black, Red and blue, respectively are the TDOS, Sn[d] and O[p] states.*

The rutile structure of $SnO_2$ has been considered. This crystalline structure has a tetragonal unit cell with two lattice parameters (a = 4.7373 and c = 3.1864 Å, with u = 0.307 Å) [128]. The space group of our system is $P4_2/mnm$ with six atoms. Two Sn atoms occupying the 2a Wyckoff positions (0,0,0); (½, ½,½) and four O occupying the 4f positions (u,u,0); (-u,-u,0); (½+u,½-u,½); (½-u,½+u,½). The system integrates also the primarily empty-spheres (Z=0) as an inter-sites. Then, for each atom, the sphere radius is taken such that the volume of the unit cell is the sum of the volumes of all atomic spheres. So, the current system incorporated eight inter-sites localized at the following positions: (½,0,-0.1682); (0,½,-0.1682); (0,½,0.1682); (½,0,0.1682); (-0.3125,0.3125,0); (-0.1875,-0.1875,0.3363); (0.1875,0.1875,0.3363); (0.3125,-0.3125,0), see figure 3.1. The considered valence states are Sn($4d^{10}5s^25p^2$) and O($1s^22s^22p^4$).

### 3 - 2 - 3 Results and Discussion

#### 3 - 2 - 3 - 1 The effect of defects on the stability of F-doped $SnO_2$ system.

In the present work, the considered point defects are fluorine Interstitial ($F_i$), oxygen interstitial ($O_i$) and oxygen vacancy ($V_O$). Therefore, we restricted our study in the following systems: $SnO_{2(1-x)}F_{2x}$ ; $SnO_2F\boldsymbol{i}_x$ ; $SnO_{2(1-x)}F_{2x}O\boldsymbol{i}_x$ and $SnO_2(V_O\frac{\mathbf{1}}{\mathbf{2}}{}_x)F\boldsymbol{i}_x$,with x = 0.01, 0.03 and 0.05. Then, we plotted the density of states (DOS) in order to evaluate the behavior of the conduction band (CB) and valence band (VB).

Figure 3.11 related to $SnO_{2\ (1-x)}F_{2x}$, shows that the Fermi level is shifted to the CB. We can observe the increasing of the occupied levels in CB by augmenting the fluorine concentration. This is due to the F[p] state. This behavior was reported in literature [50] within the LDA incorporated in ABNIT package.

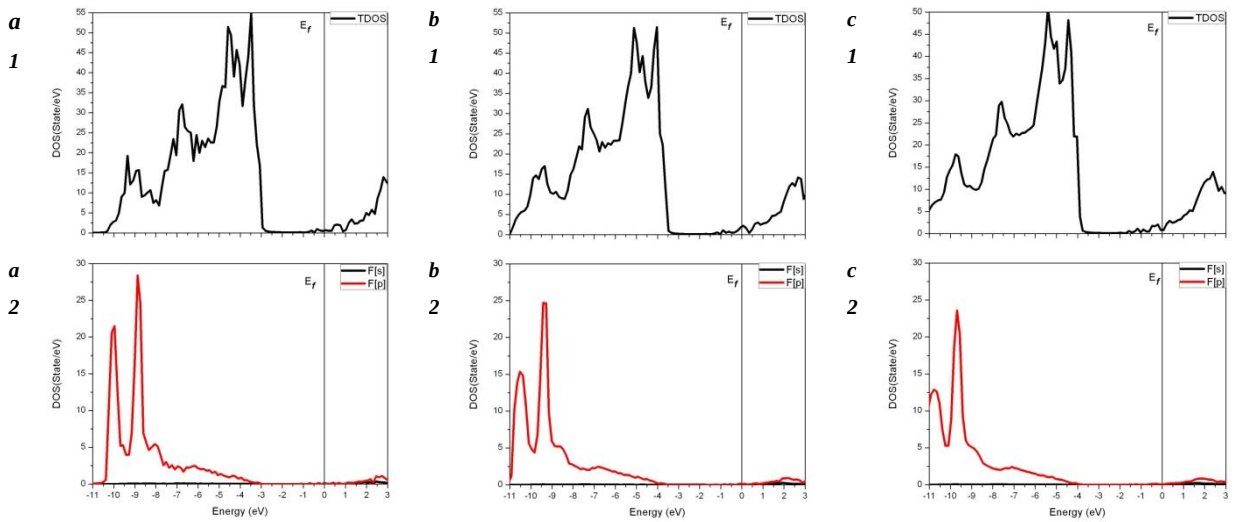


***Figure 3.11 (a, b, c):*** *Total and Partial DOS of the ($SnO_{2(1-x)}F_{2x}$)related to the Fermi energy, for x=0.01, 0.03 and 0.05, respectively. a (1), b (1) and c (1) are the TDOS; a (2), b (2) and c (2) are the PDOS of F[s] and F[p] indicating by the black and the red colors, respectively.*

For $SnO_2Fi_x$ related to figure 3.12 (a2, b2, c2), the Fermi level shifts to the top of the VB when F***i*** defect increased. This indicates the presence of p-type conductivity. Also, in $SnO_2(Vo_{\frac{1}{2}x})Fi_x$ system, see figure 3.14, the p-type conductivity is observed, consequently Vo is expected to be donor. Then, the p-type is induced by the presence of F***i***.

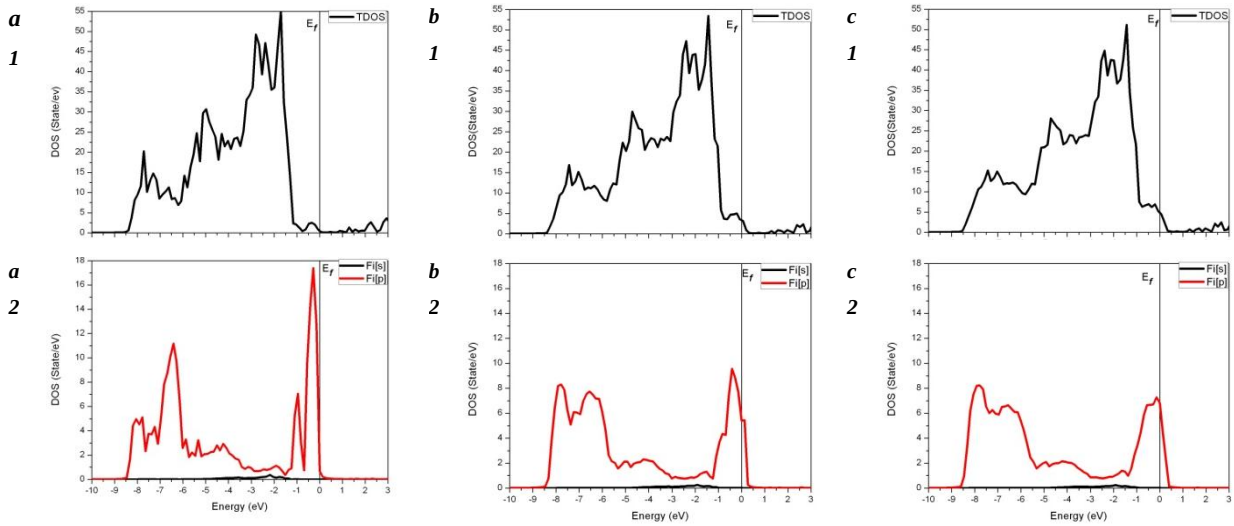


***Figure 3.12 (a, b, c):*** *Total and Partial DOS of the ($SnO_2Fi_x$) related to the Fermi energy, when x=0.01, 0.03 and 0.05, respectively. a (1), b (1) and c (1) are the TDOS; a (2), b (2) and c (2) are the PDOS of Fi[s] and Fi[p] indicating by the black and the red, respectively.*

Nevertheless, the partial (PDOS) of $SnO_{2(1-x)}F_{2x}O\boldsymbol{i}_x$ shows the energy levels around the occupied Fermi threshold, see figure 3.13. This fact induces the n-type conductivity. In addition, figure 3.13 (c) indicates that the origin of conductivity is due the O***i***[p] state. Here, we can predict that the Fermi level shifted to the CB. Consequently, the O***i*** defect is expected to increase the n-type conductivity of the material. The TDOS of $SnO_{2(1-x)}F_{2x}O\boldsymbol{i}_x$ comparedto the pure $SnO_2$ (see figure 3.10) indicates that the bottom of CB is expanded due to the presence of O***i*** defect.

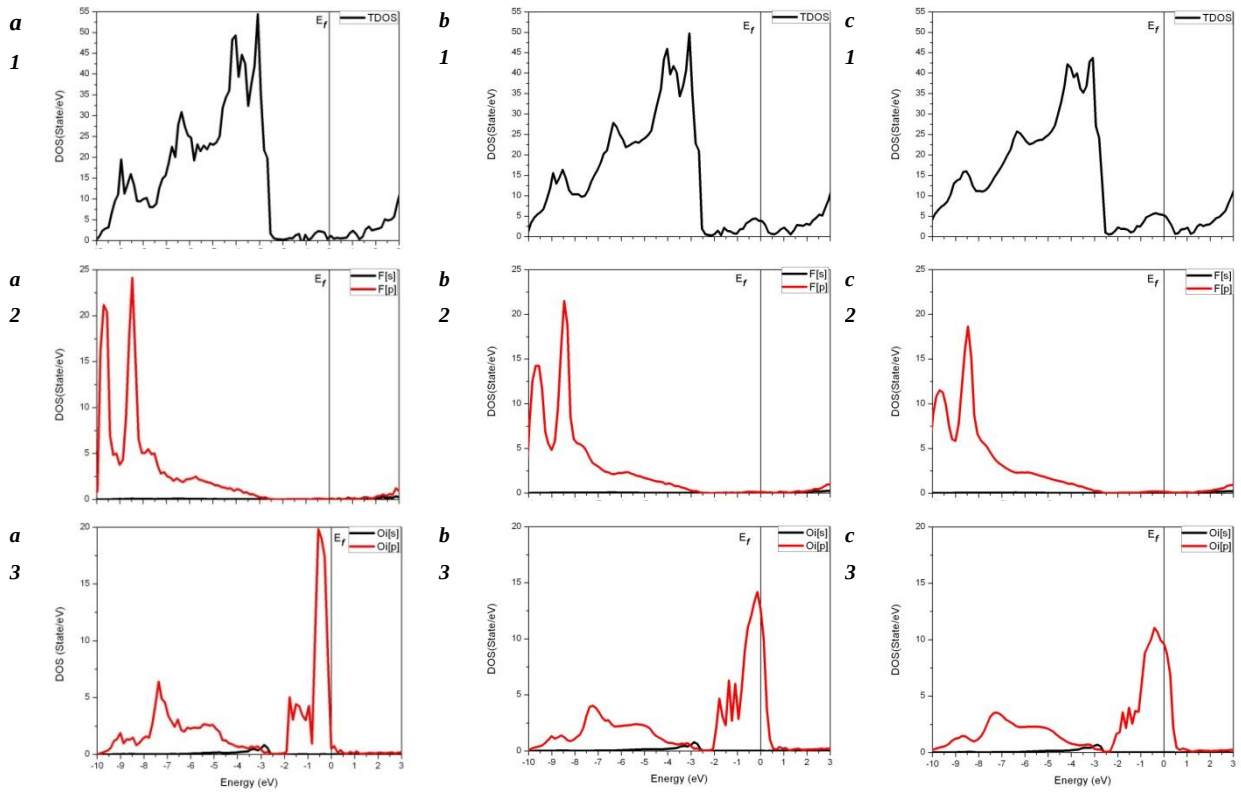


***Figure 3.13 (a, b, c):*** *Total and Partial DOS of the ($SnO_{2(1-x)}F_{2x}O\boldsymbol{i}_x$)related to the Fermi energy, when x=0.01, 0.03 and 0.05, respectively. a (1), b (1) and c (1) are the TDOS; a (2), b (2) and c (2) are the PDOS of F[s] and F[p] indicating by the black and the red, respectively. a (3), b (3) and c (3) are the PDOS of O**i**[s] and O**i**[p] indicating by the black and the red, respectively*

***a*** 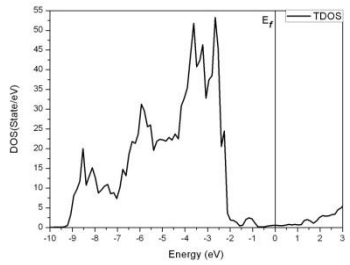

***b*** 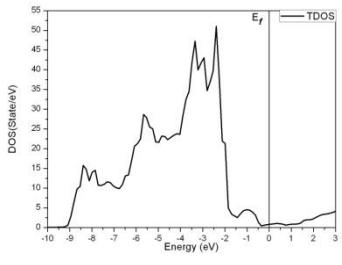

***c*** 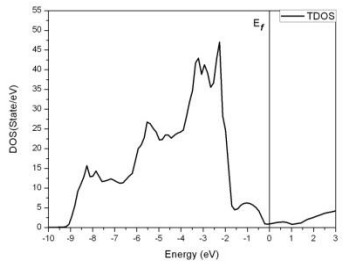


***Figure 3.14 (a, b, c):*** *Total DOS of the $SnO_2(V_{O\frac{1}{2}x})Fi_x$related to the Fermi energy, when x=0.01, 0.03 and 0.05, respectively.*

Since $SnO_2$ is an n-type semiconductor, we have evaluated only the formation energies of $SnO_{2(1-x)}F_{2x}$ and$SnO_{2(1-x)}F_{2x}O\boldsymbol{i}_x$ by the following formulas [150-151]

$$\Delta H(SnO_{2(1-x)}F_{2x}) = E(SnO_{2(1-x)}F_{2x}) - E_{pure}(SnO_2) + 2E(O) - 2E(F) \quad \textbf{(3.3)}$$

$$\Delta H(SnO_{2(1-x)}F_{2x}O\boldsymbol{i}_x) = E(SnO_{2(1-x)}F_{2x}O\boldsymbol{i}_x) - E_{pure}(SnO_2) + E(O) - 2E(F) \quad \textbf{(3.4)}$$

Where, $E_{pure}(SnO_2)$ is the total energy of the $SnO_2$ unit-cell and { $E(SnO_{2(1-x)}F_{2x})$ and $E(SnO_{2(1-x)}F_{2x}O\boldsymbol{i}_x)$ } are the total energies of the unit-cell of $SnO_{2(1-x)}F_{2x}$ and $SnO_{2(1-x)}F_{2x}O\boldsymbol{i}_x$.
E(O) and E(F) are the chemicals potential of O and F unit-cell in their reference states, respectively.
The calculated formation energies, with x = 0.05, are summarized in table 3.7. These results show that the stability of $SnO_{2(1-x)}F_{2x}O\boldsymbol{i}_x$ is higher than that of$SnO_{2(1-x)}F_{2x}$ system

| | Energy formation (eV) |
|---|---|
| $SnO_{2(1-x)}F_{2x}$ | -9.01 |
| $SnO_{2(1-x)}F_{2x}O\boldsymbol{i}_x$ | -9,50 |

***Table 3.7****: Formation energy with x = 0.05.*

For the remaining study, we restricted our investigation on $Sn_{0.98}Mn_{0.02}O_{1.95}F_{0.05}$ system to predict its magnetism behavior.

***-Magnetic properties in $Sn_{0.98}Mn_{0.02}O_{1.95}F_{0.05}$ system.***

The aim of this investigation is to study tin oxide semiconductor with double impurities (2p–3d) for $Sn_{0.98}Mn_{0.02}O_{1.95}F_{0.05}$ matrix rather than the regular single impurity. In fact, the double impurities in the present system can optimize the magnetic and electronic properties. Before talking about the effect of F impurity on $Sn_{0.98}Mn_{0.02}O_2$ system, it worthy to mention that 2% of Mn doped $SnO_2$ induced the disordered local moment (DLM) state [147] due to the majority-spin related to $e_g^+$ of Mn[d]. This latter band is unoccupied, and the Mn impurity has $d^3$ electron configuration due to the substitution of $Sn^{4+}$ by $Mn^{4+}$. Subsequently, there is no carrier to mediate the FM state. Besides this fact, the double impurities (Mn and F) have an effect on the conversion of the $Sn_{0.98}Mn_{0.02}O_{1.95}F_{0.05}$ to FM state. To clarify this fact, we plotted the PDOS of Mn related to ($Sn_{0.98}Mn_{0.02}O_2$ and $Sn_{0.98}Mn_{0.02}O_{1.95}F_{0.05}$)to evaluate the stability state of these systems, see figure 3.15 (a, b).

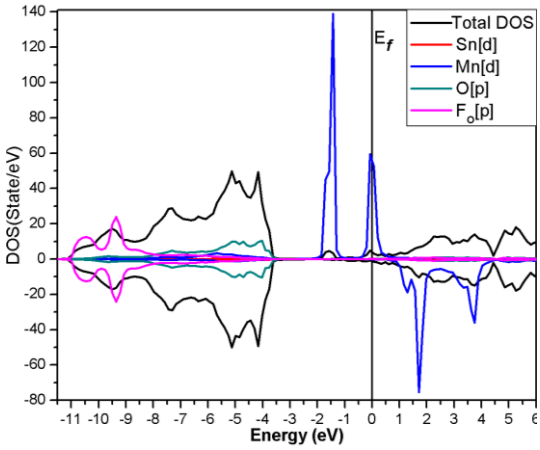


***Figure 3.15 (a):****TDOS and PDOS of $Sn_{0.98}Mn_{0.02}O_{1.95}F_{0.05}$ related to the Fermi energy; the black, Red blue, green and pink respectively are the TDOS, Sn[d], Mn[d] O[p] and $F_O$[p] states.*

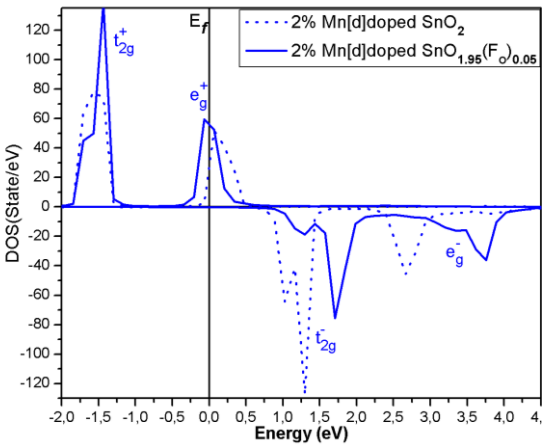


***Figure 3.15 (b):*** *The Mn[d] state presentation in $Sn_{0.98}Mn_{0.02}O_2$ and $Sn_{0.98}Mn_{0.02}O_{1.95}F_{0.05}$.*

Where, figure 3.15 (a) shows that the VB and CB are predominantly contributed by F[2p], O[2p] and Sn[3d]. Where, the spin polarization around the Fermi level is mainly composed of Mn[3d] states and the nearest neighbouring F[2p] states. Since Mn($3d^5 4s^2$) has seven electrons in $SnO_2$, which is doped in the octahedral site of tin , it becomes $Mn^{3+}$($3d^4$) when F

impurity occurred. Moreover, the d orbital of Mn is divided into two states: $e_g(d_{x-y}^2, d_z^2)$ and $t_{2g}(d_{xy}, d_{yz}, d_{xz})$, which are the high and the low energy states, respectively, due to electronic field created by six ligands corresponding to octahedral crystal field. In this case, $Mn^{3+}(3d^4)$ will have four Mn electrons. Then, three electrons will fill the majority-spin related to $t_{2g}^+$ on VB side and the remaining electron will be in the majority-spin related to $e_g^+$. That is why $e_g^+$ is situated slightly to the Fermi level and having the half metallic characteristic in $Sn_{0.98}Mn_{0.02}O_{1.95}F_{0.05}$. While the remaining $t_{2g}^-$and $e_g^-$ will be empty in the CB to the right of the Fermi level. Then, we predict the stability of FM in $Sn_{0.98}Mn_{0.02}O_{1.95}F_{0.05}$ system instead the presence of DLM in $Sn_{0.98}Mn_{0.02}O_2$.

From The DOS of figure 3.15 compared to figure 3.10, we noticed a decrease in the gap energy. This observation exhibits that additional n-type carriers are required to stabilize the FM state and the Curie temperature of the present system is expected to increase with the increasing of n-type carriers. This behavior is noticed in V-doped $SnO_2$ [120].

To verify the FM stability, we can evaluate the total energy difference (ΔE) between the DLM and FM states **(3.1)**.

Where $E_{DLM}$ and $E_{ferro}$ stand for the total energies of the DLM and the FM states, respectively. The DLM state is simulated by state in which half of the impurity ion spins point in the upward direction and the rest points in the opposite direction. Where $Sn_{0.98}Mn_{0.01}^{up}Mn_{0.01}^{down}O_{1.95}F_{0.025}^{up}F_{0.025}^{down}$ stands for the DLM state and $Sn_{0.98}Mn_{0.02}^{up}O_{1.95}F_{0.05}^{up}$ for the FM state in which all spins have one direction. Our results show that the difference of energy ΔE= 1.375 meV, then ΔE>0. This fact indicates the stability of FM state and pushes us to calculate the mean-field Curie temperature ($T_C$) by using the mean-field method (MFA), **(3.2).**

As a result, $T_C$ = 152.03 K. For $Sn_{0.98}Mn_{0.02}O_{1.95}F_{0.05}$, the spin up of Mn approaches to the Fermi level, where the spin down moves away from it figure 3.15 (b). Subsequently, we can predict the presence of p–d exchange [152].

The total magnetic moment of unit cell is of 0.176 and 0.134 $\mu_B$, for $Sn_{0.98}Mn_{0.02}O_{1.95}F_{0.05}$ and $Sn_{0.98}Mn_{0.02}O_2$, respectively. The partial moments are $M^{Mn}$ =3.694 and $M^F$ =0.003 $\mu_B$, see table 3.8. The major contribution to the moment comes from Mn and ($M^{Mn} >> M^F$). Moreover, from figure 3.15 (b), we observe in $Sn_{0.98}Mn_{0.02}O_2$ system that the exchange

splitting between $e_g^+$ and $e_g^-$ states is larger than the crystal field splitting between $e_g$ and $t_{2g}$ states. For $Sn_{0.98}Mn_{0.02}O_{1.95}F_{0.05}$ compared to$Sn_{0.98}Mn_{0.02}O_2$, the exchange splitting has increased andthe total magnetic moment augmented due to fluorine impurity.

| | ΔE (meV) | Tc(K) | state | $M^T(\mu_B)$ | $M^{Sn}$ ($\mu_B$) | $M^{Mn}$ ($\mu_B$) | $M^O(\mu_B)$ | $M^F$ ($\mu_B$) |
|---|---|---|---|---|---|---|---|---|
| $Sn_{0.98}Mn_{0.02}O_2$ | -0 .211 | ---- | DLM | 0.134 | 0.0007 | 3.183 | 0.0009 | ---- |
| $Sn_{0.98}Mn_{0.02}O_{1.95}F_{0.05}$ | 1.375 | 152.03 | FM | 0.176 | 0.0016 | 3.694 | 0.0017 | 0.003 |

***Table 3.8:*** *Energies and magnetic facts, comparison between $Sn_{0.98}Mn_{0.02}O_2$ and $Sn_{0.98}Mn_{0.02}O_{1.95}F_{0.05}$.*

### 3 - 2 - 4 Conclusion

The Korringa-Kohn-Rostoker method combined with the Coherent Potential Approximation (KKR-CPA) has been used to study the electronic structure and magnetic properties of $\mathbf{Sn_{0.98}Mn_{0.02}O_{1.95}F_{0.05}}$. Our results have shown that 5% of fluorine could induce the FM state instead DLM. Since the majority-spin related to$e_g^+$is located around the Fermi level. The half metal characteristic is observed.

Additionally, in $Sn_{0.98}Mn_{0.02}O_2$ system, we notice that the exchange splitting between $e_g^+$and $e_g^-$ states is larger than the crystal field splitting between $e_g$ and $t_{2g}$ states, for $Sn_{0.98}Mn_{0.02}O_{1.95}F_{0.05}$ compared to$Sn_{0.98}Mn_{0.02}O_2$, the exchange splitting has increased.

## 3 - 3 - Magnetic properties of Co-(Os, Mn) co-doped ZrO2 within GGA and mBJ approaches

### 3 - 3 - 1 Introduction

In the last decades, diluted magnetic semiconductors (DMSs) have been investigated extensively. One of the current priorities in the science is the development of advanced materials technologies that are based on (DMS), [71, 153]. (DMSs) considered as compounds based on the typical types of semiconductors: Zn, $TiO_2$, $SnO_2$….[147]. Zirconia ($ZrO_2$) is a p-type semiconductor including a large and indirect band gap $E_g$= 6.1eV in the cubic ground

state phase, then having a bigger band gap other than tetragonal and monoclinic ones (5.87 and 5.83) eV, respectively [154]. Recently, the stabilization of $ZrO_2$ (cubic phase) by transition metal doping were theoretical and experimentally investigated by several groups [36, 155-156]; Boujnah et al. [36] found that the V, Mn and Fe provide half-metalic properties considered to be the leading cause, responsible for ferromagnetism. The fabrication of $ZrO_2$based (DMS) is a challenging objective, as this would combine the advantages of $ZrO_2$ with the enhanced magnetic properties, what is more, the applications of such a material appear in many places like: gas sensors, solid fuel cells, high durability coating, and catalytic agents [58-59]. Moreover, that material involves a large band offset in direct contact with Silicium and good thermal stability, these key points have led $ZrO_2$ to be extensively studied [59, 115, 157].

Using (DFT) within the Full-Potential Linearized Augmented Plane Wave (FP-LAPW) method in connection with (GGA and mBJ) approximations have been included, we were choosing mBJ besides DFT-GGA because the first one is in good agreement with experimental results in terms of the optical band gaps rather than GGA, and many studies believe in that: Abbassi et al. [158] noticed this truth for ZnO. Also Boujnah et al. [159] have shown that the band gap of spinels ($CdGa_2O_4$ and $CdIn_2O_4$) are close to the experimental values than GGA. Moreover, the (GGA-mBJ) is a modification employed especially on semiconductors and insulator materials; it gives accurate results and wide gaps [160]. We have studied the electronic structure and magnetic properties of (5d- 3d and 3d-3d) transition metal related to (Os, Co) and (Mn, Co) co-doped $ZrO_2$, respectively. In particular, the predicted exchange splitting between $e_g$ states versus the crystal field splitting between $e_g$ and $t_{2g}$behavior in case of $Zr_{14}TMCoO_{32}$system for both (GGA and mBJ) and refer them to the single impurities systems: $Zr_{15}CoO_{32}$, $Zr_{15}OsO_{32}$and $Zr_{15}MnO_{32}$.

### 3 - 3 - 2 Computational details

For $Z_{14}TMCoO_2$ when (TM = Os, Mn), the First principles calculations are performed using the (FP-LAPW) method based on spin-polarized density functional theory (SDFT), as implemented in the Wien2k code **[114]**. The electronic structure and magnetic properties were calculated within the generalized gradient approximation: (GGA) of Perdew-Burke-Ernzerhof: (PBE)**[98]** and the modified Becke–Johnson: (mBJ) **[100]** exchange correlation potential.

Recently Tran and Blaha proposed to introduce the parameter c into the original BJ exchange potential **[101]** as the following formula:

$$\upsilon_{\chi,\sigma}^{mBJ}(r) = c\upsilon_{\chi,\sigma}^{BR}(r) + (3c-2)\frac{1}{\pi}\sqrt{\frac{5}{12}}\sqrt{\frac{2t_\sigma(r)}{n_\sigma(r)}}$$

Where n□□is the spin dependent electron density and t□ is the spin dependent kinetic-energy density. $V^{BR}$ is the Becke Roussel potential **[102]**; within the mBJ potential, the parameter c was proposed to be determined self consistently from the density by the following:

$$c = \alpha + \beta\left(\frac{1}{V_{cell}}\int_{cell}\frac{|\nabla_n(r')|}{n(r')}\,d^3r'\right)^{1/2}$$

These parameters have been chosen to suit the band gaps in a broad range of solids. That calculation was done with a scalar relativistic approach without spin orbit coupling; the partial waves inside the atomic spheres are expanded up to the angular momentum $l_{max}$=10 with $R_{MT}$ x $k_{max}$= 7, which determines the matrix size, when $R_{MT}$ is the smallest muffin tin radius and $k_{max}$ is the maximum value of the wave vector; the self consistency is obtained by 250 k-points in the irreducible symmetry wedge of the first Brillouin zone. $ZrO_2$(bulk) exhibits cubic structure: space group Fm3m and the lattice coordinates of one Zr position atom is located at (0, 0, 0) and the two O positions atoms are located at ($\frac{3}{4}$, $\frac{3}{4}$, $\frac{3}{4}$) and ($\frac{1}{4}$,$\frac{1}{4}$, $\frac{1}{4}$), the parameters of $ZrO_2$ (cubic) unit cell are a = b = c, the experimentally a between (5.09 and 5.25) å [161], in the current calculation we took a = 5.137 å, we considered 2x2x1 cubic supercell model to simulate the ordered cubic structure of $Z_{14}TMCoO_2$ based DMS.

Our results have achieved a good convergence in both cases of GGA and mBJ approaches: less than $10^{-5}$ e for charge convergence and $10^{-4}$Ry for energy.

### 3 - 3 - 3 Results and discussion

***-(Co, Os and Mn) doped $ZrO_2$***

The used concentration in the current system is 12.50%, two Zr replaced by a Co and TM (Mn or Os) atoms, the Co and (Mn or Os) kept 6.25% for each one, the obtained calculation modeling shows that the most stable energy in this host system is d($Co_0$-$Co_3$) presented in the figure 3.16 (c) when the distance between Co-Co around 9.7075Bohr, in this case the partial moment of each Co is 2.42/2.38 **μB** which indicate the strong coupling in that position, see table 3.9; based on the previous magnetism facts, we well considered the supercell of figure

3.16 (c) keeping Co beside the second substituted TM (Mn or Os) position. Therefore, this study of $ZrO_2$ semiconductor doped with double class of transition metal Mn (3d) and Os (5d) systems using both GGA beside mBJ rather than the ordinary single impurities.

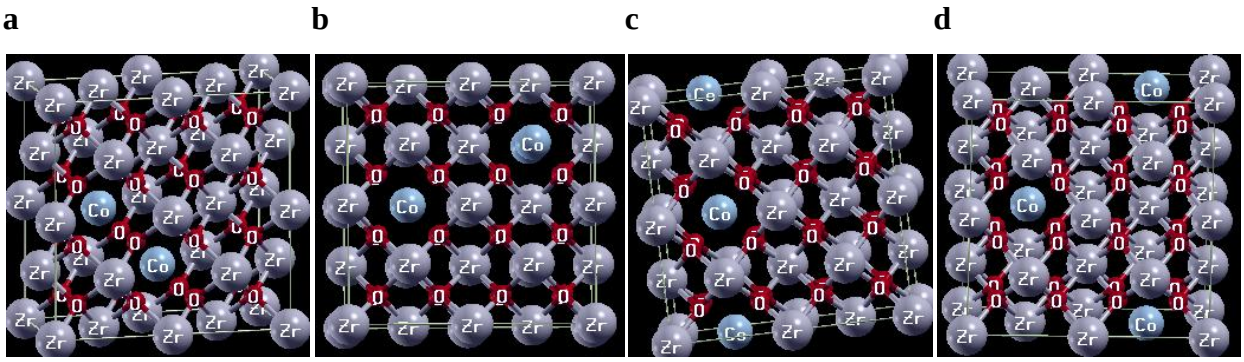


***Figure 3.16:*** *supercells of the cubic $ZrO_2$, the gray, red and blue spheres are Zr, O and substituded Co in different sites.*

| d($Co_0$-$Co_i$) | $M^{Total}(\mu_B)$ | $M^{[Co_0/Co_i]}(\mu_B)$ | Energy(eV) |
|---|---|---|---|
| d($Co_0$-$Co_1$) | 4.89398 | 2.53/2.34 | -111173.76793733 |
| d($Co_0$-$Co_2$) | 2.0017 | 1.62/1.62 | -111173.76560644 |
| d($Co_0$-$Co_3$) | 4.41968 | 2.42/2.38 | -111173.98232866 |
| d($Co_0$-$Co_4$) | 2.56879 | 1.69/1.93 | -111173.76310437 |

***Table 3.9:*** *Total and partial moments ($Co_0$/$Co_i$) and energies facts in different proposed distances [d($Co_0$-$Co_i$)] related to supercells of* ***figure 3.16.***

Before talking about the co-doped statements, we would like to remember that is (Co or Mn) doped $ZrO_2$ beside O ions form a cubic crystal field, that is to say, the d orbitals are splitting into the lower doubly degenerate and the higher triply degenerate states: $e_g(d_{x-y}^2, d_z^2)$ and $t_{2g}(d_{xy}, d_{yz}, d_{xz})$. For the $Zr_{15}CoO_{32}$ as indicated by Boujnah et al. [36] the crystal field splitting between $e_g$ and $t_{2g}$ is larger than the exchange splitting. In contrast the exchange splitting for $Zr_{15}MnO_{32}$ is larger that of the crystal field as indicated figure 3.19 (a) and figure 3.20 (a), while the total moments of (Co and Mn) within GGA are 1.11 and 3.39 $\mu_B$ respectively; as a remarks, the impact and the presence of crystal field beside the exchange sharps splitting is related to the total moments of the TM, but for the $Zr_{15}OsO_{32}$ there is no evidence of moment

magnetic presence when the up and down sides of TDOS are symmetric, see figure 3.17 (a) and figure 3.18 (a).

**(a)** $Zr_{15}OsO_{32}$ **(b)** $Zr_{15}CoO_{32}$

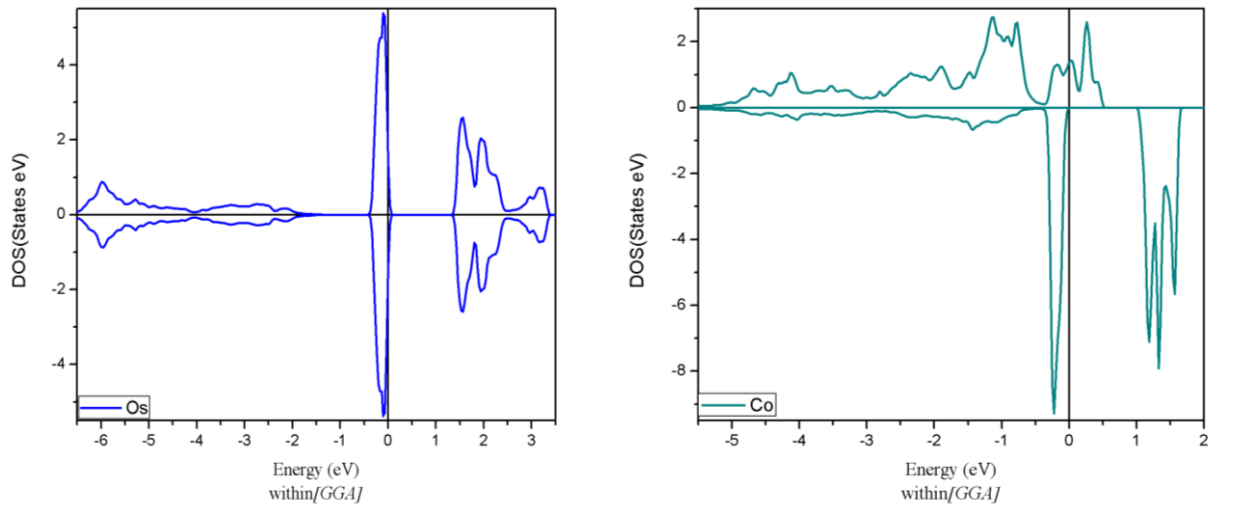


**(c)** $Zr_{14}OsCoO_{32}$ **(d)** $Zr_{14}OsCoO_{32}$

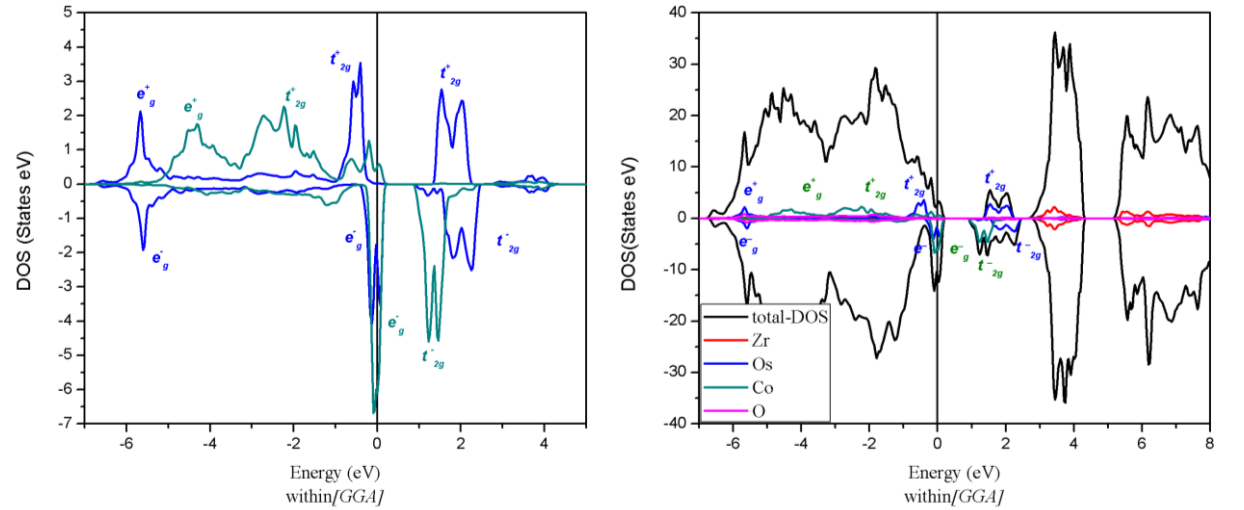


***Figure 3.17:*** *Total and Partial DOS, the black, red, blue, green and pink respectively are the TDOS, Zr[d], Os[d], Co[d] and O[p] orbitalsrelated to the Fermi energy; within* ***GGA****.*

**(a)** $Zr_{15}OsO_{32}$ **(b)** $Zr_{15}CoO_{32}$

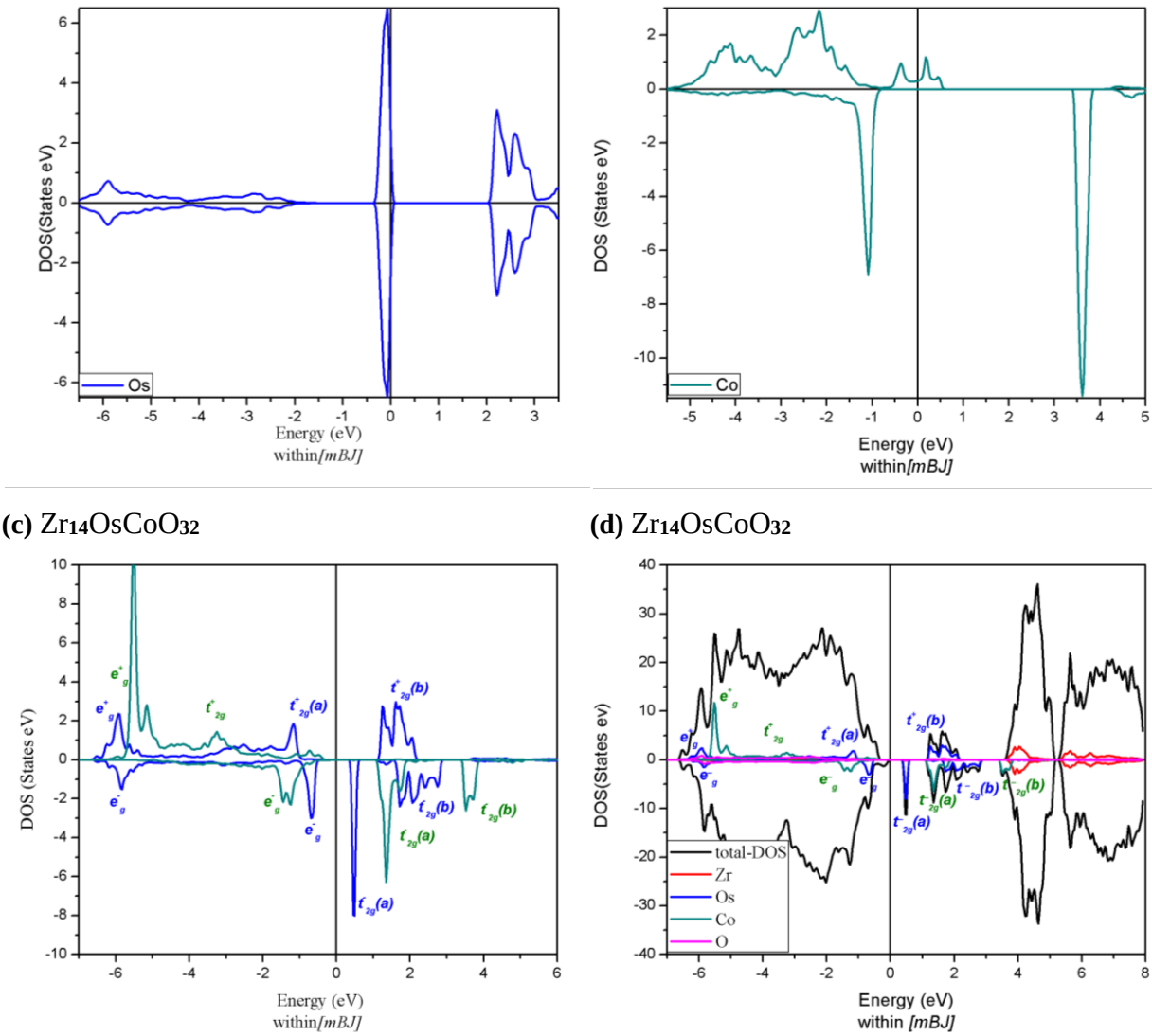


**(c)** $Zr_{14}OsCoO_{32}$ **(d)** $Zr_{14}OsCoO_{32}$

***Figure 3.18:*** *Total and Partial DOS, the black, red, blue, green and pink respectively are the TDOS, Zr[d], Os[d], Co[d] and O[p] orbitalsrelated to the Fermi energy; within* ***mBJ****.*

***-(Os, Co) co-doped $ZrO_2$***

As shown in the table 3.10, the total magnetic moment of Co in $Zr_{14}OsCoO_{32}$ is around 2.77 instead1.11$\mu_B$ when we have$Zr_{15}CoO_{32}$**.** the crystal field is narrowed front of the exchange splitting when we considered (Os beside Co) rather than $Zr_{15}CoO_{32}$ system, as presented in figure 3.17 (c). The total moment of Os is 0,55 and 1 µB within (GGA and mBJ) respectively, this modest $M^{Os}$ due the crystal field splitting of Os which is larger than the exchange splitting in (Os, Co) co-doped $ZrO_2$. Although for $Zr_{15}OsO_{32}$ the plotted TDOS shown that is no evidence of the magnetic presence and the moment total of system is 0 $\mu_B$, see figure 3.17 (a) and figure 3.18 (a). However, in the case of $Zr_{14}OsCoO_{32}$, we have two statements: on one

hand, within GGA, $Zr_{14}OsCoO_{32}$ system provides the coupling between Os[5d] and Co[3d] see figure 3.17 (c), and the half metallic behavior is estimated although is not 100% polarized on the down side of Fermi level.

| | | **Band gab (eV)** | **$M^{Total}(\mu_B)$** | **$M^{[Co/TM]}(\mu_B)$** | **Energy(eV)** |
|---|---|---|---|---|---|
| $Zr_{14}OsCoO_{32}$ | GGA | --- | 4.15 | 2,77/0,55 | -142951.11692986 |
| | mBJ | 0.45 | 5.00 | 3.24/1.00 | -142781.87931121 |
| $Zr_{14}MnCoO_{32}$ | GGA | --- | 5.14 | 2.42/3.42 | -110704.53639681 |
| | mBJ | --- | 4.00 | 3.9/2.5 | -110550.85552336 |

***Table 3.10:*** *Total magnetic moments and energies facts in $Zr_{14}TMCoO_{32}$ within GGA and mBJ.*

In addition, the charge state within mBJ approach is more close to the ($Os^{3+}$ and $Co^{2+}$) electronic configuration, that predict the occupation of the electronic configuration as $5d^5$ and $3d^7$ for (Os and Co), respectively, this fact indicates that(5d of Os having2 spin in $e^+_g$ state and 3 remaining in $t^+_{2g}$ state) and (3d of Co has 4 spin in $e^+_g$ and 3spin $t^+_{2g}$state), here we addressed the question to theJahn-Teller-effect spin distribution to understand the ferromagnetic mechanism in $Zr_{14}OsCoO_{32}$host system, for this purpose, the figure 3.17 (c, d) has been introduced, throughout PDOS presence of Os[5d] and Co[3d], for Os we can estimate both the majorities spin up/down of $e^+_g$ and $t^+_{2g}$ are completely filled because a part of $t^+_{2g}$ is appeared around (1.40 to 2.40) eV when the minorities spin are empty; besides that , with $d^7$ of Co we can notice that the $t^+_{2g}$ of the majority spin is appeared around (-2.90 to 0.20) eV, then both spin up/down of $e^+_g$ should to be completely filled to have 3 spin up in $t^+_{2g}$ for this arrange of energy while the minorities spin of Co are empty. Within mBJ and from figure 3.18 (c, d) beside table 3.10: a band gap is observed included the value of 0.45 eV with a localization of $e_g$ and $t_{2g}$ levels to low energy of valence band (VB).

***- (Co, Mn) co-doped $ZrO_2$***

In the present $Zr_{14}MnCoO_{32}$, the estimated calculations of the total magnetic moment are: ($M^{Co/Mn}$= 2.42/3.42 $\mu_B$ and the $M^T$ = 5.14 $\mu_B$) within GGA instead ($M^{Co/Mn}$= 3.9/2.5 $\mu_B$ and $M^T$ = 4.00 $\mu_B$) within mBJ, as shown in the table 3.10; here we should mention that ($M^{Co}_{GGA} < M^{Mn}_{GGA}$) instead ($M^{Co}_{mBJ} > M^{Mn}_{mBJ}$), even more ($M^{T}_{GGA} > M^{T}_{mBJ}$). When the mBJ used, the observed $M^{Mn}$ = 2.7 $\mu_B$ in $Zr_{15}MnO_{32}$ but in $Zr_{14}MnCoO_{32}$, we have $M^{Mn}$ = 2.5 $\mu_B$, table 3.10;

moreover, in figure 3.19 (c), the system provides the hybridization between M[3d] and Co[3d] as shown for $t^{+}_{2g(Mn)}$ state having the up side of Fermi level, when the $e^{-}_{g(Co)}$ state found on the down side and half metallic behavior is estimated, even more for Co[3d] we do not have 100% polarized on the down side of Fermi level, and for the electronic configuration, the present calculations indicate that in $Zr_{14}MnCoO_{32}$ having ($Mn^{2+}$ and $Co^{2+}$), so we could explain the magnetic behavior in this case by the predict occupied electronic configuration, while (Mn and Co) having ($3d^5$ and $3d^7$), respectively, this information indicates that (3d of Mn with 2 spin in $e^{+}_{g}$ state and 3 in $t^{+}_{2g}$ state bedside 3d of Co having 4 spin in $e^{+}_{g}$ and 3spin $t^{+}_{2g}$ state).

**(a)** $Zr_{15}MnO_{32}$ **(b)** $Zr_{15}CoO_{32}$

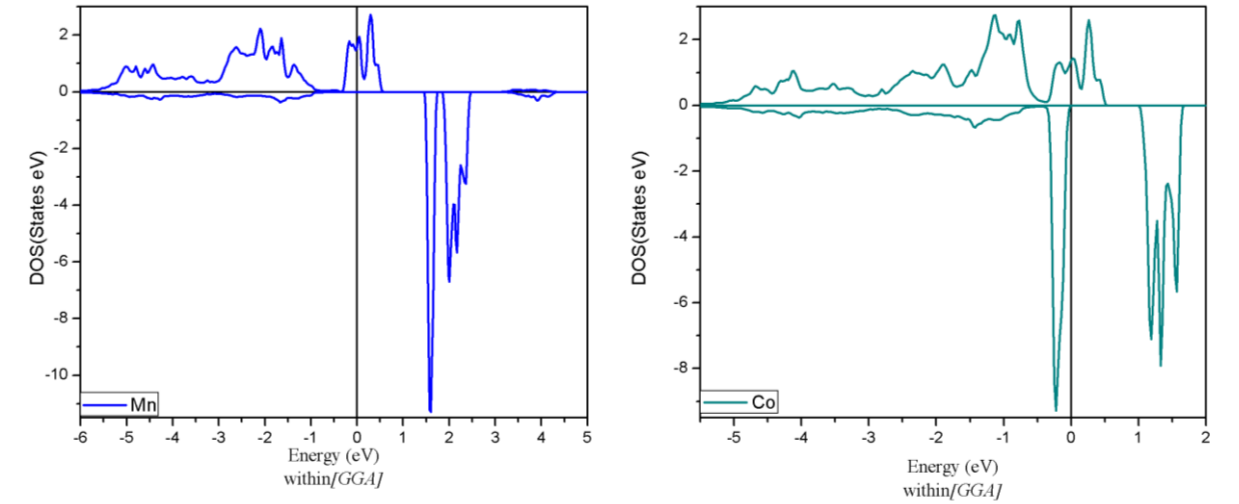


**(c)** $Zr_{14}MnCoO_{32}$ **(d)** $Zr_{14}MnCoO_{32}$

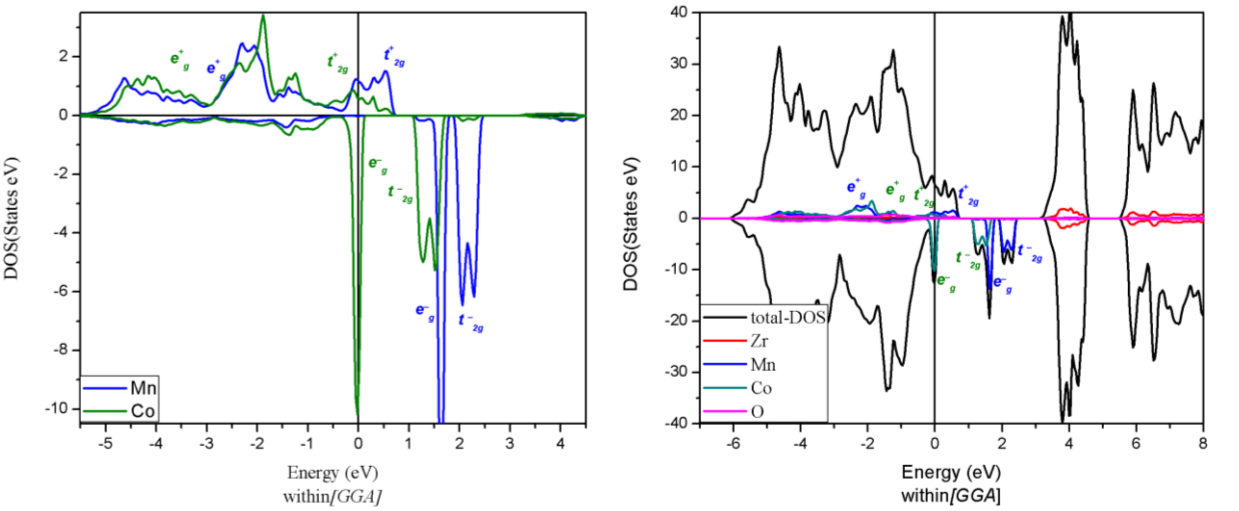


***Figure 3.19:*** *Total and Partial DOS, the black, red, blue, green and pink respectively are the TDOS, Zr[d],Mn[d], Co[d] and O[p] orbitalsrelated to the Fermi energy; within* ***GGA****.*

In figure 3.19 (c, d), the PDOS of Mn[3d] and Co[3d] could estimate the Jahn-Teller-effect spin allocation, in Mn: the majorities spin up of $e^{+}_{g}$ and $t^{+}_{2g}$ are completely filled, $t^{+}_{2g}$ is appeared around Fermi level when the minorities spin are empty. Besides that, Co[3d] noticed that the $t^{+}_{2g}$ of the majority spin is appeared on -2.95 to 0.75 eV, then both spin up/down of $e^{+}_{g}$ should to be completely filled in order having 3 spin up in $t^{+}_{2g}$ for this arrange of energy while the minorities spin of Co[3d] are empty. For mBJ's impact on $Zr_{14}MnCoO_{32}$ system, we would like to mention that the main obtained remarks on the crystal field beside exchange splitting are those of PDOS aspects, when we have compared the figure 3.19 (c) and figure 3.20 (c): the increased of that crystal field splitting between ($e_g$, $t_{2g}$) into Mn, in contrast the Co will know an increased of that exchange splitting in $e_g$ according the GGA modeling. This behavior explain that the $M^T$ values is related to the crystal field versus the exchange splitting in (3d-3d) co-doped present's system and not depends of that ( $M^{Mn}$ versus $M^{Co}$), see table 3.10, figure 3.19 (c) and figure 3.20 (c).

**(a)** $Zr_{15}MnO_{32}$ **(b)** $Zr_{15}CoO_{32}$

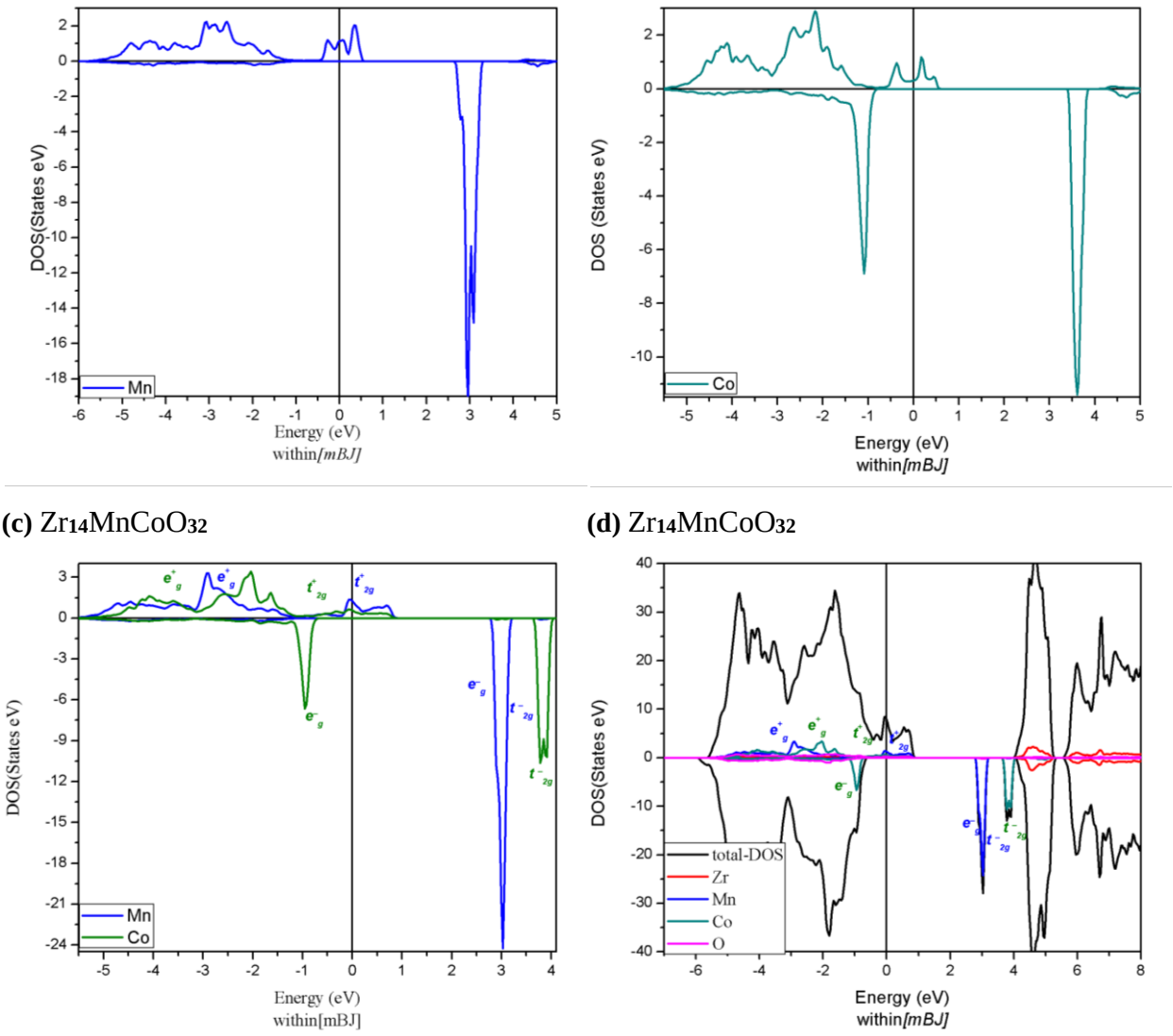


**(c)** $Zr_{14}MnCoO_{32}$ **(d)** $Zr_{14}MnCoO_{32}$

***Figure 3.20:*** *Total and Partial DOS, the black, red, blue, green and pink respectively are the TDOS, Zr[d],Mn[d], Co[d] and O[p] orbitalsrelated to the Fermi energy; within* ***mBJ****.*

### 3 - 3 - 4 Conclusion

To sum up this work, within DFT including (GGA and mBJ) approaches, the electronic structure and magnetic properties have been investigated. Our calculation shows the half metallic behavior even it is not 100% polarized for GGA, but in $Zr_{14}OsCoO_{32}$ the presences of magnetic gap is predicted with mBJ, also we revealed the impact of exchange splitting between $e_g$ states versus the crystal field splitting between $e_g$ and $t_{2g}$in (Os, Co) and (Mn, Co) doped $ZrO_2$ and the influence of that on the $M^T$ of the studied system; to determinate the most probably approach, the experimentally band gap in $ZrO_2$ is close to that of obtained with mBJ.

## 3 - 4 - The magnetism behavior of $Fe_{0.93}V_{0.02}Cr_{0.05}S_2$ pyrite within ab-initio calculation

### 3 - 4 - 1 Introduction

The most common naturally taking place metal sulphide is $FeS_2$ pyrite structured [162], Pearce et al. [64] talked about the electrical and magnetic proprieties of sulfides ($MnS_2$ hauerite , $FeS_2$ pyrite, $NiS_2$ vaesite…etc) as well as his point of view that the sulfurs have a major areas of potential technological exploitation in photovoltaics and in solar energy conversion devices, magnetic recording devices, etc....

since the semiconductors are requested in now day to develop (spintronic and other related applications) we're going to focus the present work on $FeS_2$ pyrite as a dilated magnetic semiconductor (DMS), because transition metal (TM) sulphide minerals having an immense industrial beside technological and economic values, those minerals considered as the major source of metals, moreover, the valuable metals such as gold and platinum group elements are often associating with the (sulphide ores) [163]; naturally occurred pyrite is mainly commonly founding in three main crystal forms, the most common is: the cubic form (100) surface, also found in octahedral (111) surface and pyritohedral (210) surface crystals[164]. The (DMS) study within simulation combined with the different method and approach is helpful complement beside the experimental side, for this purpose, many studies token place in semiconductors simulation, as example, we were found M. Boujnah et al. [36] talking about the ferromagnetism and optical absorption in cubic $ZrO_2$ within (mBj and GGA) approach using (WIEN2K) code, also in [147] the magnetism was studied in rutile $Sn_{0.98-x}Mn_{0.02}Cr_xO_2$ with (LDA and GGA) approximations integrated: Akai-KKR (MACHIKANEYAMA2002v09) code, and for $FeS_2$ pyrite many theoretically and experimentally studies have been done, Zhao et al. signed in his calculation using (LCAO) method and (self consistent local spin density) associated to ($CoS_2$ and $FeS_2$) pyrite, that $FeS_2$ has amoderately (small band gap) semiconductor and $CoS_2$ to be an almost half metallic ferromagnet [165]; in addition, Zhang et al [166] cited that the effect of surface stoichiometry on stability, band gap and electronic structure for a series of $FeS_2$ (100) pyrite while the bulk $FeS_2$ is nonmagnetic. Also, Hung et al [167] have been contributed in the $FeS_2$ pyrite (100 and 110) surfaces within calculation study using both (VASP and CRYSTAL98) codes, so, their calculations indicate that the $FeS_2$ pyrite (100) surface is more stable than the planar (110), which is expected to have a higher surface energy; Kolb et al. [168] used fully self consistent

(GW calculations) and demonstrating that a phonon mode is related to the oscillated of the S-S bond distance in pyrite structure is coupled robustly to the energy of (conduction band minimum) leaded to an ultrafast ≈ 100 fs oscillation in the band gap. At the side of the experimental, it is a diamagnetic semiconductor having an experimentally determined band gap of (~ 0.95 eV) in [169].

Baláž et al. were talking about the magnetic proprieties of nano-powders prepared by pyrite when they described the experimental setup and the mechanochemical reaction between $FeS_2$ pyrite and elemental iron (Fe) to get the (FeS troilite) as the follow ($FeS_2+Fe \rightarrow FeS$)[170]. Moreover, Cabán-Acevedo et al. cited in [171] that electrical transport measurements showed the pyrite nano-wires to be highly p-doped with an average of resistivity (0.18 ±0.09 Ω cm) and carried concentrations on the order of ($10^{21}$ $cm^{-3}$). Also, Thomas et al. [172] talked about thin film of $FsS_2$ pyrite and prepared it on (glass and glassy carbon) substrates by low pressure (LP) metal organic chemical vapor deposition (MOCVD), on other side, [173] reported a new and facile strategy for synthesizing ($FeS_2$ pyrite/nitrogen-doped graphene: $FeS_2$/N-G) composite, then, Qiu et al. in that paper showing improved electrochemical performance as an anode material for high-performance Lithium-ion batteries (LIBs).

### 3 - 4 - 2 Crystal structure and calculation method

The current calculations based on the density functional theory noticed (DFT), used the Korringa Kohn Rostoker (KKR) method [123-124], which facilitates us to take in consideration the randomness of the impurity elements in the calculation. We're going to use the AKAI KKR (MACHIKANEYAMA 2002V08) developed by H. Akai [122], using the (DFT) combined with the coherent potential approximation (CPA), including the (KKR-CPA) beside the parameterization of Vosko, Wilk and Nusair noticed: VWN [174]. Within the calculations, the scalar relativistic approximation was considered and the potential form is restricted to the muffin tin spheres are expanded with real harmonic up to $l = 2$ , while $l$ is the angular momentum at different sites.

In this study, the cubic structure of $FeS_2$ pyrite has been considered. This latter crystalline structure has a (face centred cubic) unit cell with one lattice parameter: (a= 5.416 Å) while u = 0.387 Å [175]; the space group of $FeS_2$ pyrite is *Pa-3*, having twelve atoms: four (Fe atoms) occupying the 4a Wyckoff positions (0,0,0); ( ½,0, ½); (0, ½,½); (½,½,0) and eight S occupying the 8c positions (u, u,u); (-u+½, -u, u+½); (-u, u+½, -u+½); (u+½, -u+½, -

u); (-u, -u, -u); (u+½, u, -u+½); (u, -u+½, u+½); (-u+½, u+½, u), figure 3.21. The valence states considered are Fe($3d^6 4s^2$) and S($3s^2 3p^4$). The (Fe atoms) form a (face centred cubic) array, while the (S atoms) are arranging in pairs across the cell centre and the midpoints of the cell edges; the iron is surrounded octahedrally by six sulfur atoms, while the sulfur is tetrahedrally surrounded by three Fe atoms and one S, while a pairs of sulfur atoms aligned at an angle to the axe directions.

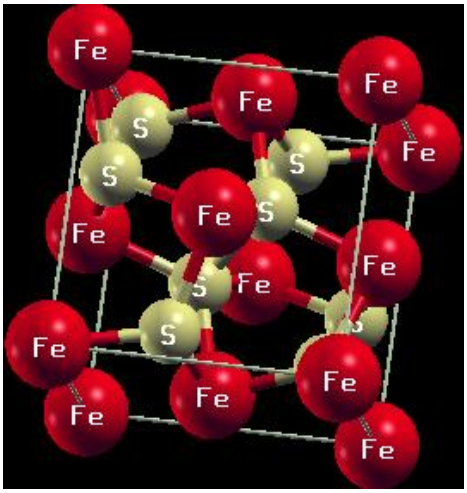


***Figure 3.21:*** *The unit cell of $FeS_2$ pyrite; the red balls correspond to Fe and the yellow balls to the S atoms.*

The electronic structure proprieties of V- and Cr- doped $FeS_2$ have been investigated to know the impact of the interaction 3d-3d on this system, then, show the most stable states; after that, we considered the same transition metals as co-doped $FeS_2$ pyrite in order to determinate the ferromagnetism behavior.

### 3 - 4 - 3 Results and discussion

Based on the used indicated method (KKR-CPA) included (VWN), figure 3.22 in relation to the pure $FeS_2$ pyrite, reveals that the valence band (VB) included two parts: the first one is indicated as high (VB) having an energy range (from -0.15 to -0.054 Ry) and the second one is the short (VB) in the follows range (from -0.57 to -0.15 Ry). $FeS_2$ pyrite without doped elements shows that the (DOS) of majority and minority states are symmetrical, that is to say in the pure case there is no magnetic evidence, and the sum of moment spin is 0 $\mu_B$, also the moment total is null in [176] as well as [166] confirms that $FeS_2$ pyrite (bulk) is nonmagnetic.

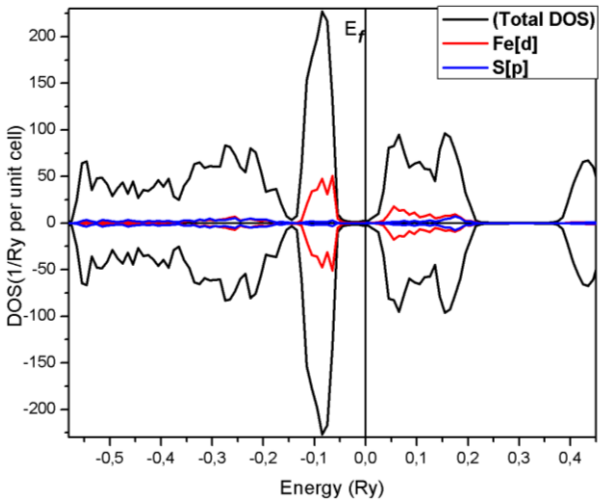


***Figure 3.22:*** *TDOS and PDOS of the pure $FeS_2$ pyrite related to the Fermi energy; the black, red and blue, respectively are the TDOS, Fe[d] and S[p] shells.*

For $Fe_{0.98}V_{0.02}S_2$, the stabilization of the magnetic state was evaluated within the estimation of the total energy difference indicated as (ΔE), that is to say the difference between ferromagnetic (FM) and the disordered local moment (DLM) states. For ferromagnetic state all moments of the magnetic atoms will aligned in the same direction and the other one is used conveniently to describe the DLM state at finite temperature, the (DLM) state is simulated by states in which half of the impurity ion spins point to the up direction and the rest points to the opposite direction; on the other side, Ziat et al. [147] introduced the same mechanism within the example of $Sn_{1-x}Mn^{\uparrow}_{0.5x}Mn^{\downarrow}_{0.5x}O_2$, therefore, in our case: the $Fe_{0.98}V^{\uparrow}_{0.01}V^{\downarrow}_{0.01}S_2$ system stands for the (DLM) state, and $Fe_{0.98}V^{\uparrow}_{0.02}S_2$ for the (FM) state in which all spins have one direction, therefore we will compare**(3.1)**, from table 3.11, we have ($\Delta E = -8{,}780*10^{-5}$) < 0 which means that the (DLM) more stable than (FM). Moreover, figure 3.23 depicts that is 3d electrons of V give rise to the highly localizing impurity state into the band gap and the hybridization with the valence band (VB) will be considered weakly; from table 3.11: as a fact the V provides the stability of (DLM) state which in agreement with figure 3.23, this figure shows an antiferromagnetic (AFM) stability belongs to super-exchange coupling type,on one hand, one of the two 3p orbital electrons of the anion $S_2^{2-}$ can be relocated to the half filled shell of $V^{2+}$ with three d electrons, the second p electron of sulfur would have its spin anti-parallel to the previous then would localized on the anion sulfur, on the other hand, for $V^{2+}$ the similar mechanism expects ferromagnetic coupling for $V^{2+}$ cations with less than half filed shells; also to explain the (DLM) state satiability in $Fe_{0.98}V_{0.02}S_2$ , itis worthy to say that the V impurity when (x = 0.02) has $d^3$electrons configuration due to the

substitution of $Fe^{2+}$ by $V^{2+}$ , as consequence, there is no carrier to mediate the (FM) stability, then, the predicted calculation magnetic state in $Fe_{0.98}V^{\uparrow}_{0.01}V^{\downarrow}_{0.01}S_2$ mechanism will standing for (DLM) state, figure 3.23 beside figure 3.21 shows the gap decreasing from the pure to $Fe_{0.98}V_{0.02}S_2$ system, which shifted (VB) to the Fermi level; for the reason that $V(3d^34S^2)$ has five electrons in $FeS_2$ which is doping in octahedral site of Fe, then becomes $V^{2+}(3d^3)$, the d orbital will be divided in two states: the first one is $e_g(d_{x-y}^{2\ 2})$ and second one is $t_{2g}(d_{xy}, d_{yz}, d_{xz})$, respectively high and low energy states, those two energy states due to the electron field created by the current six ligands resulting to octahedral crystal field, thus, $V^{2+}(3d^3)$ will having three V electrons that is filling the orbital:( $t_{2g}^{+}$); that is the reason why this orbital is into the left side of the Fermi level in the (VB) when the orbitals ( $t_{2g}^{-}$,$e_g^{+}$ and $e_g^{-}$) will be unfilled in the conduction band (CB) into the right side of the Fermi level, see figure 3.23.

| | $E_{ferro}$ (Ry) | $E_{Dlm}$ (Ry) | $E_{Dlm}$ -$E_{ferro}$ (Ry) | $T_c$ (K) | $M^T$ ($\mu_B$) | $M^{Fe}$ ($\mu_B$) | $M^V$ ($\mu_B$) | $M^{Cr}$ ($\mu_B$) | $M^S$ ($\mu_B$) |
|---|---|---|---|---|---|---|---|---|---|
| **$Fe_{0.98}V_{0.02}S_2$** | **-16479.340756** | **-16479.3408438** | **$-8.780*10^{-5}$** | **_____** | **-0.18487** | **-0.00815** | **-1.61516** | **____** | **-0.00031** |
| **$Fe_{0.95}Cr_{0.05}S_2$** | **-16442.1651405** | **-16442.164737** | **$4.035*10^{-4}$** | **849.80** | **0.30485** | **0.00394** | **_____** | **1.41733** | **-0.00157** |
| **$Fe_{0.93}V_{0.02}\ Cr_{0.05}S_2$** | **-16390.4483399** | **-16390.4479258** | **$4.141*10^{-4}$** | **622.95** | **-0.54098** | **-0.01463** | **-1.86889** | **-1.46416** | **0.00051** |

***Table 3.11:*** *Energies, moments and $T_c$ facts in $Fe_{0.98}V_{0.02}S_2$ ; $Fe_{0.95}Cr_{0.05}S_2$ and $Fe_{0.93}V_{0.02}Cr_{0.05}S_2$.*

The table 3.11 shows that is the total moment magnetic in $Fe_{0.98}V_{0.02}S_2$ is (-0.18487 $\mu_B$) the major contribution on the moment is from the V impurity when the $M^V$ around -1.61516 $\mu_B$, and this value is dominant front of the remaining $M^{Fe}$ and $M^S$, as result the V is a good element to provide more magnetic proprieties in $FeS_2$ pyrite.

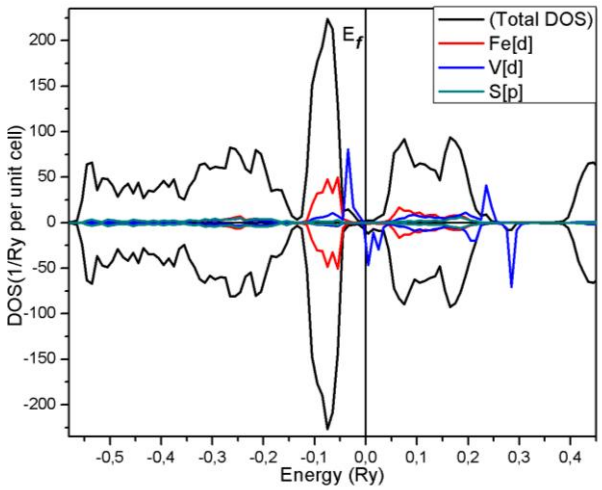


***Figure 3.23:*** *TDOS and PDOS of the $Fe_{0.98}V_{0.02}S_2$ related to the Fermi energy; the black, red, blue and green respectively are the TDOS, Fe[d], V[d] and S[p] shells.*

To explain and understanding the more stabilized ferromagnetism in $Fe_{0.95}Cr_{0.05}S_2$ hosted system, the (TDOS and PDOS) of this one has been plotted, figure 3.24, as we know the Cr($3d^5 4s^1$) has six valence electrons, and in $FeS_2$ pyrite system which is doped in octahedral site of iron, it becomes $Cr^{2+}$($3d^4$) with four electrons; as well, the 3d orbital is divided in two states $e_g$($d_{x-y}^2$) and $t_{2g}$($d_{xy}$, $d_{yz}$, $d_{xz}$), respectively high and low energy due to electronic field created by six ligands (octahedral crystal field), figure 3.24, the four electrons in Cr[3d] are occupied with 3 spins up in $t_{2g}$ state and 1 spin up in $e_g$ state, and the same figure of $Fe_{0.95}Cr_{0.05}S_2$ shows the ferromagnetic (FM) stability belongs to double-exchange coupling type, here it would been occurred a simultaneous transfer of electrons from $V^{2+}$ to $S^{2-}$ and from $S_2^{2-}$to $V^{2+}$, that effect involves (FM). In addition, the table 3.11 also confirm the that fact, when the ($\Delta E = 4{,}035*10^{-4}$ Ry)>0,which means that the (FM) more stable than (DLM) state; the value of ($\Delta E$) allowed to use the mean field approximation (MFA), thus, the Curie temperature ($T_c$) can be expected from the ($\Delta E$) between the (DLM and FM) states cited in table 3.11, then, $T_C$ is expressed in **(3.2)**, a result: Tc = 849.80 K, the obtained value of ($T_c$) shows that the Cr is a good 3d element to keep the $Fe_{0.95}Cr_{0.05}S_2$ in the (FM) state even in such as temperature. Moreover, in $Fe_{0.95}Cr_{0.05}S_2$ we found that the $M^{Cr}$ is 1.41733 $\mu_B$ whenthe total moment magnetic ($M^T$) around 0.30485 $\mu_B$, whereas $M^{Fe}$ and $M^S$ are neglected, that is to say the Cr is predicted doped $FeS_2$ pyrite for spintronic's applications, see table 3.11.

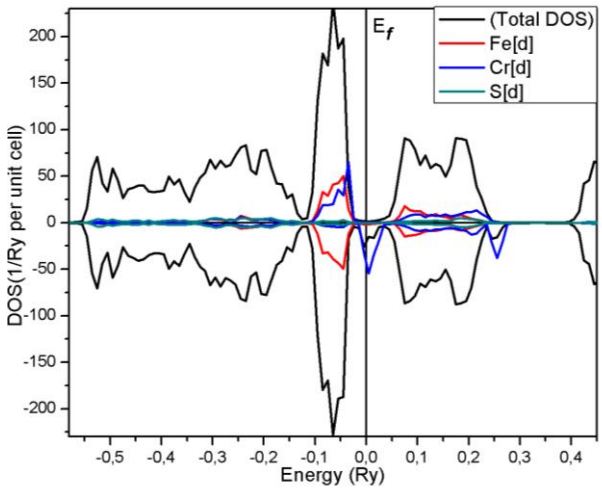


***Figure 3.24:*** *TDOS and PDOS of the $Fe_{0.95}Cr_{0.05}S_2$ related to the Fermi energy; the black, red, blue and green respectively are the TDOS, Fe[d], Cr[d] and S[p] shells.*

We have been noticed that $Fe_{0.98}V_{0.02}S_2$ found in (DLM) and $Fe_{0.95}Cr_{0.05}S_2$ in(FM) states, also from the figure 3.25, is worthy to mention that 3d-3d hybridization of transition metals (V and Cr) show that is believed to result a half metal proprieties for $Fe_{0.93}V_{0.02}Cr_{0.05}S_2$ system; the fact of introducing the (3d orbital of V and Cr) impurities will be in interacted with 3p orbital of S ,as a result forms the p-d orbital hybridization, so those 3d of impurities beside 3p state of S will producing an efficient magnetic moment field to line up the (V and Cr) magnetic moment as well as stabilize the half metallic (FM) state; furthermore, the double impurities in the $Fe_{0.93}V_{0.02}Cr_{0.05}S_2$ could optimize the hybridization instead the single doped case, then, the possibility to obtain the (sp3d) hybridization type could toke place in $Fe_{0.93}V_{0.02}Cr_{0.05}S_2$, as a consequence (one d beside one s and three p orbitals) of almost equivalent energy intermix to provide five identical and degenerate hybridization orbitals. The (TDOS) shown in figure 3.25 indicates a decrease in energy gap for the $Fe_{0.93}V_{0.02}Cr_{0.05}S_2$ to the pure $FeS_2$ since $Cr^{+2}(3d^4)$ has four net electrons in this current co-doped system, then, the variation in the gap is due to the (Coulomb correlation interaction) between ($S_2^{2-}$ and $Cr^{2+}$) anion and cation respectively; also the (FM) fact in $Fe_{0.93}V_{0.02}Cr_{0.05}S_2$ would be explain from the V[d] orbital state noted in figure 3.25, especially when ( $t_{2g}^{+})^3$ of (2% of V[d]) is moved at the top of valence band (TVB) to be nearest at the Fermi level since $Cr^{2+}$ having $[d^4=(e_g^+)^1,(t_{2g}^+)^3,(e_g^-)^0,(t_{2g}^-)^0]$, see (V[d] in figure 3.23 and figure 3.25). On other hand, the table 3.11 also confirms the existing (FM) state in $Fe_{0.93}V_{0.02}Cr_{0.05}S_2$ within ($\Delta E = 4.217*10^{-4}$ Ry)>0 since the computed energies of ($Fe_{0.93}V^{\uparrow}_{0.01}V^{\downarrow}_{0.01}Cr^{\uparrow}_{0.025}Cr^{\downarrow}_{0.025}S_2$ versus$Fe_{0.93}V^{\uparrow}_{0.02}Cr^{\uparrow}_{0.05}S_2$) indicated the (FM) state stability, as a result the Curie temperature

is calculated $T_c$= 622.95 K, as well, table 3.11 pointed up that the major contributed elements in the moments are (Cr and V) when $||M^{Cr}||+||M^{V}|| \gg ||M^{Fe}||+||M^{S}||$, that's why the total moment is -0.54098$\mu_B$ instead only -0.18487an b 0.30485 $\mu_B$, respectively in ($Fe_{0.98}V_{0.02}S_2$ and $Fe_{0.95}Cr_{0.05}S_2$) single's impurity; so the (V and Cr) co-doped $FeS_2$ pyrite would represented a ultimate 3d-3d elements regarding the high predicted ($T_c$) to keep (FM) stability beside its magnetism proprieties.

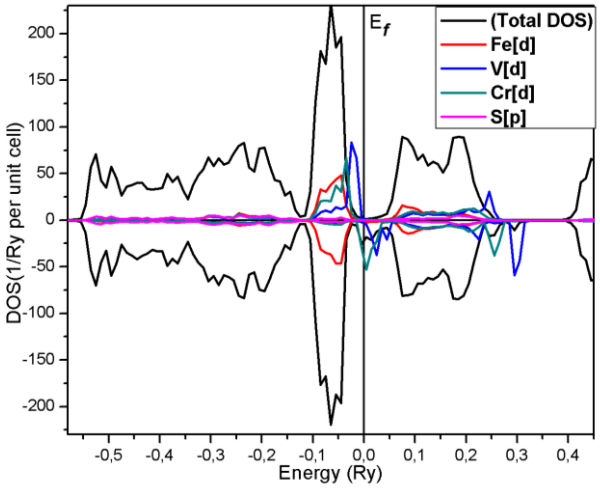


***Figure 3.25:*** *TDOS and PDOS of the $Fe_{0.93}V_{0.02}Cr_{0.05}S_2$ related to the Fermi energy; the black, red, blue, green and pink respectively are the TDOS, Fe[d], V[d], Cr[d] and S[p] shells.*

### 3 - 4 - 4 Conclusion

the ab-initio calculations based on (KKR-CPA) beside (VWM parameterization) utilized in $FeS_2$ pyrite for the follows hosted system, $Fe_{0.98}V_{0.02}S_2$,$Fe_{0.95}Cr_{0.05}S_2$ and$Fe_{0.93}V_{0.02}Cr_{0.05}S_2$ shows clearly the exiting of the (DLM) stability explained by (AFM) state belongs to super-exchange coupling type in $Fe_{0.93}V_{0.02}Cr_{0.05}S_2$ which has the V as major contributed on the moment, intended for $Fe_{0.95}Cr_{0.05}S_2$ system, the (FM) state is occur due to double-exchange coupling type, also the obtained ($T_c$) shows that the Cr is a good 3d element to keep the $Fe_{0.95}Cr_{0.05}S_2$ in the (FM) state, the third fact related to $Fe_{0.93}V_{0.02}Cr_{0.05}S_2$ is 3d-3d hybridization of transition metals (V and Cr) explains that is believed to result a half metal (FM) proprieties as well getting high moment and a predicted useful ($T_c$) making this material a good candidate in spintronic applications.

## 3 - 5 - The effect of nitrogen doping on magnetic and electronic properties of $Fe_{0.98}TM_{0.02}S_2$ pyrite (TM = V or Cr): ab-initio calculations

### 3 - 5 - 1 Introduction

Transition metal disulfides of $MS_2$ (M =Mn, Fe, Co, Ni Cu and Zn) with the pyrite structure forms a series of compounds with extremely interesting electrical and magnetic properties [64, 165, 177-178]. $CoS_2$ pyrite is an itinerate electron ferromagnet, $NiS_2$ pyrite is antiferromagnetic semiconductor, $CuS_2$ pyrite is metallic with a low temperature transition to a superconducting state and $ZnS_2$ pyrite is a wide-band-gap and nonmagnetic insulator, [165, 176, 178-180].

$FeS_2$ pyrite is composed of very abundant and nontoxic elements [181], with excellent electron mobility [182]. This material is receiving growing attention due to its promising potential for applications as an optoelectronic or photovoltaic material. It is required to have excellent environment compatibility, low production cost for photocurrent generation and high quantum efficiency [66-70]. Moreover, Gudelli et al. predicted that $FeS_2$ might have promising applications as a good thermoelectric material [183]. Naturally occurring pyrite is mainly found in three main crystal forms. The most common is the cubic form (100), the octahedral (111) and pyritohedral (210) surface crystals [164]. In addition, both n- and p-type conductivity were reported by Schlegel et al. [184].

In terms of p-type conductivity, many studies have been devoted. Rana et al. concluded that the electrical properties of $Cu_xFe_{1-x}S_2$ (CH-CFS) chalcopyrite and Cu-incorporated CFS (P-CFS) thin films were studied by Hall effect measurement employing the Van der Pauw method at room temperature, as a results, the measured electrical properties of CH-CFS and P-CFS thin films showed p-type conductivity [185]. According to Möller et al. [186], the Arsenic (As) is the most important element in establishing p-type conductivity of pyrite and arsenopyrite.

In addition, the synthetic $FeS_2$ pyrite thin films has been investigated via first-principles computations by Sun et al. [187], where the native and extrinsic ($O_s$ and $O_i$) point defects are computed. This study shown that under sufficiently oxidizing conditions, $O_s$ becoming the most dominant defect type and inducing p-type conductivity. Moreover, in the literature [188], the formation of $FeS_2$ pyrite thin films was performed using thermal sulfurization of dc

magnetron sputtered iron under different annealing temperatures and times. The single phase pyrite films were obtained after sulfurization in a sulfur and nitrogen atmosphere at 450°C for 1 h, the cubic phase of prepared pyrite films was p-type. That study found that the best Ohmic contact for the pyrite thin films, using inexpensive metals, was Ni.

Within the local density approximation (LDA) framework [92-93], many works have been devoted to investigate $FeS_2$ pyrite [177, 189-192]. In general, these studies concluded that this approximation is in reasonable agreement with the experimental data.

The purpose of this work is investigating the possibility to have the stability of FM for N-doped $Fe_{0.98}V_{0.02}S_2$ system as well as the effect of N on the magnetic properties of $Fe_{0.98}Cr_{0.02}S_2$.Since the ferromagnetic (FM) state connected to the half metal has been extensively searched due to its potential applications in spintronic field.

### 3 - 5 - 2 Calculation Model and Method

In the present work, the calculations are based on the density functional theory (DFT) using the Korringa-Kohn-Rostoker method [123-124] combined with the coherent potential approximation (CPA) and LDA [92-93], which is implemented in (MACHIKANEYAMA 2002V08) code [122]. The LDA is the simplest physical path to treat the exchange-correlation energy. Moreover, it is the most widely used in applied DFT and based on the homogeneous electron gas model (HEG) that has the same electron density at the point. In our calculations, the LDA is based on the parameterization given by Moruzzi, Janak and Williams (MJW)[127]. Here, the scalar relativistic approximation was considered and the potential form is restricted to the muffin tin spheres are expanded with real harmonic up to $l = 2$, while $l$ is the angular momentum at different sites.

The cubic structure of $FeS_2$ pyrite has been considered. The crystalline structure has a face-centered-cubic unit cell with one lattice parameter a= 5.416 Å with u=0.387 Å [175]. The space group of $FeS_2$ pyrite is *Pa-3* with twelve atoms, see figure 3.21. Four Fe atoms occupying the 4a Wyckoff positions (0,0,0); ( ½,0, ½); (0, ½,½); (½,½,0) and eight S occupying the 8c positions (u, u, u); (-u+½, -u, u+½); (-u, u+½, -u+½); (u+½, -u+½, -u); (-u, -u, -u); (u+½, u, -u+½); (u, -u+½, u+½); (-u+½, u+½, u). The valence states are Fe($3d^6 4s^2$) and S($3s^2 3p^4$). The Fe atoms form a face-centered-cubic array, where the S are arranging in pairs across the cell centre and the midpoints of the cell edges, the Fe is octahedrally surrounded by six S atoms, while the S is tetrahedrally surrounded by three Fe atoms and one S, and a pair of sulfur atoms aligned at an angle to the axe directions.

The electronic structure properties of $Fe_{0.98}TM_{0.02}S_{1.97}N_{0.03}$ pyrite has been investigated to know the effect of N doping on this system, then, understanding the magnetism stability.

### 3 - 5 - 3 Results and Discussion

The aim of this investigation is to study $FeS_2$ pyrite with double impurities (2p and 3d for $Fe_{0.98}TM_{0.02}S_{1.97}N_{0.03}$ system) rather than the regular single one. Since the double impurities in the current system can optimize the magnetic and electronic properties.

For $FeS_2$ without doped elements, the density of state (DOS) of majority and minority states are symmetrical, figure 3.26.That is to say, there is no magnetic evidence and the sum of moment spin is 0 $\mu_B$. Also, the total moment is null according to Bither et al. [176].

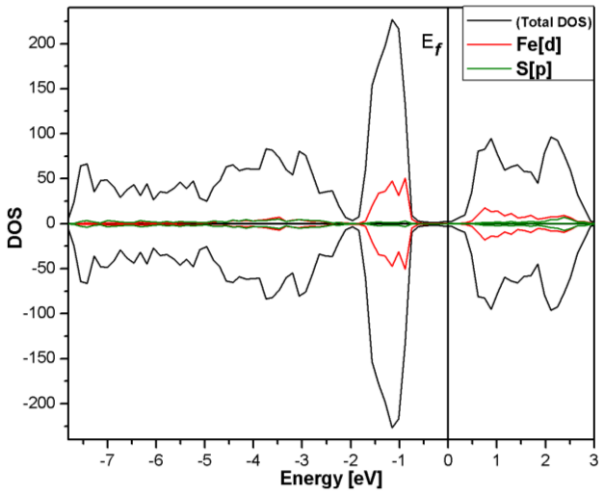


***Figure 3.26:*** *TDOS and PDOS of the pure $FeS_2$ pyrite related to the Fermi energy; the black, red and green, respectively are the TDOS, Fe[d] and S[p] shells.*

The experimentally band gap is around 0.95 eV [66], where the current study predicts 0.90 eV, which means that our obtained calculations in good agreement with the experimental data.

Before talking about $Fe_{0.98}TM_{0.02}S_{1.97}N_{0.03}$, it is worthy to indicate two main remarks, the first one is the calculated total moment of $FeS_{1.97}N_{0.03}$ is null, figure 3.27 (a), since the up and down of total (TDOS) is symmetrical. The second one is $FeS_{1.97}N_{0.03}$ shows the p-type conductivity where the valence band (VB) shifted to the Fermi level, see TDOS and partial (PDOS) related to N[p] , figure 3.27.

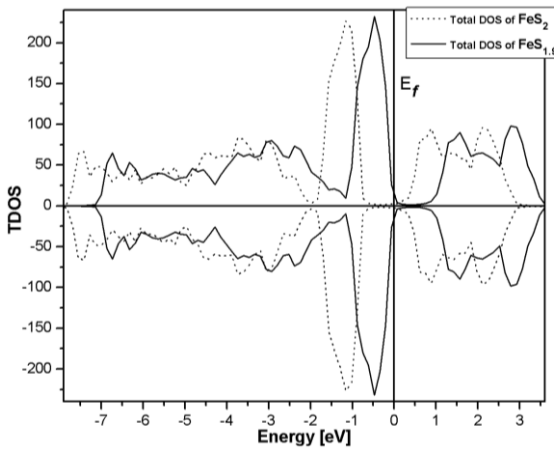


***Figure 3.27 (a):*** *the TDOS of $FeS_{1.97}N_{0.03}$ compared to$FeS_2$.*

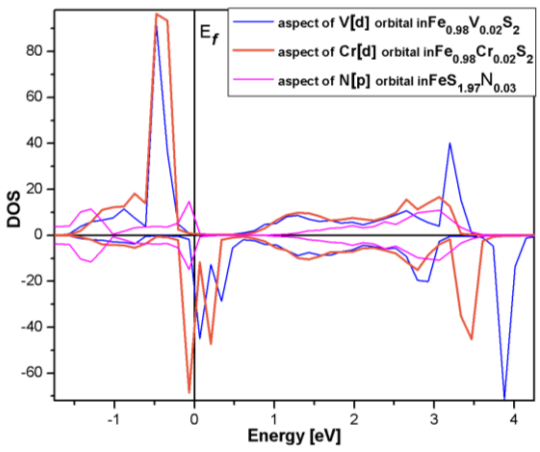


***Figure 3.27 (b):*** *The PDOS of N[p] associated to $FeS_{1.97}N_{0.03}$ compared to TM[d] of $Fe_{0.98}TM_{0.02}S_2$.*

Prior to discuss the $Fe_{0.98}V_{0.02}S_{1.97}N_{0.03}$ system, it is worthy to indicate that vanadium induces the disordered local moment (DLM) in $FeS_2$ [193]. In fact, the $Fe_{0.98}V_{0.02}S_2$ recognized an antiferromagnetic stability belongs to super-exchange coupling between two next to nearest neighbor $V^{2+}$cation through a $S_2^{2-}$ anion. One of two 3p orbital of sulfur electrons can be relocated to the half filled shell of $V^{2+}$ with 3 electrons of the orbital d, and the second 3p electrons of S would have its spin anti-parallel to the previous one. Also this mechanism is expecting the ferromagnetic coupling in $V^{2+}$ with less than half filed shells.

In $Fe_{0.98}V_{0.02}S_{1.97}N_{0.03}$, we observed the effect of N on the conversion of the $Fe_{0.98}V_{0.02}S_{1.97}N_{0.03}$ to FM state. To clarify this fact, the figure 3.28 associated to $Fe_{0.98}V_{0.02}S_2$ and $Fe_{0.98}V_{0.02}S_{1.97}N_{0.03}$ was plotted. Figure 3.28 (a) shows that the VB and conduction band (CB) are predominantly contributed by N[2p] and S[3p], and the top of VB (TVB) is mostly contributed by Fe[3d]. Moreover, the spin polarization around the Fermi level is mainly composed by V[3d] and the nearest neighboring N[2p] states. And $V(3d^34s^2)$ has 5 electrons which is doped in the octahedral site of iron, it becomes $V^{2+}(3d^3)$ when N impurity occurred. In addition, the d orbital is divided into two states $e_g(d_{x-y}^2, d_z^2)$ and $t_{2g}(d_{xy}, d_{yz}, d_{xz})$, which are the high and low energy states, respectively, due to electronic field created by 6 ligands corresponding to octahedral crystal field. In this case, $V^{2+}(3d^3)$ has 3 vanadium electrons, then, three electrons will fill the majority-spin related to $t_{2g}^+$ state . This state is situated slightly to the Fermi level and having the half metallic characteristic, figure 3.28 (b). The remaining majority-spin and minorities-spin related to ( $e_g^+$ , $t_{2g}^-$ and $t_{2g}^+$ states) will be

empty in the CB. Then, we predict the stability of FM in$Fe_{0.98}V_{0.02}S_{1.97}N_{0.03}$ system instead the presence of DLM in $Fe_{0.98}V_{0.02}S_2$.

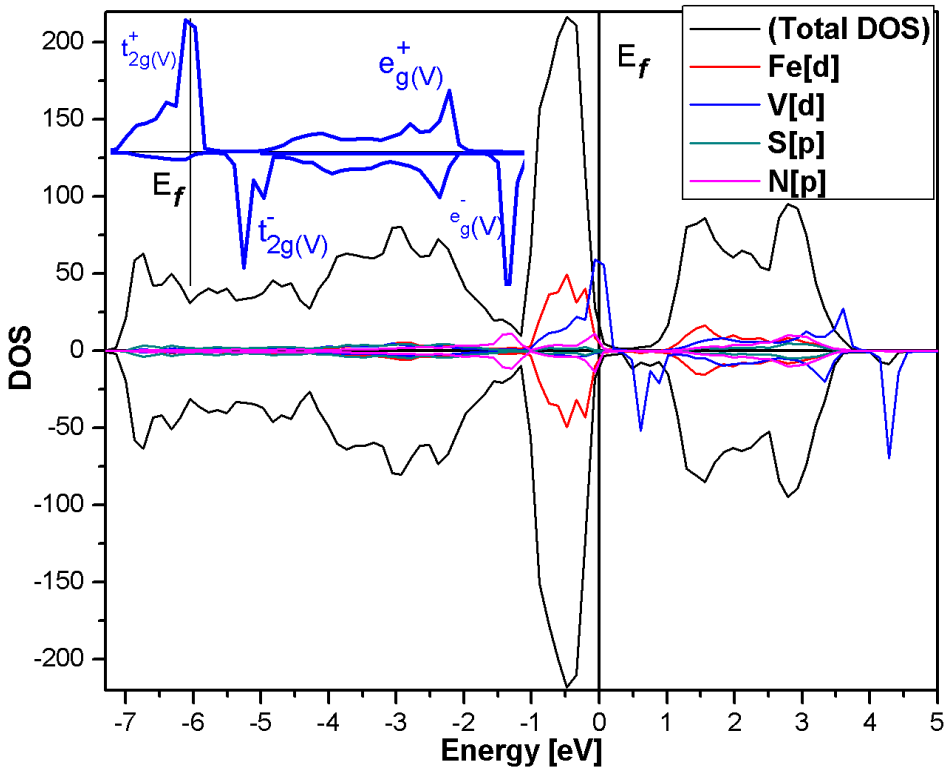


***Figure 3.28 (a):*** *TDOS and PDOS of $Fe_{0.98}V_{0.02}S_{1.97}N_{0.03}$ related to the Fermi energy; the black, red, blue, green and pink respectively are the TDOS, Fe[d], V[d], S[p] and N[p] shells.*

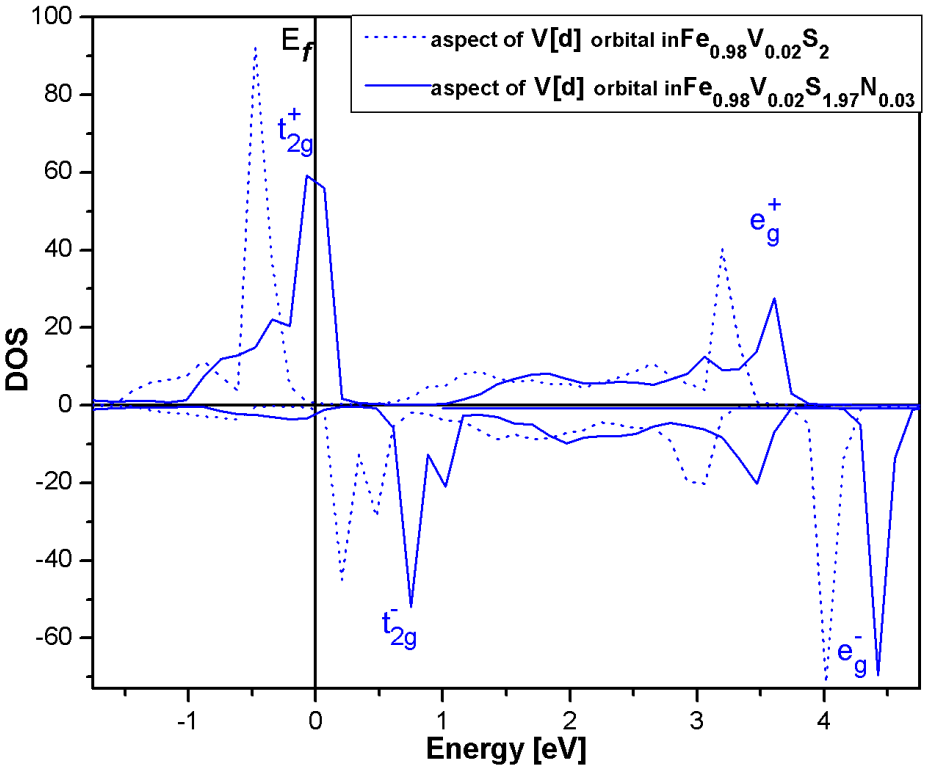


***Figure 3.28 (b):*** *V[d] state of $Fe_{0.98}V_{0.02}S_{1.97}N_{0.03}$ compared to $Fe_{0.98}V_{0.02}S_2$.*

To verify the FM stability, we can estimate the total energy difference (ΔE) between the DLM and FM states, **(3.1)**. $E_{DLM}$ and $E_{ferro}$ stand for the total energies of the DLM state and the FM state, respectively. The DLM state is simulated by state in which half of the impurity ion spins point to the up direction and the rest points to the opposite direction. Where $Fe_{0.98}V^{\uparrow}_{0.01}V^{\downarrow}_{0.01}S_{1.97}N^{\uparrow}_{0.015}N^{\downarrow}_{0.015}$ stands for the DLM state and $Fe_{0.98}V^{\uparrow}_{0.02}S_{1.97}N^{\uparrow}_{0.03}$ for the FM state in which all spins have the same direction. Our results depict that ΔE = 2.41> 0 meV. This fact confirms the stability of FM state. The Curie temperature ($T_C$) can be estimated within the mean-field approximation (MFA), see [194-195]. And its expression is noticed in **(3.2)**, see [147, 196-197]. For $Fe_{0.98}V_{0.02}S_{1.97}N_{0.03}$, the calculated $T_C$ is of 372.37 K. Hence, the N impurity could be a good candidate to stabilize the FM in $Fe_{0.98}V_{0.02}S_2$ for spintronic applications.

Moreover, for the comparison between $Fe_{0.98}V_{0.02}S_{1.97}N_{0.03}$ and $Fe_{0.98}V_{0.02}S_2$ systems, the total magnetic moment of unit cell is of -0.2182 and -0.1869 $\mu_B$, respectively. The partial moments are $M^V$ = -1.8912 and $M^N$ = -0.0005$\mu_B$ in $Fe_{0.98}V_{0.02}S_{1.97}N_{0.03}$, see table 3.12. Then, the major contribution to the moment comes from V, while $||M^V||>>||M^N||$. Moreover, the 3% of N doped

$Fe_{0.98}V_{0.02}S_2$ depicts the presence of p-type conductivity. Since figure 3.28 (b) shows a shifting of VB toward the Fermi level, see figure 3.26 compared to the TDOS of figure 3.28(a).

| | ΔE(meV) | $T_c$(K) | state | $M^T(\mu_B)$ | $M^{Fe}(\mu_B)$ | $M^{TM}(\mu_B)$ TM=V or Cr | $M^S(\mu_B)$ | $M^N(\mu_B)$ |
|---|---|---|---|---|---|---|---|---|
| $Fe_{0.98}V_{0.02}S_2$ | -1.27 | ---- | DLM | -0.1869 | -0.0081 | -1.6432 | -0.0003 | ---- |
| $Fe_{0.98}V_{0.02}S_{1.97}N_{0.03}$ | 2.41 | 372.37 | FM | -0.2182 | -0.0090 | -1.8912 | -0.0006 | -0.0005 |
| $Fe_{0.98}Cr_{0.02}S_2$ | 0.89 | 343.82 | FM | -0.0832 | 0.0001 | -1.09972 | 0.0011 | ---- |
| $Fe_{0.98}Cr_{0.02}S_{1.97}N_{0.03}$ | 2.66 | 412.16 | FM | -0.2350 | -0.0064 | -2.4642 | 0.0006 | -0.0026 |

***Table 3.12:*** *Energies and magnetic facts, comparison between $Fe_{0.98}TM_{0.02}S_2$ and $Fe_{0.98}TM_{0.02}S_{1.97}N_{0.03}$, with TM = V or Cr.*

Figure 3.29 was plotted to understand the ferromagnetism stability of $Fe_{0.98}Cr_{0.02}S_{1.97}N_{0.03}$ system. The effect of 3% of N-doped $Fe_{0.98}Cr_{0.02}S_2$ is clearly observed, because TDOS of figure 3.29 (a) shows a shifting of VB toward the Fermi level and verifying the presence of p-type conductivity, see figure 3.26 compared to the TDOS of figure 3.29 (a).

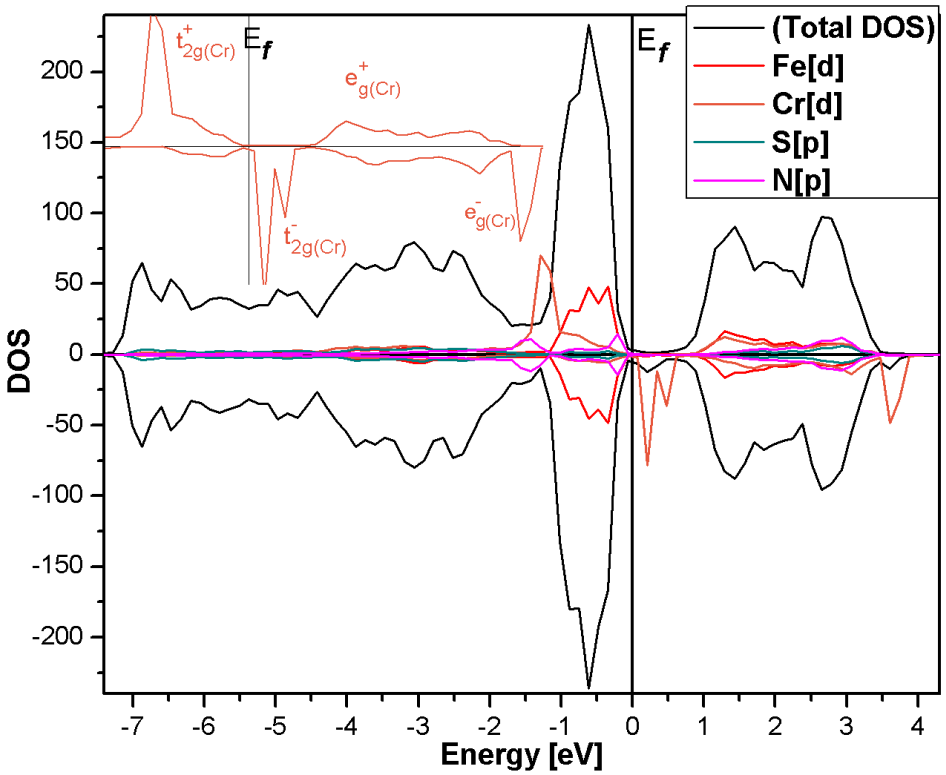


***Figure 3.29 (a):*** *TDOS and PDOS of $Fe_{0.98}Cr_{0.02}S_{1.97}N_{0.03}$ related to the Fermi energy; the black, red, orange, green and pink respectively are the TDOS, Fe[d], Cr[d], S[p] and N[p] shells.*

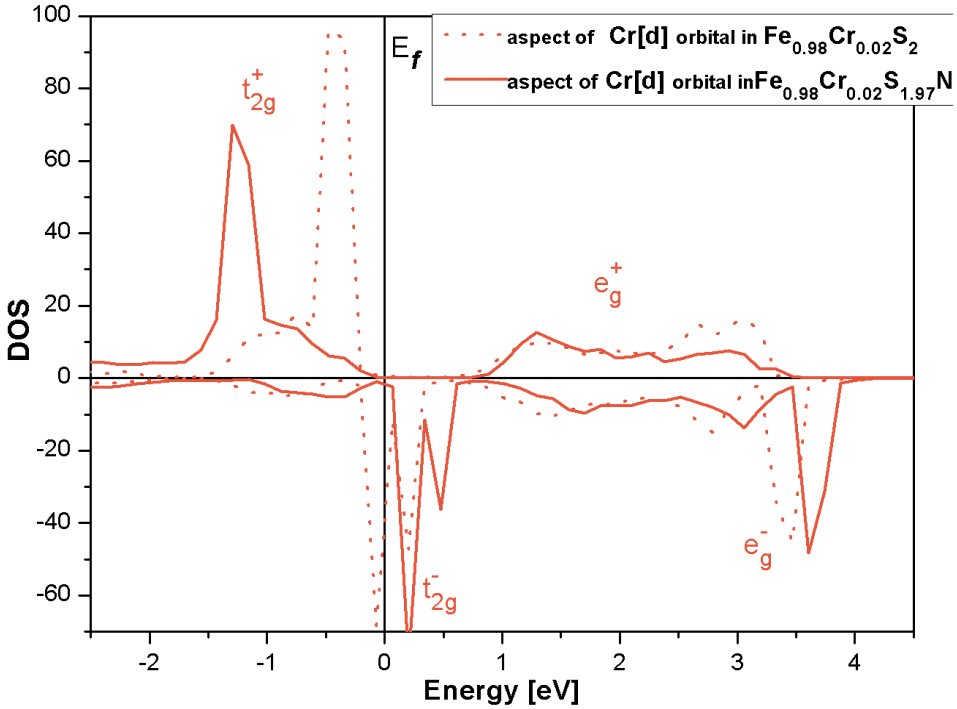


***Figure 3.29 (b):*** *Cr[d] state of $Fe_{0.98}Cr_{0.02}S_{1.97}N_{0.03}$ compared to$Fe_{0.98}Cr_{0.02}S_2$.*

Briefly, the $Fe_{0.98}Cr_{0.02}S_2$ system shows the FM stability belongs to double-exchange coupling type where an occurred simultaneous transfer of electrons is predicted from $Cr^{2+}$ to $S_2^{2-}$ and from $S_2^{2-}$to $Cr^{2+}$. In case of $Fe_{0.98}Cr_{0.02}S_{1.97}N_{0.03}$ , seefigure 3.29 (a),we can estimate that the 3% of N induced a hybridization between the Cr[3d] and N[2p] states in the following arrangement :{ (-1.75 to -0.5 eV) at the side of VB and (1.75 to 3 eV) at the side of CB}. So, this is an indirect coupling. Here, we have an enlargement and an amplitude reduction of the peak of the Cr[3d], see figure 3.29 (b). In addition, it is worthy to mention other remarks; the first one is that 3% of N augmented the total moment of unit cell to -0.2350 $\mu_B$ instead -0.0832 $\mu_B$, see table 3.12. The second one is related to the exchange splitting between $t_{2g}$ states and the crystal field splitting between $t_{2g}$ and $e_g$ states. Given that in $Fe_{0.98}Cr_{0.02}S_2$ the crystal field splitting between $e_g$ and $t_{2g}$ is larger than the exchange splitting between $t_{2g}^{+}$ and $t_{2g}^{-}$, but after introducing the 3% of N, the exchange splitting between $t_{2g}^{+}$ and $t_{2g}^{-}$ recognized an increase, see figure 3.29 (b). In addition, the ($\Delta E = 2.66 > 0$ meV) indicates the stability of FM state. Subsequently, the estimated $T_C$ is of 412.16 K, which can be very useful in the spintronic field.

### 3 - 5 - 4 Conclusion

To conclude this investigation, within DFT and LDA, the calculations of $Fe_{0.98}V_{0.02}S_{1.97}N_{0.03}$ pyrite predict the FM stability instead DLM, since $t_{2g}^{+}$state is around the Fermi level. The FM state connected to the half metal is searched due to its potential applications in spintronic.

For $Fe_{0.98}Cr_{0.02}S_{1.97}N_{0.03}$, the hybridization between the Cr[3d] and the N[2p] is occurred with an enlargement and an amplitude reduction of the peak of the Cr[3d]. As well as the p-type conductivity is observed. The total moment is augmented and the stability of FM is verified within MFA. The $T_C$ is augmented when 3% of N has been incorporated in the current systems.

# Bibliography

## List of Publication

### Publications connected to this thesis

---

**1** ***Magnetic and electronic properties of Cr-and Mn-doped $SnO_2$: ab initio calculations***

**Y. Ziat**, A. Benyoussef, A. El Kenz, Journal of Physics and Chemistry of Solids,75 (2014) 701-709.

---

**2** ***First-principles study of magnetic and electronic properties of fluorine-doped $Sn_{0.98}Mn_{0.02}O_2$ system***

**Y. Ziat**, A. Slassi, Z. Zarhri, M. Hammi, M. Houmad, A. Ait Raiss, Y. Sbai, S. Echihi, A. El Kenz, A. Benyoussef, Journal of Superconductivity and Novel Magnetism, 29 (2016) 2979-2985.

---

**3** ***Magnetic Properties of Co-(Os, Mn) Co-doped $ZrO_2$ Within GGA and mBJ Approaches***

**Y. Ziat**, M. Boujnah, A. Benyoussef, A. El Kenz, Journal of Superconductivity and Novel Magnetism, 28 (2015) 3397-3403.

---

**4** ***The Magnetism Behavior of $Fe_{0.93}V_{0.02}Cr_{0.05}S_2$ Pyrite Within Ab Initio Calculation***

**Y. Ziat**, Z. Zarhri, A. Slassi, A. Benyoussef, A. El Kenz.. Journal of Superconductivity and Novel Magnetism, 28 (2015) 3645-3649.

---

**5** ***The effect of nitrogen doping on magnetic and electronic properties of $Fe_{0.98}TM_{0.02}S_2$ pyrite (TM= V or Cr): Ab-initio calculations***

**Y. Ziat**, Z. Zarhri, M. Hammi, A. Slassi, S. Echihi, A. El Kenz, A. Benyoussef, Solid State Communications, 237(2016) 5-9.

---

**Other publications**

| | |
|---|---|
| **1** | *Investigation of electronic and magnetic properties of FeS: First principle and Monte Carlo simulations*<br>R. Bouachraoui, **Y. Ziat**, L.Bahmad, N.Tahiri, Solid State Communications, 274 (2018) 46-50 |
| **2** | *Fabrication and characterization of novel transparent conducting oxide N-CNT doped ZnO for photovoltaic applications*<br>A. Benyounes, N. Abbas, M. Hammi, **Y. Ziat**, A. Slassi, N. Zahra, Applied Physics A, 124 (2018) 90 |
| **3** | *Ferromagnetism induced by double impurities Mn and Cr in 3C–SiC*<br>M. Houmad, Z. Zarhri, **Y. Ziat**, Y. Benhouria, A. Benyoussef, A. El Kenz, Chinese Journal of Physics, 56 (2018) 404-410 |
| **4** | *Effect of halogens doping on transparent conducting properties of SnO 2 rutile: an ab initio investigation*<br>A. Slassi, M. Hammi, Z. Oumekloul, A. Nid-bahami, M. Arejdal, **Y. Ziat**, O. El Rhazouani, Optical and Quantum Electronics, 50 (2018) 8. |
| **5** | *Monte Carlo simulation for calculating the exchange couplings in $Ca_2CrNO_6$(**N**= Mo, Re) double perovskites*<br>O. El Rhazouani, **Y. Ziat**, A. Benyoussef, Modern Electronic Materials, 3 (2017) 99-103 |
| **6** | *Exchange couplings calculation in $Sr_2CrNO_6$ (N= Os, Ir) Double Perovskites: Monte Carlo simulation*<br>O. El Rhazouani, A. Slassi, **Y. Ziat**, A. Benyoussef, Current Applied Physics, 17 (2017) 951-956. |
| **7** | *Exchange couplings calculation in the Double Perovskite $Sr_2CrWO_6$*<br>O. El Rhazouani, A. Slassi, **Y. Ziat**, A. Benyoussef, Physica A: Statistical Mechanics |

and its Applications, 476 (2017) 38-42.

**8** *Magnetocaloric effect in $Sr_2CrIrO_6$ double perovskite: Monte Carlo simulation*

O. El Rhazouani, A. Slassi, **Y. Ziat**, A. Benyoussef, Journal of Physics and Chemistry of Solids, 104 (2017) 32-35.

**9** *Competing exchange couplings in $Sr_2CrReO_6$ Double Perovskite*

O. El Rhazouani, A. Slassi, **Y. Ziat**, A. Benyoussef, Physics Letters A, 381 (2017) 1177-1180.

**10** *Effect of Fe doping on the electronic structure, optical and electrical properties of ZnO compound: Ab initio insights*

M. Hammi, **Y. Ziat**, A. Ait Raiss, M. Arejdal, Y. Sbai, O. El Rhazouani, A. Slassi, Optik-International Journal for Light and Electron Optics, 131 (2017) 399-405.

**11** *First-principles investigation of the electronic and optical properties of Al-doped $FeS_2$ pyrite for photovoltaic applications*

**Y. Ziat**, A. Abbassi, A. Slassi, M. Hammi, A. Ait Raiss,O. El Rhazouani,M. Houmad,S. Echihi, A. El Kenz, Optical and Quantum Electronics, 48 (2016) 511.

**12** *Titanium atoms dimerization phenomenon and magnetic properties of titanium-antisite ($Ti_O$) and chromium doped rutile $TiO_2$, ab-initio calculation*

Z. Zarhri, **Y. Ziat**, O. El Rhazouani, A. Benyoussef, A. El kenz,. Journal of Physics and Chemistry of Solids, 94 (2016) 12-16.

**13** *Ab-initio study of magnetism behavior in $TiO_2$ semiconductor with structural defects*

Z. Zarhri, M. Houmad, **Y. Ziat**, O. El Rhazouani, A. Slassi, A. Benyoussef, A. El Kenz, Journal of Magnetism and Magnetic Materials, 406 (2016) 212-216.

**14** *Ab initio investigations of the F-doped ZnO transparent conducting oxide*

A. Slassi, **Y. Ziat**, Z. Zarhri, M. Abdellaoui, A. F. Lamrani, Physica Scripta, 90 (2015) 085801.

**15** *Ab initio study on the electronic, optical and electrical properties of Ti-, Sn-and Zr-doped ZnO*

A. Slassi, N. Lakouari, **Y. Ziat**, Z. Zarhri, A. F. Lamrani, E. K. Hlil, A. Benyoussef, Solid State Communications, 218 (2015) 45-48.

# References


[1] D. L. Dreifus, R. M, Kolbas, R. L. Harper, J. R. Tassitino, S. Hwang, J. F. Schetzina, Appl. Phys. Lett, 53 (1988) 1279-1281.

[2] N. Teraguchi, A. Suzuki, Y. Nanishi, Y. K. Zhou, M. Hashimoto, H. Asahi, Solid State Commun, 122 (2002) 651-653.

[3] X. C. Liu, E. W Shi, Z. Z. Chen, H. W. Zhang, B. Xiao, L. X. Song, Appl. Phys. Lett, 88 (2006) 252503.

[4] T. Minami, MRS Bull, 25 (2000) 38.

[5] T. Fukumura, Y. Yamada, H. Toyosaki, T. Hasegawa, H. Koinuma, M. Kawasaki, Appl. Surf. Sci, 223 (2004) 62-67.

[6] T. Mizokawa, T. Nambu, A. Fujimori, T. Fukumura, M. Kawasaki, Phys. Rev. B65 (2002) 085209.

[7] Wikimedia commons, http ://commons.wikimedia.org/

[8] L. Chang, M. Wang, L. Liu, S. Luo, P. Xiao, arXiv preprint arXiv (2014) 1412.7691.

[9] http://simple.wikipedia.org/wiki/Giant_magnetoresistance

[10] E. Y. Tsymbal, D. Pettifor, Solid State Physics, 56 (2001) 113–237.

[11] M. Jullière, Phys. Lett. A, 54 (1975) 225

[12] P. M. Tedrow, R. Meservey, Phys. Rev. Lett, 26 (1971) 192-195

[13] J. S. Moodera, L. R. Kinder, T. M. Wong, R. Meservey, Phys. Rev. Lett, 74 (1995) 3273-3276

[14] W. J. Gallagher, S. P. P. Parkin, "Development of the magnetic tunnel junction MRAM

[15] S. Datta, B. Das, Appl. Phys. Lett, 56 (1990) 665-667

[16] Y. A. Bychkov, E. I. Rashba, J. Phys. C, 17 (1984) 6039

[17] G. Lommer, F. Malcher, U. Rossler, Phys. Rev. Lett, 60 (1988) 728–731

[18] G. Engels, J. Lange, T. Schäpers, H. Lüth, Phys. Rev. B, 55 (1997) R1958–R1961

[19] J. P. Heida, B. J. van Wees, J. J. Kuipers, T. M. Klapwijk, G. Borghs , Phys. Rev. B, 57 (1998) 11911–11914]

[20] T. Matsuyama, R. Kürsten, C. Meißner, and U. Merkt, Phys. Rev. B, 61(2000)15588–15591

[21] J. Nitta, T. Akazaki, H. Takayanagi, T. Enoki, Phys. Rev. Lett, 78 (1997)1335–1338

[22] T. Schäpers, G. Engels, J. Lange, T. Klocke, M. Hollfelder, H. Lüth, J. Appl. Phys, 83(1998) 4324–4333

[23] J. Wunderlich, B. G. Park, A. C. Irvine, L. P. Zârbo, E. Rozkotová, P. Nemec, V. Novak, J. Sinova, T. Jungwirth, Science, 330 (2010) 1801–1804

[24] Nan. Zheng, Introduction to Dilute Magnetic Semiconductors, Solid Sate II, Instructor (2008)

[25] H. Munekata, H. Ohno, S. von Molnar, A. Segmüller, L. L. Chang, L. Esaki, Phys. Rev. Lett, 63 (1989) 1849.

[26] H. Ohno, A. Shen, F. Matsukura, A. Oiwa, A. Endo, S. Katsumoto,Y. Iye, Appl. Phys. Lett. 69 (1996) 363-365

[27] T. Jungwirth, J. Sinova, J. Mašek, J. Kucera, A. H. MacDonald, Rev. Mod. Phys. 78 (2006) 809.

[28] T. Fukumura, Z. Jin, A. Ohtomo, H. Koinuma, M. Kawasaki, J. Appl. Phys. 75 (1999) 3366.

[29] Y. Matsumoto, R. Takahashi, M. Murakami, T. Koida, X. J. Fan, T. Hasegawa, T. Fukumura, M. Kawasaki, S.-Y. Koshihara and H. Koinuma, Jpn. J. Appl. Phys. 40 (2001) L1204

[30] Y. Matsumoto, M. Murakami, T. Shono, T. Hasegawa, T. Fukumura, M. Kawasaki, P. Ahmet, T. Chikyow, S. Y. Koshihara, H. Koinuma, Science 291 (2001) 854-856

[31] S. B. Ogale, R. J. Choudhary, J. P. Buban, S. E. Lofland, S. R. Shinde, S. N. Kale, V. N. Kulkarni, J. Higgins, C. Lanci, J. R. Simpson, N. D. Browning, S. Das Sarma, H. D. Drew, R. L. Greene, T. Venkatesan, Phys. Rev. Lett. 91 (2003) 077205

[32] J. Philip, N. Theodoropolou, G. Berera, J. S. Moodera, B. Satpati, Appl. Phys. Lett. 85 (2004) 777

[33] S. N. Kale, S. B. Ogale, S. R. Shinde, M. Sahasrabuddhe, V. N. Kulkarni, R. L. Greene T. Venkatesan, Appl. Phys. Lett. 82 (2003) 2100-2102

[34] K. Ueda, H. Tabata, T. Kawai , Appl. Phys. Lett. 79 (2001) 988

[35] S. Ostanin, A. Ernst, L. M. Sandratskii, P. Bruno, M. Dane, I. D. Hughes, J. B. Saunton,

W. Hergert, I. Mertig, J. Kudronvsky. Phys. Rev. Lett, 98 (2007) 016101

[36] M. Boujnah, H. Zaari, H. Labrim, A.Benyoussef, A. El Kenz, O. Mounkachi, J. Appl. Phys, 115 (2014) 123909

[37] T. Miyadai, S. Ohtani, Y. Tazuke,J. Magn. Magn. Mater, 70 (1987) 201-202.

[38] K. Ramesha, R. Seshadri, C Ederer, T. He, M. A. Subramanian, Phys. Rev. B, 70 (2004), 214409.

[39] J. M. D. Coey, A.P. Douvalis, C.B. Fitzgerald, and M. Venkatesan. Appl. Phys. Lett., 84 (2004) 1332-1334

[40] S. R. Shinde, S. B. Ogale, S. Das Sarma, J. R. Simpson, H. D. Drew, S. E. Lofland,

C. Lanci, J. P. Buban, J. Higgins R. P. Sharma N. D. Browning, V. N. Kulkarni, R. L. Greene, T. Venkatesan. Phys. Rev. B, 67 (2003) 115211

[41] N. H. Hong, J. Sakai, W. Prellier, A. Hassini, A. Ruyter, F. Gervais. Phys. Rev. Lett.,

21 (1968) 1190

[42] Z. Wang, W. Wang, J. Tang, L. D. Tung, L. Spinu, and W. Zhou. Appl. Phys. Lett., 83 (2003) 518

[43] J. Philip, A. Punnoose, B. I. Kim, K. M. Reddy, S. Layne, J. O. Holmes, B. Satpati,

P. R. LeClair, T. S. Santos, and J. S. Moodera. Nature Mater, 5 (2006) 298

[44] Y. K. Yoo, Q. Xue, H.-C. Lee, S. Cheng, X.-D. Xiang, G. F. Dionne, S. Xu, J. He, Y. S. Chu, S. D. Preite, S. E. Lofland, and Ichiro Takeuchi. Appl. Phys. Lett., 86 (2005) 052503

[45] J. M. D. Coey, J. Appl. Phys, 97 (2005) 10D313

[46] B. Sathyaseelan, K. Senthilnathan,T. Alagesan, R. Jayavel, K. Sivakumar, Mater. Chem. Phys., 124 (2010) 1046

[47] B. Kamp, R. Merkle, R. Lauck, J. Maier, J. Solid State Chem., 178 (2005) 3027–3039

[48] M. Batzill, U. Diebold, Prog. Surf. Sci., 79 (2005) 47

[49] L. M. Fang, X. T. Zu, Z. J. Li, S. Zhu, C. M. Liu, W. L. Zhou, L. M. Wang, J. AlloysCompd, 454 (2008) 261-267

[50] J. Xu, S. Huang, Z. Wang, Solid State Commun, 149 (2009) 527-531

[51] Y. Lu, P. J. Wangn, C. W. Zhang, X. Y. Feng, L. Jiang, G. L. Zhang, Physica B Condens Matter, 406 (2011) 3137–3138

[52] W. Wei, Y. Dai, M. Guo, Z. Zhang, B. Huang, J. Solid State Chem, 183 (2010) 3073

[53] Z. Liang , Y. Ding , J. Jia , C. Fan , P. Han, Physica B Condens Matter, 406 (2011) 2266

[54] F. Bouamra, A. Boumeddiene, M. Rérat, H. Belkhir, Appl. Surf. Sci, 269 (2013) 41-44

[55] C. Zhang, P. wang, F. Li, Solid State Sci, 13 (2011) 1608-1611

[56] V. Bilovol, C. Herme, S. Jacobo, A.F. Cabrera, Mater Chem Phys, 135(2012) 335

[57] C. E. R. Torres, A. F. Cabrera, F. H. Sánchez, Physica B Condens Matter, 389 (2007) 176-177

[58] S. A. Steiner, T. F. Baumann, B. C. Bayer, R. Blume, M. A. Worsley, W. J. Moberly Chan, E. L. Shaw, R. Schlogl, A. J. Hart, S. Hofmann, B. L. Wardle. J. Am. Chem. Soc., 131 (2009) 12144

[59] X. Song, M. Xie, X. Hao, F. Jia, S. An, J. Alloys Compd. 497,

(2010) L5

[60] E. Ryshkewitz, D. W. Richardson, Physical Chemistry and Technology. General Ceramics, Haskell (1985)

[61] M. Liu, C. He, J. Wang, W. Wang, Z. Wang, J. Alloys Compd. 502 (2010) 319

[62] J. Ding, J. Liu, W. M. Guo, J. Alloys Compd, 489, (2009) 286]

[63] D. G. Lamas, M. F. Bianchetti, M. D. Cabezas, N. E. Walsoe de Reca, J. Alloys Compd, 495 (2010) 548

[64] C. I. Pearce, R. A. D. Pattrick and D. J. Vaughan, Reviews in Mineralogy and Geochemistry, 61(2006) 127-2006

[65] S. Nakamura, A. Yamamoto, Solar Energy Mater. Solar Cells, 65 (2001) 79

[66] A. Ennaoui, H. Tributsch, Solar Cells, 13 (1984) 197

[67] A. Ennaoui, S. Fiechter, H. Goslowsky, H. Tributsch, J. Electrochem. Soc., 132 (1985) 1579

[68] A. Ennaoui, S. Fiechter, W. Jaegermann, H. Tributsch, J. Electrochem.Soc., 133 (1986) 97

[69] A. Ennaoui, S. Fiechter, C. Pettenkofer, N. Alonso-Vante, K. Büker, M. Bronold, C. Höpfner, H. Tributsch, Solar Energy Mater. Solar Cells, 29 (1993) 289.

[70] I. J. Ferrer, D.M. Nevskaia, C. de las Heras, C. Sánchez, Solid State Commun., 74 (1990) 913

[71] T. Dietl, H. Ohno, F. Matsukura, J. Cibert, D. Ferrand, Science, 287 (2000) 1019-1022

[72] O. Mounkachi, A. Benyoussef, A. El Kenz, E. H. Saidi, E. K. Hlil, Physica A, 388 (2009) 3433-3441

[73] K. Sato, P. H. Dederichs, H. Katayama-Yoshida, J. Kudrnovsky. J. Phys: Condens.

Matter, 16 (2004) S5491

[74] https://en.wikipedia.org/wiki/Double-exchange_mechanism

[75] P. G. De Gennes, Phys. Rev, 118 (1960) 141

[76] G. H. Jonker, J. H. van Santen. Physica, 16 (1950) 337

[77] R. Skomski, J. Zhou, J. Zhang, D. J. Sellmyer , J. Appl. Phys. 99 (2006), 08D504.1-08D504.3

[78] J. B. Goodenough, A. Wold, R. J. Arnot, N. Menyuk, Phys. Rev, 124 (1961) 373

[79] https://en.wikipedia.org/wiki/Superexchange

[80] F. Herlach, Physica B, 319 (2002) 321-329

[81] A. Visintin, "Historical Notes." Differential Models of Hysteresis. Springer Berlin Heidelberg (1994) 9-11

[82] H. N. Russell, F. A. Saunders, J. Astrophys, 61 (1925) 38]

[83] W. Heisenberg. Z. Phys,, 49 (1928) 619-636

[84] M. Born, J. R. Oppenheimer, Annalen der Physik, 389 (1927) 457–484

[85] P. Baranek, G. Pinarello, C. Pisani , R. Dovesi, Phys. Chem. Chem. Phys, 2 (2000) 3893-3901

[86] S. Casassa, A. Ferrari, M. Busso, and C. Pisani. J. Phys. Chem. B, 106 (2002) 12978-12985

[87] A. Szabo, N. S. Ostlund, Modern Quantum Chemistry, 1982

[88] P. Pulay, S. Saebø, Theor. Chim. Acta, 69 (1986), 357-368

[89] G. E. Scuseria, Chem. Phys. Lett, 176 (1991) 27-35

[90] L. H. Thomas. Math. Proc. Cambridge Philos. Soc, 23 (1927) 542

[91] E. Fermi. Z. Phys, 48 (1928) 73-79

[92] P. Hohenberg, W. Kohn. Phys. Rev, 136 (1964) B864

[93] W. Kohn , L. J. Sham, Phys. Rev, 140 (1965) A1133

[94] P. A. M. Dirac. Proc. Cambridge Phil. Roy. Soc., 26 (1930) 376

[95] W. Kohn, Rev. Mod. Phys, 71 (1999) 1253

[96] C. S. Wang, B. M. Klein, H. Krakauer, Phys. Rev. Lett, 54 (1985) 1852

[97] T. C. Leung, C. T. Chan, B. N. Harmon, Phys. Rev. B, 44 (1991) 2923

[98] J. P. Perdew, K. Burke, M. Ernzerhof, Phys. Rev. Lett, 77 (1996) 3865

[99] A. D. Becke, Phys. Rev. A, 38 (1988) 3098

[100] F. Tran, P. Blaha. Phys. Rev. Lett, 102 (2009) 226401

[101] A. D. Becke, E. R. Johnson, J. Chem. Phys, 124 (2006) 221101

[102] A. D. Becke and M. R. Roussel. Phys. Rev. A, 39 (1989) 3761

[103] j. Korringa, Physica, 13 (1947) 392-400

[104] W. Kohn, N. Rostoker, Phys. Rev 94 (1954) 1111

[105] K. Inoue, K. Ohtaka, eds. Photonic crystals: physics, fabrication and applications. Vol. 94. Springer, 2013

[106] J. S. Galsin, Impurity scattering in metallic alloys. Springer Science & Business Media, 2012

[107] Y. Kumashiro, Electric refractory materials. CRC Press, 2000

[108] A. Meike, A. Gonis, P. E. Turchi, K. Rajan (2000). Properties of Complex Inorganic Solids 2. Springer. p. 213

[109] S. Blügel, G. Bihlmayer, NIC series, 31 (2006) 85–129 or http://juser.fz-juelich.de/record/50026/files/FZJ-2014-02213.pdf

[110] J. C. Slater, Phys. Rev, 81 (1951) 385

[111] O. K. Andersen., Phys. Rev. B, 12 (1975) 3060

[112] D. D. Koelling, G. O. Arbman, J. Phys. F: Metal Phys, 5 (1975) 2041

[113] E. Sjöstedt, L. Nordström, and D. J. Singh. Solid State Commun, 114 (2000) 15–20

[114] P. Blaha, K. Schwarz, G. Madsen, D. Kvasnicka, and J. Luitz, WIEN2k, Augmented Plane Wave + Local Orbitals Program for Calculating Crystal Properties, Vienna, Austria, 2001. See also: http://www.wien2k.at

[115] S. Chattopadhyay, S. K. Neogi, A. Sarkar, M. D. Mukadam, S. M. Yusuf, A. Banerjee, S. Bandyopadhyay, J. Magn. Magn. Mater, 323 ( 2011) 363–368

[116] A. Punnoose, M. H. Engelhard, J. Hays, Solid State Commun, 139 (2006) 434

[117] C.E. Rodrıguez Torres, L. Errico, F. Golmar, A.M. Mudarra Navarro, A.F. Cabrera, S. Duhalde, F.H. Sanchez, M. Weissmann, J. Magn. Magn. Mater 316 (2007) 219

[118] C. B. Fitzgerald, M. Venkatesan, A. P. Douvalis, S. Huber, and J. M. D. Coey, J. Appl. Phys, 95 (2004) 7390-7391

[119] N. H. Hong, J. Magn. Magn. Mater, 303 (2006) 338

[120] X.L. Wang, Z.X. Dai, Z. Zeng, J. Phys. Condens. Matter, 20 (2008) 045214

[121] M. Toyoda, H. Akai , K. Sato and H. Katayama-Yoshida, Physica B: Condens. Matter, 376 (2006) 647-650

[122] MACHIKANEYAMA2002v08 :H. Akai , Department of Physics, Graduate School of Science ,Osaka University, Machikaneyama 1-1,Toyonaka 560-0043, Japan, akai@phys.sci.osaka-u.ac.jp

[123] Á. Nagy, Physics Reports 298 (1998) 1-79.

[124] H. Akai, J. Phys. Condens. Matter, 1 (1989) 8045

[125] J. P. Perdew, J. A.Chevary, S. H. Vosko, K. A. Jackson, M. R. Pederson, D. J. Singh, C. Fiolhais, Phys. Rev. B 46 (1992) 6671

[126] Van An Dinh, Kazunori Sato, Hiroshi Katayama-Yoshida, Solid State Commun, 136 (2005) 2

[127] V. L. Mouruzzi, J. F. Janak and A. R. Williams Properties of Metals. Pergramon, New York (1998)

[128] A. A. Bolzan, C. Fong, B. J. Kennedy and C. J. Howard, Acta Crystallogr. B 53 (1997) 373

[129] J. P. Perdew, R. G. Parr, M. Levy and J. L. Balduz, Phys. Rev. Lett, 49 (1982) 1691.

[130] L. J. Sham and M. Sclüter, Phys. Rev. Lett, 51 (1983) 1888.

[131] A. Fakhim Lamrani, M. Belaiche, A. Benyoussef, A.E.L. Kenz, E.H. Saidi, J. Magn. Magn. Mater, 322 (2010) 454–458

[132] N. H. Hong, J. Sakai, W. Prellier, A. Hassini, J. Phys: Condens. Matter 17 (2005) 1697–1702

[133] D. Canteli, I. Torres, J. J. García-Ballesteros, J. Cárabe, C. Molpeceres, J. J. Gandía, Appl Surf Sci, 271 (2013) 223

[134] H. Sefardjella, B. Boudjema, A. Kabir and G. Schmerber, J. Phys. Chem. Solids, 74 (2013) 1686

[135] B. Thangaraju, Thin Solid Films, 402 (2002) 71

[136] F.A. Garcés, N. Budini, R.R. Koropecki, R.D. Arce, Thin Solid Films, 531 (2013) 172

[137] G. Rahman, V. M. Garcia-Suarez, S. C. Hong, Phys. Rev. B 78 (2008) 184404

[138] Z. M. Jarzebski, J. P. Marton, J. Electrochem. Soc, 123 (1976) 203C

[139] H. Wang, Y. Yan, K. Li, X. Du, Z. Lan and H. Jin, Phys. Status Solidi B 247 , No. 2 (2010) 444

[140] L. B. Shi, H. K. Dong, G. Q. Qi, J. Magn. Magn. Mater, 345 (2013) 215-221.

[141] W. Z. Xiao, L. L. Wang, L. Xu, Q. Wan, B.S. Zou, Solid State Commun, 149 (2009) 1304-1307.

[142] S. Mohanty, S. Ravi, Solid State Commun, 150 (2010) 739-742

[143] K. Anandan, V. Rajendran, Superlattices Microstruct, 85 (2015) 185

[144] Y. Xiao, , S. Ge, , L. Xi, Y. Zuo, X. Zhou, B. Zhanga, Li Zhang, C. Li, X. Han, Z. Wen, Appl. Surf. Sci, 254 (2008) 7459

[145] A. Espinosa, N. Sánchez, J. S. Marcos, A. D. Andrés, M. C. Muñoz, J. Phys. Chem. C, 115 (2011) 24054–24060

[146] X. G. Chen, W. W. Li, J. D. Wu, J. Sun, K. Jiang, Z. G. Hu, J. H. Chu, Mater. Res. Bull, 47 (2012) 111–116

[147] Y. Ziat, A. Benyoussef, A. El Kenz, J. Phys. Chem. Solids, 75(2014) 701-709

[148] MACHIKANEYAMA2002v09 :H. Akai , Department of Physics, Graduate School of Science ,Osaka University, Machikaneyama 1-1, Toyonaka 560-0043, Japan, akai@phys.sci.osaka-u.ac.jp

[149] V. Golovanov, V. Golovanova, T. T. Rantala, J. Phys. Chem. Solids, 89(2016) 16

[150] J. Bai, J. M. Raulot, Y. D. Zhang, C. Esling, X. Zhao, L. Zuo, J. Appl. Phys, 109 (2011) 014908

[151] Y. Yan, S. B. Zhang, Phys. Rev. Lett., 86 (2001) 5723-5726

[152] Z. Zarhri, A. Benyoussef, A. El Kenz, J. Supercond. Novel. Magn 27 (2013) 1326

[153] H. Ohno, Science, 281 (1998) 951

[154] R. H. French, S. J. Glass, F. S. Ohuchi, Y. N. Xu, and W. Y. Ching, Phys. Rev. B, 49 (1994) 5133

[155] T. Archer, C. Das Pemmaraju, S. Sanvito, J. Magn. Magn. Mater. 316 (2007) e188

[156] P. W. Peacock, J. Robertson, Phys. Rev. Lett. 92 (2004) 057601

[157] P. Shuk, E. Bailey, U. Guth, Mod. Sens. Technol. 90 (2008) 174

[158] A. Abbassi, H. Ez-Zahraouy, A. Benyoussef, Opt Quant Electron, 47 (2015) 1869

[159] M. Boujnah, O. Dakir, H. Zaari, A. Benyoussef, and A. El Kenz, J. Appl. Phys. 116 (2014) 123703

[160] A. Labdelli, N. Hamdad, Results in Physics, 5 (2015) 48

[161] J. C. Garcia, L. M. R. Scolfaro, A. T. Lino, V. N. Freire, G. A. Farias, C. C. Silva, H. W. L. Alves, S. C. P. Rodrigues, and E. F. da Silva, J. Appl. Phys. 100 (2006) 104103

[162] R. T. Shuey, Semiconducting Ore Minerals, Elsevier, Amsterdam, 1975

[163] N. Weiss, SME Mineral Processing Handbook, Society of Mining Engineers, 1985

[164] J. B. Murowchick, H.L. Barnes, American Mineralogist 72 (1987) 1241

[165] G. L. Zhao, J. Callaway, M. Hayashibara, Phys. Rev. B, 48 (1993) 15781-1576

[166] Y. N. Zhang, J. Hu, M. Law, R. Q. Wu, Phys. Rev. B, 85 (2012) 085314

[167] A. Hung, J. Muscat, I. Yarovsky, S. P.Russo, J. of Suf. Sci, 513 (2002) 511

[168] B. Kolb, A. M. Kolpak, Phys. Rev. B, 88 (2013) 235208

[169] Vaughan, D. J, Chemical bonding and spectroscopy in mineral chemistry (1985) 251-292

[170] P. Baláž, A. Aláčová, E. Godočíková, J. Kováč, I. Škorvánek, J.Z. Jiang, Czech. J. Phys, 54 (2004) D197-D200

[171] M. Cabán-Acevedo, M. S. Faber, Y. Tan, R. J. Hamers and S. Jin, Nano lett 12 (2012) 1977

[172] B. Thomas, T. Cibik, C. Höpfner, K. Diesner, G. Ehlers, S. Fiechter, K. Ellmer, j. mater. sci. mater. electron, 9 (1998) 61

[173] W. Qui, J. Xia, H. Zhong, S. He, S. Lai, L. Chen, Electrochimica Acta, 137 (2014) 197-205

[174] S. H. Vosko, L. Wilk, M. Nusair, Can. J. Phys. 58 (1980) 1200

[175] S. Finklea, L. Cathey, E. Amma, Acta Crystallographica 32 (1976) 529

[176] T. A. Bither, R. J. Bouchard, W. H. Cloud, P. C. Donohue, W. J. Siemons, Inorg Chem, 7 (1968) 2208-2220

[177] V. Eyert, K. H. Höck, S. Fiechter and H. Tributsch, Physical Review B, 57 (1998) 6350-6358

[178] S. K. Kwon, S. J. Youn, and B. I. Min, Physical Review B, 62(2000) 357

[179] S. Miyahara and T. Teranishi, J. Appl. Phys, 39 (1968) 896

[180] S. Ogawa, J. Appl. Phys, 50 (1979) 2308

[181] D. Wan, Y. Wang, Z. Zhou, G.Yang, B. Wang, L. Wei, Mater. Sci. Eng., B, 122 (2005) 156–159

[182] Y. H. Liu, L. Meng, L. Zhang, Thin Solid Films 479 (2005) 83–88

[183] V. K. Gudelli, V. Kanchana, , S. Appalakondaiah, , G. Vaitheeswaran, and M. C.V. alsakumar, J. Phys. Chem. C, 117(2013) 21120-21131

[184] A. Schlegel, P. Wachter, J. Phys. C: Solid State Phys , 17 (1976) 3363

[185] T. R. Rana, D. B. Khadka, J. H. Kim, Mater. Sci. Semicond. Process, 40 (2015) 325–330

[186] P. Möller, G. Kersten, Mineralium Deposita, 29 (1994) 404-413

[187] R. Sun, M. K. Y. Chan, S. Y. Kang, G. Ceder, Phys. Rev. B, 84 (2011) 035212

[188] R. J. Soukup, P. Prabukanthan, N. J. Ianno, A. Sarkar, C. A. Kamler, D. G. Sekora, J. Vac. Sci. Technol. A, 29 (2011) 011001

[189] I. Opahle, K. Koepernik, H. Eschrig, Phy. Rev. B, 60 (1999) 14035

[190] W. M. Temmerman, P. J. Durham, and D. J. Vaughan, Phys. Chem. Miner, 20(1993) 248

[191] W. Folkerts et al., J. Phys. C: Solid State Phys, 20 (1987) 4135

[192] M. Imada, A. Fujimori and Y. Tokura, Rev. Mod. Phys, 70(1998) 1039

[193] Y. Ziat, Z. Zarhri, A. Slassi, A. Benyoussef, A. El Kenz, J. Supercond. Nov. Magn, 28 (2015) 3645-3649

[194] E. Şaşioglu, L. M. Sandratskii, P. Bruno, Journal of Physics: Condensed Matter, 17 (2005) 995-1001

[195] D. J. Priour Jr, E. H. Hwang, S. D. Sarma, Phys. Rev. lett, 92(2004) 117201

[196] Y. H. Chang, C. H. Park, K. Sato, H. Katayama-Yoshida, Phy. Rev. B, 75 (2007) 125211

[197] H. Zaari, M. Boujnah, H. Labrim, B. Khalil, A. Benyoussef and A. El Kenz, J. Supercond. Nov. Magn, 26 (2013) 2961-2967

*Abstract*

*Within LDA, the ferrimagnetic state is predicted in $Sn_{0.98-x}Mn_{0.02}Cr_xO_2$ (x=0.09). Within GGA, the stability of the ferrimagnetic also is observed (x=0.05). $Sn_{0.98}Mn_{0.02}O_{1.95}F_{0.05}$ system could induce the FM stability instead the DLM and shows the half-metallic characteristic. Within GGA, $Zr_{14}OsCoO_{32}$ system provides the half-metallic behavior. With mBJ, the presence of magnetic gap is predicted. For $Zr_{14}MnCoO_{32}$; the system provides the half metallic behavior. For $FeS_2$ pyrite, the antiferromagnetic (AFM) stability belongs to super-exchange coupling is observed in $Fe_{0.98}V_{0.02}S_2$. However, $Fe_{0.95}Cr_{0.05}S_2$ shows FM stability belongs to double-exchange coupling type and having a considered $T_C$ which leads to significant magnetic proprieties. Moreover, 3d-3d hybridization of transition metals show that is believed to result half-metal propriety. The stabilization of the FM state in N-doped $Fe_{0.98}V_{0.02}S_2$ is observed.*

*Key words: ab intio; Diluted magnetic semiconductors; spintronic; ferromagnetic; ferrimagnetic; half metallic.*



✉ Faculté des Sciences, avenue Ibn Battouta, BP. 1014 RP, Rabat –Maroc
☎ 00212(0) 37 77 18 76 🖷 00212(0) 37 77 42 61 ; http://www.fsr.ac.ma